

Summer 8-2015

Random Actuation Pattern Optimization by Genetic Algorithm for Ultrasonic Structural Health Monitoring of Plates

Pierrot R. Derjany
Embry-Riddle Aeronautical University

Follow this and additional works at: <https://commons.erau.edu/edt>



Part of the [Mechanical Engineering Commons](#)

Scholarly Commons Citation

Derjany, Pierrot R., "Random Actuation Pattern Optimization by Genetic Algorithm for Ultrasonic Structural Health Monitoring of Plates" (2015). *Doctoral Dissertations and Master's Theses*. 297.
<https://commons.erau.edu/edt/297>

This Thesis - Open Access is brought to you for free and open access by Scholarly Commons. It has been accepted for inclusion in Doctoral Dissertations and Master's Theses by an authorized administrator of Scholarly Commons. For more information, please contact commons@erau.edu.

RANDOM ACTUATION PATTERN OPTIMIZATION BY GENETIC ALGORITHM
FOR ULTRASONIC STRUCTURAL HEALTH MONITORING OF PLATES

A Thesis

Submitted to the Faculty

of

Embry-Riddle Aeronautical University

by

Pierrot R. Derjany

In Partial Fulfillment of the

Requirements for the Degree

of

Master of Science in Aerospace Engineering

August 2015

Embry-Riddle Aeronautical University

Daytona Beach, Florida

RANDOM ACTUATION PATTERN OPTIMIZATION BY GENETIC ALGORITHM
FOR ULTRASONIC STRUCTURAL HEALTH MONITORING OF PLATES

by

Pierrot R. Derjany

A Thesis prepared under the direction of the candidate's committee chairman, Dr. Dae Won Kim, Department of Aerospace Engineering, and has been approved by the members of the thesis committee. It was submitted to the School of Graduate Studies and Research and was accepted in partial fulfillment of the requirements for the degree of Master of Science in Aerospace Engineering.

THESIS COMMITTEE



Chairman, Dr. Dae Won Kim



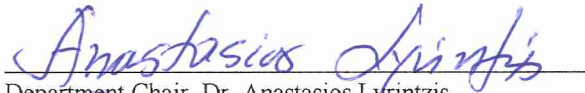
Member, Dr. Susan Allen



Member, Dr. Sirish Namilae



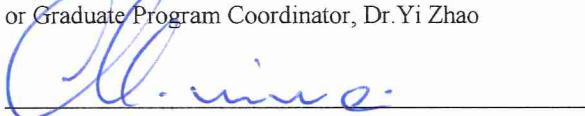
Member, Dr. Andrei Ludu



Department Chair, Dr. Anastasios Lyrintzis
or Graduate Program Coordinator, Dr. Yi Zhao

8/25/15

Date



Dean of College of Engineering, Dr. Maj Mirmirani

8/26/15

Date



Vice Chancellor for Academic Support, Dr. Christopher Grant

8/26/15

Date

ACKNOWLEDGMENTS

I would like to express my deepest gratitude to my thesis advisor, Dr. Dae Won Kim, who introduced this topic to me. His mentorship and supervision in the pursuit of this research were infinitely valuable.

I would also like to thank my thesis committee members, Dr. Susan Allen, Dr. Sirish Namilae and Dr. Andrei Ludu, who have patiently and carefully assisted me throughout the thesis process. They have continually inspired me with courage, spirit and confidence.

In addition, a thank you to my friends, Peter Osterc and Boutros Azizi, who stimulated me with support and approval, and whose enthusiasm for aerospace engineering had a positive effect. Without their continual help, this work would not have been established in this way.

I would like to further express my appreciation to Prof. Charles Lee and Miss Sheila Bishop for believing in my ambitions and providing me with an opportunity of employment. I am also indebted to the Philippe Jaber Foundation and Mr. Adib Derjany for their generous contributions to my quest for knowledge.

Finally, I owe the greatest sense of gratefulness to my parents, Raymond and Kaly. Believing that education is the best head-start on life as it paves the way for a promising future, they continuously supported me without hesitation, both morally and financially, through my many years of education. Thank you again for always backing me up to chase my dreams.

TABLE OF CONTENTS

LIST OF TABLES	vi
LIST OF FIGURES	vii
ABSTRACT	xi
1. Introduction	1
1.1. Damage Definition and Classification	2
1.2. Non Destructive Examination (NDE)	3
1.3. Structural Health Monitoring (SHM)	4
2. Elastic Waves	9
2.1. Guided Lamb Waves	9
2.2. Wave Equations	10
2.2.1. Isotropic Wave Equations	11
2.2.2. Anisotropic Wave Equations	17
2.3. Phase and Group Velocity and Slowness Curve	19
2.4. Skew Angle	21
2.5. Dispersion Curves for a Traction Free Plate	21
2.5.1. Isotropic Medium	22
2.5.2. Anisotropic Medium	24
3. Beamforming Presentation	26
3.1. Formulation of Wave Beamforming from Multiple Excitation Sources in an Anisotropic Medium	28
3.1.1. Simultaneous Excitations (No Delay)	29
3.1.2. Successive Excitations (Time Delay Interval)	37
3.2. Wave Beamforming from Multiple Excitation Sources in an Isotropic Medium	40
4. Pattern Geometry	42
4.1. Actuation Time Delay	43
4.2. Isotropic Propagation Medium	44
4.3. Anisotropic Propagation Medium	46
5. Finite Element Model and Results	51
5.1. Plate Modelling	52
5.1.1. Part Creation	52
5.1.2. Material Selection and Section Assignment	53
5.1.3. Step Formation	54
5.1.4. Loads and Boundary Conditions Attribution	54
5.1.5. Mesh Instance Creation	55
5.1.6. Field and Output Request Generation	57
5.1.7. Job Creation and Verification	57
5.2. Postprocessing, Results and Plots	58
5.3. Results Confirmation	60

6.	Optimization Algorithm	62
6.1.	Proposed Algorithms for Phased Arrays.....	62
6.1.1.	Linear Arrays	62
6.1.2.	Circular Arrays	64
6.1.3.	Multi-Dimensional Arrays.....	65
6.2.	Algorithm Selection	66
6.2.1.	Genetic Algorithm.....	66
6.2.2.	Particle Swarm Optimization.....	67
6.2.3.	Interpretation and Selection	68
6.3.	The Process of Optimization for The GA.....	72
7.	Data Analysis and Findings.....	83
7.1.	Random Array Results for Aluminum.....	83
7.2.	Random Array Results for a 0° Unidirectional Laminate.....	86
7.3.	Random Array Results for a 90° Unidirectional Laminate	90
7.4.	Results of Uniformly Distributed Linear Array for an Orthotropic Laminate	92
7.5.	Results of Uniform Array Geometries for an Isotropic Material	92
7.6.	Discussion and Interpretation	93
8.	Conclusion and Future Work	96
	REFERENCES	97

LIST OF TABLES

Table 1.1 A series of NDE techniques for metal alloys (Colangelo & Heiser, 1987)	4
Table 1.2 Non-Destructive Evaluations applicable for composites failure modes (Vaara & Leinonen, 2012)	4
Table 5.1 Mechanical properties of the aluminium and composite	53
Table 7.1 Beamwidth first null and sidelobes' levels at different random actuation points for an isotropic medium	93
Table 7.2 Beamwidth first null and sidelobes' levels at different uniformly spaced actuation points for an isotropic medium.....	93
Table 7.3 Beamwidth first null and sidelobes' levels at different random actuation points for a 0° unidirectional fiber plate	94
Table 7.4 Beamwidth first null and sidelobe levels at different random actuation points for a 90° unidirectional fiber plate	94
Table 7.5 Beamwidth first null and sidelobes' levels at different random actuation points for a linear 20 actuators array over a composite plate	94

LIST OF FIGURES

Figure 1.1 ISS Ultrasonic Background Noise Test System Overview (Richards, Madaras, Prosser & Studor, 2013)	6
Figure 1.2 A typical schema of the internal components of an accelerometer (en.wikipedia.org)	7
Figure 1.3 Components of a Fiber-optic-based SHM system (micronoptics.com)	7
Figure 2.1 Lamb wave propagation modes; (a) antisymmetric; (b) symmetric.....	10
Figure 2.2. Lamb wave propagation for structural health monitoring of composite laminate using: (a) pitch-catch; (b) pulse-echo methods (Calomfirescu, 2008).....	11
Figure 2.3 Circular wave fronts produced by a single point source in a two-dimensional plane.....	15
Figure 2.4 Two dimensional plate with single point sources and two sensing nodes A and B in space domain.....	20
Figure 2.5 Out-of-plane displacement of a disturbance signal in time domain.....	20
Figure 2.6 Free boundaries 2mm aluminum plate dispersion relations; (a) phase velocity; (b) group velocity curves (Wan <i>et al.</i> , 2014).....	22
Figure 3.1 Wave interference from two point sources: (a) top view; (b) constructive and destructive out of plane displacement profile.	26
Figure 3.2 Focused directional radiation pattern Left-In polar coordinates; Right-In cartesian coordinates (MATLAB R2011a).....	27
Figure 3.3 Wave front in the near and far fields respectively	28
Figure 3.4 Near field schema for single actuation point.....	29
Figure 3.5 Far field schema for single actuation point	35
Figure 3.6 Schematic of near field for a single actuation point and a target at 90° direction.	39
Figure 4.1 different pattern configuration: (a) linear; (b) rectangular; (c) disk; (d) circular arrays (Lingyu, 2006).....	43
Figure 4.2 Excitations delays in time domain.....	43
Figure 4.3 Aluminum pattern geometry for a target point in the 90° direction	44
Figure 4.4 The x_m and y_m coordinates range for an isotropic medium.....	46
Figure 4.5 Pattern arrangement on elliptical arcs for fiber reinforced composites: (a) for a single actuation; (b) for M actuations	48
Figure 5.1 A top view of the quarter plate (ABAQUS/CAE 6.14).....	52
Figure 5.2 50 KHz 2.5 Hanning window for 0.1 ms excitation interval.....	55

Figure 5.3 Normal load and boundary conditions imposed to the thin plate (ABAQUS/CAE 6.14)	55
Figure 5.4 Sensors distribution on the 150 mm radius quarter plate (ABAQUS/CAE 6.14)	57
Figure 5.5 Signal response detected by a sensor 50mm from the excitation source (ABAQUS/CAE 6.14)	58
Figure 5.6 Out-of-plane displacement amplitude; (a) for aluminium; (b) for composite for 0° fiber angle (ABAQUS/CAE 6.14)	59
Figure 5.7 Characteristics of a 50 KHz lamb wave propagation in an aluminum plate of thickness 1.125mm: (a) amplitude profile; (b) phase velocity; (c) slowness curve.....	59
Figure 5.8 Characteristics of a 50 KHz lamb wave propagation in a unidirectional 0° composite plate of thickness 1.125mm: (a) amplitude profile; (b) phase velocity; (c) slowness curve	60
Figure 5.9. Wave characteristics of 12-layer unidirectional laminate: (a) phase velocity; (b) peak-to-peak amplitude profiles (Salas and Cesnik, 2010).....	61
Figure 5.10. Slowness curves at different frequency-thickness product of antisymmetric Lamb wave dispersing in unidirectional laminate (Pant, 2014)	61
Figure 6.1 Chromosome single point cross-over	69
Figure 6.2 Chromosome mutations.....	69
Figure 6.3 The <i>i</i> th particle's local and global best displacement and velocity vectors (Hassan et Al., 2004)	71
Figure 6.4 The flow chart of the proposed Genetic Algorithm for multi-directional sparse array	73
Figure 6.5 A three dimensional array of the wave radiators. Left - In plane arrangement; Right - An isometric view (Bhattacharya M. et Al., 2012).....	79
Figure 7.1 Polar beamforming resulting from 40 actuators and pointing towards a 90° target on an aluminum plate.....	84
Figure 7.2 A Cartesian plot of the array factor illustrating the main beam at 90° and its adjacent side lobes of 40 actuators for an isotropic medium	84
Figure 7.3 The convergence process of the cost function to the optimum solution by means of a Genetic Algorithm processing of 40 locations for an isotropic medium.....	84
Figure 7.4 A space arrangement of the 40 actuation points enclosed within a circular aperture and facing a target point in the near field on an aluminum plate.....	84
Figure 7.5 Polar beamforming resulting from 51 random actuators and pointing towards a 90° target on an aluminum plate	85
Figure 7.6 A Cartesian plot of the array factor illustrating the main beam at 90° and its adjacent side lobes of 51 actuators for an isotropic medium	85
Figure 7.7 The convergence process of the cost function to the optimum solution by	

means of a Genetic Algorithm processing of 51 locations for an isotropic medium.....	85
Figure 7.8 A space arrangement of the 51 actuation points enclosed within a circular aperture and facing a target point in the near field on an aluminum plate.....	85
Figure 7.9 Polar beamforming resulting from 66 random actuations and pointing towards a 90° target on an aluminum plate	86
Figure 7.10 A Cartesian plot of the array factor illustrating the main beam at 90° and its adjacent side lobes of 66 actuations for an isotropic medium	86
Figure 7.11 The convergence process of the cost function to the optimum solution by means of a Genetic Algorithm processing of 66 locations for an isotropic medium.....	86
Figure 7.12 A space arrangement of the 66 actuation points enclosed within a circular aperture and facing a target point in the near field on an aluminum plate.....	86
Figure 7.13 Polar beamforming resulting from 20 random actuations and pointing towards a 90° target on a 0° unidirectional fiber plate.....	87
Figure 7.14 A Cartesian plot of the array factor illustrating the main beam at 90° and its adjacent side lobes of 20 actuations in a 0° fiber medium.....	87
Figure 7.15 The convergence process of the cost function to the optimum solution by means of a Genetic Algorithm processing of 20 locations in a 0° fiber medium	87
Figure 7.16 A space arrangement of the 20 actuation points enclosed within a circular aperture and facing a target point in the near field on a 0° Unidirectional Laminate.....	87
Figure 7.17 Polar beamforming resulting from 51 random actuations and pointing towards a 90° target on a 0° unidirectional fiber plate.....	88
Figure 7.18 A Cartesian plot of the array factor illustrating the main beam at 90° and its adjacent side lobes of 51 actuations in a 0° fiber medium.....	88
Figure 7.19 The convergence process of the cost function to the optimum solution by means of a Genetic Algorithm processing of 51 chromosomes in a 0° fiber medium	88
Figure 7.20 A space arrangement of the 51 actuation points enclosed within a circular aperture and facing a target point in the near field on a 0° Unidirectional Laminate.....	88
Figure 7.21 Polar beamforming resulting from 66 random actuations and pointing towards a 90° target on a 0° unidirectional fiber plate.....	89
Figure 7.22 A Cartesian plot of the array factor illustrating the main beam at 90° and its adjacent side lobes of 66 actuations in a 0° fiber medium.....	89
Figure 7.23 The convergence process of the cost function to the optimum solution by means of a Genetic Algorithm processing of 66 locations in a 0° fiber medium	89
Figure 7.24 A space arrangement of the 66 actuation points enclosed within a circular aperture and facing a target point in the near field on a 0° Unidirectional Laminate.....	89
Figure 7.25 Polar beamforming resulting from 18 random actuations and pointing towards a 90° target on a 90° unidirectional fiber plate.....	90

Figure 7.26 A Cartesian plot of the array factor illustrating the main beam at 90° and its adjacent side lobes of 18 actuations in a 90° fiber medium.....	90
Figure 7.27 The convergence process of the cost function to the optimum solution by means of a Genetic Algorithm processing of 18 locations in a 90° fiber medium	90
Figure 7.28 A space arrangement of the 18 actuation points enclosed within a circular aperture and facing a target point in the near field on a 90° Unidirectional Laminate.....	90
Figure 7.29 Polar beamforming resulting from 20 random actuations and pointing towards a 90° target on a 90° unidirectional fiber plate.....	91
Figure 7.30 A Cartesian plot of the array factor illustrating the main beam at 90° and its adjacent side lobes of 20 actuations in a 90° fiber medium.....	91
Figure 7.31 The convergence process of the cost function to the optimum solution by means of a Genetic Algorithm processing of 20 locations in a 90° fiber medium	91
Figure 7.32 A space arrangement of the 20 actuation points enclosed within a circular aperture and facing a target point in the near field on a 90° Unidirectional Laminate.....	91
Figure 7.33 Polar beamforming resulting from 20 linear actuations and pointing towards a 90° target on a 0° unidirectional fiber plate	92
Figure 7.34 Polar beamforming resulting from 20 linear actuations and pointing towards a 90° target on a 90° unidirectional fiber plate	92
Figure 7.35 Polar beamforming resulting from 40 linear actuations and pointing towards a 90° target on an aluminum plate	93
Figure 7.36 Polar beamforming resulting from a disk pattern of 40 actuations and pointing towards a 90° target on an aluminum plate	93
Figure 7.37 Polar beamforming resulting from a disk pattern of 66 actuations and pointing towards a 90° target on an aluminum plate	93

ABSTRACT

Derjany, Pierrot MSAE, Embry-Riddle Aeronautical University, August 2015. Actuation Pattern Optimization by Genetic Algorithm for Structural Health Monitoring.

The objective of this research is to investigate an optimized two-dimensional random pattern of uniformly excited points using the Genetic Algorithm (GA) technique for structural health monitoring. The point excitations generate ultrasonic waves in both isotropic and anisotropic materials that can be effective in diagnosing structural defects. The formed ultrasonic waves can constructively interfere and send out an intense wave beam to a predetermined target. The constructed wave beams can be steered to different directions with variable target distances. In the GA, the cost function is constructed to reduce main lobe beamwidth, eliminate grating lobes and suppress sidelobes' levels. Mathematical modelling, finite element simulations, and optimizations are successively performed to achieve the objectives.

Firstly, a mathematical beamforming model is developed to describe the excitation pattern of which each point is excited at the same time delay with a uniform weighting factor. The derived methodology accounts for enclosing all excitations within a certain aperture. The centroid of the emitting sources is also kept at the origin of the Cartesian coordinate within a slight tolerance range. For the near field, in isotropic materials, the excitation points lay on equally spaced circular arcs centered at the target point. In anisotropic materials, such as composites, the wave amplitude and phase velocity are highly dependent on fiber directions. Because of anisotropic nature, the excitation geometry becomes quite complicated.

Secondly, finite element models for aluminum and composite plates are simulated to extract wave characteristics, such as displacement amplitudes, phase velocity profiles and slowness curves. These data are implemented later in the optimization algorithm. A quarter plate of radius 150mm and 1.125mm thickness is modelled as a three-dimensional solid part. A concentrated force with a 2.5 cycle-Hanning window sinusoidal signal is applied at the center of the plate and the boundaries are chosen to be symmetrical. Radial sensors at 5 degrees increments are positioned at 50mm from the excitation source to measure wave properties. The simulation results show that the amplitude and velocity are uniform for isotropic materials whereas the waves propagate rapidly with higher amplitudes along the fibers in anisotropic materials.

Thirdly, after collecting all the required information, a GA optimization technique is applied to generate the excitation population of x- and y-coordinates. The pre-determined population is permuted, cross-overed and mutated so that additional possibilities are produced. The same process is repeated for many generations until the local optimum result is obtained.

Finally, the near field beamforming is plotted in MATLAB at different actuation point numbers for the isotropic and anisotropic materials. The results are then compared to other linear, circular and planar patterns found in literature.

1. Introduction

Structural and mechanical components are always exposed to functioning damages, thus, continuous inspection and restoration are mandatory. To return the equipment to a previous state or keep it operating at its existent condition, significant funds are spent for repair and maintenance. For instance, airline operators normally maintain their fleet based on prescheduled maintenance. This method is set by the manufacturers who analyze historical trends after severe failures of mechanical devices. This preventive process increases operating costs as it sometimes requires replacement of non-defected parts and additional labor. Industries are trying to minimize these costs through a structural health monitoring (SHM) method depending on the actual status and lifetime of the component.

Nowadays, engineers consider SHM a powerful tool to improve the maintainability and safety of critical structures. In aerospace industries, SHM was developed when different airlines and manufacturers collaborated to establish the condition based maintenance (CBM) program. Traditional time-based maintenance activities assume that all flight sorties stress the aircraft in the same way. However, some maneuvers and harsh operational environments strain certain parts more than others and have a direct influence on their life cycle. The SHM system implements transducers which allow continuous observation of a system and data collection of critical components to obtain real time updates during flight. Thus, defected parts may be repaired or replaced upon indications of malfunction.

The SHM technique continuously observes a system and periodically extracts vibration data by spaced time intervals. Therefore, the operators are kept updated about

the status of the equipment and noticed about a present damage and its location on the assembly. State-of-the-art SHM methods still do not deliver sufficient information about the extent and the nature of the occurred damage. It is said that such “global” SHM evaluates the overall health of the structure. Therefore, supplementary non-destructive-examinations (NDE) need to be accomplished on the defected part to assess local monitoring (Deng & Liu, 2011).

1.1.Damage Definition and Classification

Damage is generally defined as an alteration of an operating system in a way that its present or future performance is impacted (Farrar & Worden, 2007 qtd. in Deng & Liu, 2011). In this thesis, the damage is investigated on static structures. Accordingly, the changes in material and geometric properties leading to modification of boundary conditions and system connectivity (Deng & Liu, 2011) are of major concern.

Damage is assessed on length and time scales (Deng & Liu, 2011). In terms of length-scales, any component has typically inherent microscopic manufacturing defects known also as flaws. On the other hand, not every damage causes entire functionality failure. Failure is the point where the damage overpasses the allowable threshold and severely affects the system’s operation. On the time level, a flaw expands progressively and the rate of propagation can be either slow or fast. Fatigue or corrosion accumulate over a long period of time, whereas scheduled discrete events happen instantaneously. For instance, at landing, an aircraft touch-down is a prompt state causing a high dynamic loading that severely stresses the undercarriage (Deng & Liu, 2011).

Referring to Rytter (1993), the damage status is analyzed by responding to the following questions (qtd. in Deng & Liu, 2011):

- Is the system really damaged or not? (Existence)
- If present, where is the damage position on the structure? (Location)
- What kind of damage is it? (Type)
- How severe is the defect? (Extent)
- What is the remaining life of the part? (Prognosis)

The answers of these inquiries are fulfilled by the Structural Health Monitoring technique and Non-Destructive-Evaluations.

1.2.Non Destructive Examination (NDE)

Non-Destructive Evaluation is the discipline of evaluating the integrity of materials and structures without triggering any harm. The terms Non-Destructive Evaluation (NDE), Non-Destructive Examination (NDE), Non-Destructive Inspection (NDI) and Non-Destructive Testing (NDT) are interchangeable. NDE is critical to determine the system safety and reliability. In conventional NDE's, the part to be examined is "carried out off-line" to be inspected. However, current innovative techniques enable inspection of "in-situ" structures (Deng & Liu, 2011).

NDTs are numerous and depend on the material being checked. The selection of the appropriate method depends on the type of defect to be explored. Aluminum alloys and reinforced composites are often used in most aircraft structures. Aluminum experiences various failure modes such as fatigue, corrosion fatigue, creep and fracture. Some of the techniques to detect such failures are shown in Table 1.1. Anisotropic composites undergo other failure scenarios, shown in Table 1.2 with their appropriate examination performances.

Table 1.1. A series of NDE techniques for metal alloys (Colangelo & Heiser, 1987)

Technique	Defect Location	Defect Size Sensitivity (mm)	Testing Location
Scanning electron microscopy (SEM)	Surface	>0.001	Laboratory
Dye penetrant	Surface	0.025–0.25	Laboratory/in-field
Ultrasonics	Subsurface	>0.050	Laboratory/in-field
Optical microscopy	Surface	0.1–0.5	Laboratory
Visual inspection	Surface	>0.1	Laboratory/in-field
Acoustic emission	Surface/subsurface	>0.1	Laboratory/in-field
Radiography (X-ray/ gamma ray)	Subsurface	>2% of specimen thickness	Laboratory/in-field

Table 1.2. Non-Destructive Evaluations applicable for composites failure modes (Vaara & Leinonen, 2012)

	Acoustic Emission (AE)	Acoustic Impact (AI)	Laser Shearography (LS)	Mechanical Impedance (MI)	Membrane Resonance (MR)	Transient Thermography (TT)	Ultrasonic Amplitude C-Scan (UC)	Ultrasonic Thickness A-Scan (UA)	Ultrasonic Linear B-Scan (UB)	Ultrasonic Depth Scan (UD)	X-Radiography (XR)
10 High High applicability											
7-9 Good Good applicability											
4-6 Medium Some applicability											
1-3 Low Limited applicability											
0 None No applicability											
Delamination (<10 mm)	7	2	9	4	4	8	9	5	8	9	7
Delamination (>10 mm)	7	5	10	6	6	10	10	8	10	10	7
Crack	7	0	9	0	0	4	0	0	0	0	8
Disbond	2	5	10	6	6	10	10	8	10	10	7
Void	0	1	5	1	1	5	10	6	6	6	10
Impact (BVI)	7	5	10	6	6	8	10	10	10	10	4
Porosity	0	0	8	0	0	6	9	5	6	4	10
Inclusion	0	3	7	4	4	7	9	7	7	6	6
Erosion	0	0	5	0	0	7	7	9	10	10	4
Core splice	0	5	8	5	5	4	6	1	2	0	8
Core disbond	1	10	10	10	10	10	10	8	9	8	5
Core crushing	5	10	5	10	10	5	8	5	5	0	5
Matrix Cracking	10	0	0	0	0	0	0	0	0	0	6
Fibre breakage	10	4	6	4	4	0	0	0	0	0	5
Kissing Bond	0	1	5	1	1	2	1	0	0	0	0
Environment ingress	0	0	4	0	0	10	8	4	5	0	5
Fibre Wrinkling/Waviness	0	0	4	0	0	2	9	1	8	0	2
Fibre and ply misalignment	0	0	2	0	0	2	9	0	1	0	5
Incorrect cure	0	0	0	0	0	0	2	0	5	5	0
Excess resin	0	0	5	0	0	6	5	0	5	8	2
Excess fibre	0	0	5	0	0	6	5	0	5	8	2

1.3. Structural Health Monitoring (SHM)

Chang *et al.* (2003) explain structural health monitoring as “the process of determining and tracking structural integrity and assessing the nature of damage in a structure (or the process of implementing a damage identification strategy)” (qtd. in Deng

& Liu, 2011).

The statistical pattern recognition paradigm for SHM involves (Farrar & Worden, 2013):

- Operational evaluation: Defines the specific type of damage to be identified and the technical, operational and environmental restrictions facing the SHM system.
- Data acquisition: Selects the suitable hardware and the data to be extracted and interpreted.
- Feature extraction: Identifies the damage features and set the standards and thresholds for data classification.
- Statistical model development for feature discrimination: Distinguishes between damaged and undamaged states.

Conventional method for structural assessment relies upon the displacement and velocity response to applied loads. These characteristics are obtained by solving the differential system of motion equations depending on the mass, damping and stiffness matrices when loads are applied on the system (Nagayama & Spencer, 2007). The current engineering proposes complicated, huge structures consisting of different members making such method time costly and theoretically difficult to manipulate. An innovative approach is suggested by monitoring the vibration measurements delivered by “smart sensors” attached to the excited structural constituents. The essential aspects of a smart sensor are (Nagayama & Spencer, 2007):

- On-board microprocessor for data analysis
- High sensing ability
- Wireless communication between the sensing devices and the microprocessor

- Battery-powered for long term use
- Affordable operational cost

For their unmanned aerial vehicles, composite crew module, reentry vehicles, space vehicles, vehicle pressure systems, space shuttle orbiter and expendable launch vehicles, NASA manipulated three types of transducers to fulfill the mission purposes (Richards, Madaras, Prosser & Studor, 2013):

- Piezoelectric sensor-based SHM on the International Space Station (ISS). Piezoelectricity is defined as the ability of a certain type of material to accumulate electric charges when subjected to a mechanical load. The amount of stress is determined by measuring the voltage at the dipoles of the transducer. The Distributed Impact Detection System (DIDS) identifies leak sites on space vehicles by means of piezoelectric sensors (Richards, Madaras, Prosser & Studor, 2013) bonded to the structure as shown in Figure 1.2.

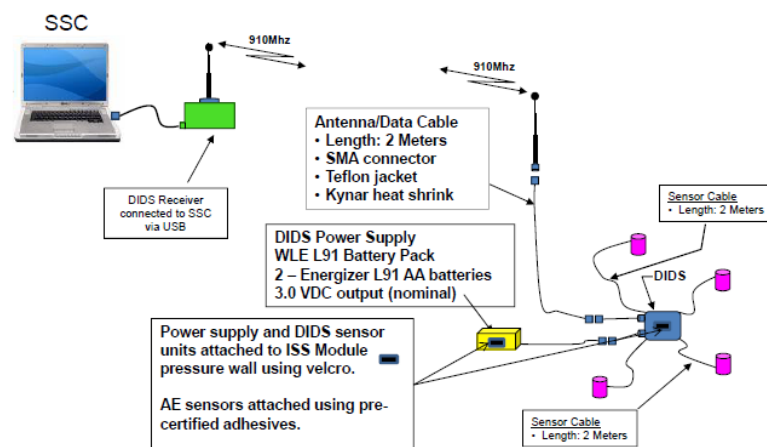


Figure 1.1. ISS Ultrasonic Background Noise Test System Overview (Richards, Madaras, Prosser & Studor, 2013)

- Piezoelectric accelerometers and acoustic-based SHM on space shuttles. The accelerometers constitute the Wing Leading Edge Impact Detection System (WLEIDS). They are mounted on all Shuttles to detect impacts during ascent. A cross-sectional view of an accelerometer is shown in Figure 1.3.

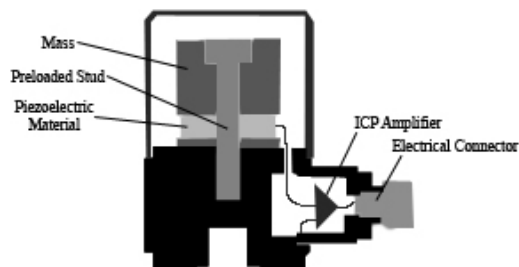


Figure 1.2. A typical schema of the internal components of an accelerometer (en.wikipedia.org)

- Fiber-optic-based SHM on Aerospace Vehicles. Such system possesses a light source, optical fibers, a transducer and a detector as shown in Figure 1.4 (Krohn, MacDougall & Mendez, 2015).

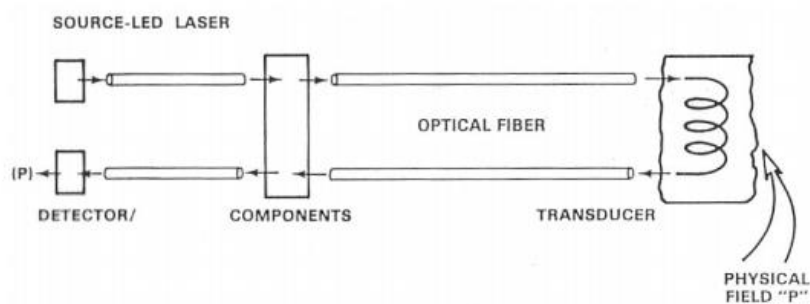


Figure 1.3. Components of a Fiber-optic-based SHM system (micronoptics.com)

Fiber Optic Sensing with Fiber Bragg Gratings (FBG) has promising applications for space vehicles. Fiber Bragg Grating Optical Frequency Domain Reflectometry enables real time measurement of strain, temperature, liquid level, mode shapes, natural frequencies, buckling modes, etc. (Richards, Madaras, Prosser & Studor, 2013).

A FBG sensor reflects a portion of the emitted light, propagating at “Bragg” wavelength, and allows passage of the remaining beam without affecting its property. The Bragg wavelength is determined from the fiber refractive index (Baskar Rao *et al.*, 2006) and grating pitch. These two factors are affected by the ambient environmental fluctuations, such as temperature, strain, vibration, etc. (Guo, Xiao, Mrad & Yao, 2011).

Strain gauges are common for wide structural health monitoring practices as they are low-cost and easy-to-attach devices. They also have a high sensitivity which enables early detection of miniature flaws. The gauges are mounted on the object by an appropriate adhesive and its electrical conductance is highly dependence on its flexible geometry. When elastically deformed, the resistance of the gauge alters, thus the amount of enforced strain is determined (Choi *et al.*, 2008).

These transducers transmute electrical signal into ultrasonic disturbances and conversely. In addition, they provide health evaluation in either “transmit” (active) or “receive” (passive) modes of wave propagation within the structure. The types of these guided waves are discussed in details in the following chapter.

2. Elastic Waves

Elastic waves are disturbances propagating within a medium that has the properties of inertia and elasticity. When a solid is distorted by forced vibrations, its particles oscillate about their equilibrium positions. The disturbance energy is quickly transmitted between neighboring molecules causing mechanical stresses to build up. If the particles vibrate in the same direction as the motion of the wave, the interatomic forces are tensile and compressive. In addition, lateral displacement also occurs as a result of shear loads. Due to the inherent elastic behavior of the material, restoration forces react autonomously to resume the initial shape. Pressure, shear, flexural, Rayleigh and Lamb are the common types of elastic waves. (Yu, 2006).

The wave's category is determined by the propagation medium and wave profile. For instance, Lamb waves are ultrasonic disturbances that spread over a surface of a plate of thickness comparable to the wavelength. In a one dimensional medium, straight-crested Lamb waves form, whereas circular-crested Lamb waves are recognized for two dimensional propagation.

2.1. Guided Lamb Waves

Lamb waves, also referred to as plate waves, are a powerful device to evaluate the condition of a material in a thin plate structure. They are also extensively implemented in non-destructive evaluation. Lamb waves are a guided wave type; the resulting fluctuations, from imposed a mechanical stress on a specimen under test, travel along the structures while guided by the boundaries. Accordingly, the loss of energy resulting from material interaction is kept at its lowest level. In structural health monitoring, Lamb waves are able to detect any damage within a structure using a sparse array of actuation

sensing points.

Like other types of disturbances, Lamb waves are produced in traction free plate's boundaries (the surfaces are free from external stress). However, these waves have only displacement along and orthogonal to the wave traveling direction (Jaeger *et al.*, 2009). Lamb waves occur when the wavelength is greater than or of the order of the plate thickness (Lahiri *et al.*, 2000 & David & Cheeke, 2012). For a high wavelength to thickness ratio, lamb waves are highly dispersive; numerous modes are produced. Dispersion means that the phase and group velocities are function of frequency.

Infinite Lamb wave propagation modes exist but the displacement of the material layers is mainly classified as symmetric and antisymmetric, as depicted in Figure 2.1. In symmetric modes, also referred as longitudinal mode shapes, the resultant displacement occurs along a direction parallel to the longitudinal axis of the structure. On the other hand, antisymmetric modes, known as flexural modes, are attributed to the dislocations in the transverse direction. The infinitely existing modes within the plate are recognized by their phase velocities. Dispersion curves of the velocity as a function of the frequency describe the propagation aspects of a wave.

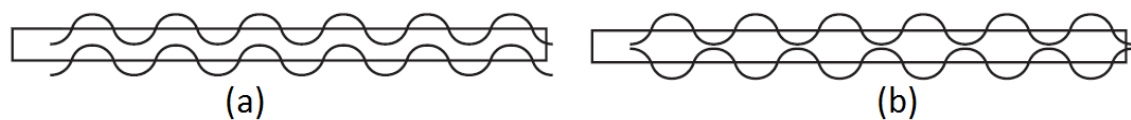


Figure 2.1. Lamb wave propagation modes; (a) antisymmetric; (b) symmetric

Active excitation approaches use guided lamb waves for the health monitoring of structures. For flaw detection, the pitch-catch or pulse-echo methods are used, depicted in Figure 2.2. In the pitch-catch technique, the actuation's source and sensor are located

from both sides of the defect, whereas for pulse-echo approach, the transducer on one side of the flaw acts as both wave emitter and receiver.

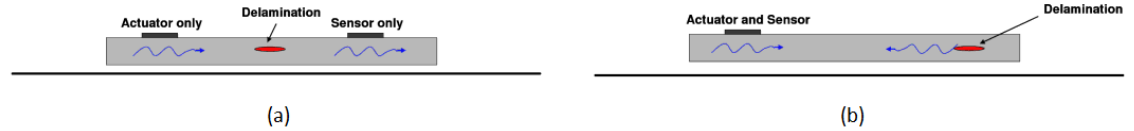


Figure 2.2. Lamb wave propagation for structural health monitoring of composite laminate using: (a) pitch-catch; (b) pulse-echo methods (Calomfirescu, 2008)

2.2. Wave Equations

A wave is the product of periodic disturbances of a vibrating source to a particle of the medium. Within a single period, the source displaces the excited particle in a sinusoidal, one cycle pattern. It moves upwards from the equilibrium position, back to rest, then, downwards from rest, and always ends up at the starting point which is considered its origin. The general wave equation is a hyperbolic, second-order, linear partial differential equation in terms of time and displacement. Therefore, the displacement profile can be determined by solving the equation subjected to the boundary conditions of the transmission medium. The material constituting the propagation platform has also tremendous influence on the final result. In the following, the solutions for isotropic and anisotropic media are sequentially derived.

2.2.1. Isotropic Circular Wave Equations

For an isotropic three dimensional body, the circular wave displacement equation, at a point $P(r, \theta)$ and time t , has the form of (Giurgiutiu, 2014) :

$$\nabla^2 u(r, \theta, t) = \frac{1}{c^2} \frac{\partial^2 u}{\partial t^2} \quad (2.1)$$

where:

u is the displacement function

t is time variable

c is the wave speed

∇ is the gradient

$\nabla^2 u(r, t)$ can be also written as:

$$\nabla^2 u(r, \theta, t) = \nabla^2 u = \frac{\partial^2 u}{\partial r^2} + \frac{1}{r} \frac{\partial u}{\partial r} + \frac{1}{r^2} \frac{\partial^2 u}{\partial \theta^2} \quad (2.2)$$

For circular symmetry, $u = u(r, t)$, thus:

$$\nabla^2 u(r, t) = \nabla^2 u = \frac{\partial^2 u}{\partial r^2} + \frac{1}{r} \frac{\partial u}{\partial r} \quad (2.3)$$

Equating Equation (2.1) to (2.3):

$$\frac{\partial^2 u}{\partial r^2} + \frac{1}{r} \frac{\partial u}{\partial r} = \frac{1}{c^2} \frac{\partial^2 u}{\partial t^2} \quad (2.4)$$

When $r \gg 1$, Equation (2.3) can be written as:

$$\nabla^2 u(r, t) = \nabla^2 u = \frac{1}{\sqrt{r}} \frac{\partial^2 (u\sqrt{r})}{\partial r^2} + \frac{1}{4r^2} u \quad (2.5)$$

Proof:

$$\frac{\partial (u\sqrt{r})}{\partial r} = \frac{\partial u}{\partial r} \sqrt{r} + \frac{1}{2\sqrt{r}} u$$

$$\begin{aligned} \frac{\partial^2 (u\sqrt{r})}{\partial r^2} &= \frac{\partial}{\partial r} \left[\frac{\partial u}{\partial r} \sqrt{r} + \frac{1}{2\sqrt{r}} u \right] \\ &= \frac{\partial^2 u}{\partial r^2} \sqrt{r} + \frac{1}{2} \frac{1}{\sqrt{r}} \frac{\partial u}{\partial r} + \frac{1}{2} \frac{1}{\sqrt{r}} \frac{\partial u}{\partial r} - \frac{1}{4r} \frac{u}{\sqrt{r}} \\ &= \frac{\partial^2 u}{\partial r^2} \sqrt{r} + \frac{1}{\sqrt{r}} \frac{\partial u}{\partial r} - \frac{1}{4r} \frac{u}{\sqrt{r}} \\ &= \sqrt{r} \left[\frac{\partial^2 u}{\partial r^2} + \frac{1}{r} \frac{\partial u}{\partial r} - \frac{1}{4r^2} u \right] : (*) \end{aligned}$$

Divide both sides of Equation (*) by \sqrt{r} :

$$\frac{1}{\sqrt{r}} \frac{\partial^2 (u\sqrt{r})}{\partial r^2} = \frac{\partial^2 u}{\partial r^2} + \frac{1}{r} \frac{\partial u}{\partial r} - \frac{1}{4r^2} u$$

or from Equation (2.3): $\nabla^2 u = \frac{\partial^2 u}{\partial r^2} + \frac{1}{r} \frac{\partial u}{\partial r}$

Thus, $\frac{1}{\sqrt{r}} \frac{\partial^2(u\sqrt{r})}{\partial r^2} = \nabla^2 u - \frac{1}{4} \frac{u}{r^2} : (**)$

Adding $\frac{1}{4} \frac{u}{r^2}$ to both sides of Equation (**):

$$\nabla^2 u = \frac{1}{\sqrt{r}} \frac{\partial^2(u\sqrt{r})}{\partial r^2} + \frac{1}{4} \frac{u}{r^2}$$

Thus, Equation (2.4) becomes:

$$\nabla^2 u = \frac{1}{\sqrt{r}} \frac{\partial^2(u\sqrt{r})}{\partial r^2} + \frac{1}{4r^2} u = \frac{1}{c^2} \frac{\partial^2 u}{\partial t^2} \quad (2.6)$$

The d'Alembert solution to Equation (2.5) is given by:

$$\sqrt{r} u(r, t) = f(r - ct) + g(r + ct) \quad (2.7)$$

As the waves propagate in an outward direction from the emission source, $g(r + ct) = 0$ and $\sqrt{r} u(r, t)$ reduces to:

$$\sqrt{r} u(r, t) = f(r - ct) \quad (2.8)$$

Dividing both sides of Equation (2.8) by \sqrt{r} :

$$u(r, t) = \frac{1}{\sqrt{r}} f(r - ct) \quad (2.9)$$

For a generic wave, the displacement vector is expressed by:

$$\vec{u}(r, t) = \frac{\vec{A}}{\sqrt{r}} f(r - ct) \quad (2.10)$$

Where \vec{u} and \vec{A} have component in r and θ directions.

For harmonic circular waves, equation (2.6) is solved by separation of variables method:

$$u(\vec{r}, t)\sqrt{r} = B e^{-i(\vec{k} \cdot \vec{r} + \omega t)} + C e^{i(\vec{k} \cdot \vec{r} - \omega t)} \quad (2.11)$$

where

B and C are the displacement amplitudes

ω is the angular frequency, $\omega=2\pi f$

\vec{k} is the wave vector

\vec{r} is the displacement vector

Again, as the waves propagate in an outward direction from the emission source, $gB e^{-i(\vec{k}\cdot\vec{r}+\omega t)} = 0$ and $u(\vec{r}, t)\sqrt{r}$ reduces to:

$$u(\vec{r}, t)\sqrt{r} = C e^{i(\vec{k}\cdot\vec{r}-\omega t)} \quad (2.12)$$

Dividing both sides of Equation (2.12) by \sqrt{r} :

$$u(\vec{r}, t) = \frac{C}{\sqrt{r}} e^{i(\vec{k}\cdot\vec{r}-\omega t)} \quad (2.13)$$

Equation (2.13) can be also replaced by:

$$u(\vec{r}, t) = \frac{C}{\sqrt{r}} e^{i(\omega t - \vec{k}\cdot\vec{r})} \quad (2.14)$$

Proof:

$$e^{i(\vec{k}\cdot\vec{r}-\omega t)} = \cos(\vec{k}\cdot\vec{r} - \omega t) + i \sin(\vec{k}\cdot\vec{r} - \omega t)$$

Thus Equation (2.13) can be written as:

$$u(\vec{r}, t) = \frac{C}{\sqrt{r}} e^{i(\vec{k}\cdot\vec{r}-\omega t)} = \frac{C}{\sqrt{r}} [\cos(\vec{k}\cdot\vec{r} - \omega t) + i \sin(\vec{k}\cdot\vec{r} - \omega t)]$$

But the displacement cannot be complex, therefore:

$$\begin{aligned} u(\vec{r}, t) &= \frac{C}{\sqrt{r}} e^{i(\vec{k}\cdot\vec{r}-\omega t)} = \frac{C}{\sqrt{r}} \cos(\vec{k}\cdot\vec{r} - \omega t) \\ &= \frac{C}{\sqrt{r}} \cos[-(\vec{k}\cdot\vec{r} - \omega t)] \\ &= \frac{C}{\sqrt{r}} \cos(\omega t - \vec{k}\cdot\vec{r}) \end{aligned}$$

Again $u(\vec{r}, t)$ can be expressed in exponential form by:

$$u(\vec{r}, t) = \frac{C}{\sqrt{r}} e^{i(\omega t - \vec{k} \cdot \vec{r})}$$

The wave front, plotted in Figure 2.3, is the group of points in the wave having the same phase after time t has elapsed. The wave front at distance r from the point source is given by:

$$\vec{k} \cdot \vec{r} = \text{constant} \quad (2.15)$$

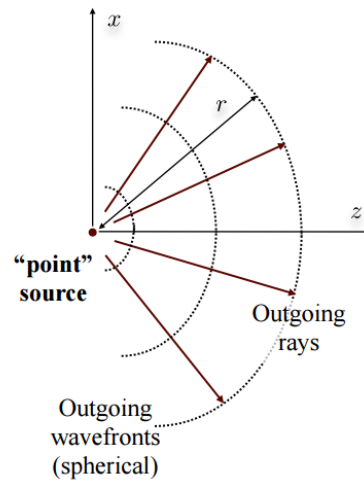


Figure 2.3. Circular wave fronts produced by a single point source in a two-dimensional plane

The magnitude of the wave vector is given in terms of wavelength λ by:

$$k = |\vec{k}| = \frac{2\pi}{\lambda} \quad (2.16)$$

Proof:

Let $\vec{k} = k_r \vec{e}_r$ and $\vec{r} = r \vec{e}_r$

Thus, $\vec{k} \cdot \vec{r} = r \cdot k : (*)$

Substituting (*) in (2.13):

$$u(\vec{r}, t) = \frac{A}{\sqrt{r}} e^{i(\omega t - r.k)} : (**)$$

Deriving (**) and replacing in (2.6):

$$\frac{\partial(u\sqrt{r})}{\partial r} = -k.i.A. e^{i(\omega t - r.k)}$$

$$\frac{\partial^2(u\sqrt{r})}{\partial r^2} = -k^2.A. e^{i(\omega t - r.k)}$$

$$\frac{1}{\sqrt{r}} \frac{\partial^2(u\sqrt{r})}{\partial r^2} = -\frac{1}{\sqrt{r}} . k^2 . A . e^{i(\omega t - r.k)}$$

and

$$\frac{1}{4r^2} u = \frac{1}{4r^2} \frac{A}{\sqrt{r}} e^{i(\omega t - r.k)}$$

Thus,

$$\begin{aligned} \frac{1}{\sqrt{r}} \frac{\partial^2(u\sqrt{r})}{\partial r^2} + \frac{1}{4r^2} u &= -\frac{1}{\sqrt{r}} . k^2 . A . e^{i(\omega t - r.k)} + \frac{1}{4r^2} \frac{A}{\sqrt{r}} e^{i(\omega t - r.k)} \\ &= e^{i(\omega t - r.k)} \left[-\frac{1}{\sqrt{r}} . k^2 . A + \frac{1}{4r^2} \frac{A}{\sqrt{r}} \right] : (#) \end{aligned}$$

On the other hand,

$$\frac{1}{c^2} \frac{\partial^2 u}{\partial t^2} = \frac{\omega^2}{c^2} \frac{A}{\sqrt{r}} e^{i(\omega t - r.k)} : (##)$$

Equating Equations (#) to (##) yields:

$$\begin{aligned} e^{i(\omega t - r.k)} \left[-\frac{1}{\sqrt{r}} . k^2 . A + \frac{1}{4r^2} \frac{A}{\sqrt{r}} \right] &= \frac{\omega^2}{c^2} \frac{A}{\sqrt{r}} e^{i(\omega t - r.k)} \rightarrow \\ -\frac{1}{\sqrt{r}} . k^2 . A + \frac{1}{4r^2} \frac{A}{\sqrt{r}} &= \frac{\omega^2}{c^2} \frac{A}{\sqrt{r}} \approx -\frac{1}{\sqrt{r}} . k^2 . A \text{ when } r \gg 1 \end{aligned}$$

Therefore,

$$k^2 = \frac{\omega^2}{c^2}$$

Square rooting both sides:

$$k = \frac{\omega}{c}$$

Or $\omega = 2\pi f$ and $c = \lambda f$ thus:

$$k = \frac{2\pi f}{\lambda f} = \frac{2\pi}{\lambda}$$

2.2.2. Anisotropic Wave Equations

The stress-strain relationship for orthotropic material in its local coordinate system is given by:

$$\begin{bmatrix} \sigma_1 \\ \sigma_2 \\ \sigma_3 \\ \tau_{23} \\ \tau_{13} \\ \tau_{12} \end{bmatrix} = \begin{bmatrix} \overline{C}_{11} & \overline{C}_{12} & \overline{C}_{13} & 0 & 0 & 0 \\ \overline{C}_{12} & \overline{C}_{22} & \overline{C}_{23} & 0 & 0 & 0 \\ \overline{C}_{13} & \overline{C}_{23} & \overline{C}_{33} & 0 & 0 & 0 \\ 0 & 0 & 0 & \overline{C}_{44} & 0 & 0 \\ 0 & 0 & 0 & 0 & \overline{C}_{55} & 0 \\ 0 & 0 & 0 & 0 & 0 & \overline{C}_{66} \end{bmatrix} \begin{bmatrix} \epsilon_1 \\ \epsilon_2 \\ \epsilon_3 \\ \epsilon_{23} \\ \epsilon_{13} \\ \epsilon_{12} \end{bmatrix} \quad (2.17)$$

Direction 1 is along the fibers and $[\overline{C}_{IJ}]$ is the local stiffness matrix.

Another stress-strain relation exists for a global coordinate system rotated by an angle α from the local system. Denote by $[\beta_{IJ}]$ the transformation matrix. Thus, the global stiffness matrix is obtained from the relation:

$$[C_{IJ}] = [\beta_{IJ}]^{-1} [\overline{C}_{IJ}] [\beta_{IJ}]^{-T} \quad (2.18)$$

where

$$[\beta_{IJ}] = \begin{bmatrix} \cos \alpha & \sin \alpha & 0 & 0 & 0 & 0 \\ -\sin \alpha & \cos \alpha & 0 & 0 & 0 & 0 \\ 0 & 0 & 1 & 0 & 0 & 0 \\ 0 & 0 & 0 & \cos \alpha & \sin \alpha & 0 \\ 0 & 0 & 0 & -\sin \alpha & \cos \alpha & 0 \\ 0 & 0 & 0 & 0 & 0 & 1 \end{bmatrix} \quad (2.19)$$

and

$$[C_{IJ}] = \begin{bmatrix} C_{11} & C_{12} & C_{13} & 0 & 0 & C_{16} \\ C_{12} & C_{22} & C_{23} & 0 & 0 & C_{26} \\ C_{13} & C_{23} & C_{33} & 0 & 0 & C_{36} \\ 0 & 0 & 0 & C_{44} & C_{45} & 0 \\ 0 & 0 & 0 & C_{45} & C_{55} & 0 \\ C_{16} & C_{26} & C_{36} & 0 & 0 & C_{66} \end{bmatrix} \quad (2.20)$$

Referring to Rokhlin *et al.* (2011), the guided wave equation for a uniaxial laminate is portrayed by:

$$\rho_s \frac{\partial^2 u_i}{\partial t^2} = c_{ijkl} \frac{\partial^2 u_k}{\partial x_j \partial x_l}; i=1,2,3 \quad (2.21)$$

Because of the anisotropic nature of composites, the wave components (longitudinal and transversal) cannot be separated. Composite laminates experience two quasi-shear and one quasi-longitudinal modes. The solution to equation (2.21) is given by (Rokhlin *et al.*, 2011):

$$u^k = U^k e^{[i(\zeta_p x_1 + \alpha^k x_3 - \zeta_p V_p t)]} \quad (2.22)$$

where

V_p is the phase velocity

ζ_p is the wave vector projection into the x_1 axis

α^k is the x_3 partial component of the partial wave vector

u^k is the wave displacement

U^k is the amplitude of wave displacement

k is the index of the partial wave modes. $k=1,2,\dots,6$

ρ_s is the volumetric density

The amplitude U^k and the x_3 partial component of the partial wave vector α^k are

calculated from solving the system below (Rokhlin *et al.*, 2011):

$$\begin{bmatrix} A + C_{55}\overline{\alpha}^{k^2} & C_{16} + C_{45}\overline{\alpha}^{k^2} & (C_{13} + C_{55})\overline{\alpha}^k \\ C_{16} + C_{45}\overline{\alpha}^{k^2} & B + C_{44}\overline{\alpha}^{k^2} & (C_{36} + C_{45})\overline{\alpha}^k \\ (C_{13} + C_{55})\overline{\alpha}^k & (C_{36} + C_{45})\overline{\alpha}^k & D + C_{33}\overline{\alpha}^{k^2} \end{bmatrix} \begin{bmatrix} U_1^k \\ U_2^k \\ U_3^k \end{bmatrix} = \begin{bmatrix} 0 \\ 0 \\ 0 \end{bmatrix} \quad (2.23)$$

where:

$$\overline{\alpha}^k = \frac{\alpha^k}{\zeta_p}$$

$$A = C_{11} - \rho_s V_p^2$$

$$B = C_{66} - \rho_s V_p^2$$

$$C = C_{55} - \rho_s V_p^2$$

Equation (2.23) is an eigen value and vector problem. First the determinant of the left hand side matrix is set to zero to calculate $\overline{\alpha}^k$, then the components of the displacement vector U_i^k are computed.

2.3. Phase and Group Velocity and Slowness Curve

The wave velocity expression is controversial because it is defined in many ways depending on the aspect of interest. Any given type of physical waves propagating in a solid medium is characterized by what is called group and phase velocities and slowness curves. This is due to the existing dispersion relation between the wave number and the frequency of waves.

The phase velocity is defined as the rate of the phase propagation in a given space. For instance, determine an emission point and locate two points on a medium at a known distance from each other, as depicted in Figure 2.4. The phase velocity is the ratio of this distance over the elapsed time required for any point of the disturbance signal in Figure 2.5 to travel from the first point to the second denoted respectively A and B.

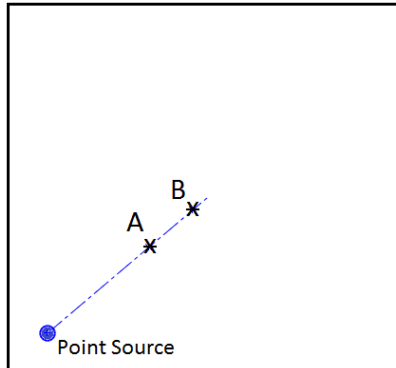


Figure 2.4. Two dimensional plate with single point sources and two sensing nodes A and B in space domain

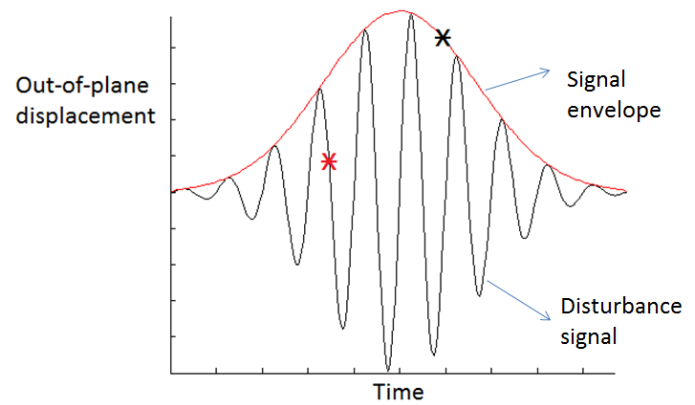


Figure 2.5. Out-of-plane displacement of a disturbance signal in time domain

The phase velocity is expressed in function of the wavelength λ and period T by:

$$v_p = \frac{\lambda}{T} \quad (2.24)$$

But

$$\text{From equation (2.6), } k = \frac{2\pi}{\lambda} \rightarrow \lambda = \frac{2\pi}{k}$$

$$\text{The frequency } f \text{ is the inverse of the period } T: f = \frac{1}{T}$$

Thus, the other forms of phase velocity are given by:

$$v_p = \lambda f = \frac{\omega}{k} \quad (2.25)$$

The slowness curve is the inverse plot ($1/v_p$) of the phase velocity profile.

On the other hand, the group velocity is the velocity of propagation of the envelope of a signal. The group velocity is a first order derivative of angular frequency ω with respect to the wave number k:

$$v_g = \begin{cases} \frac{\partial \omega}{\partial k} & \text{if isotropic} \\ \frac{\partial \omega}{\partial k_i} & \text{if anisotropic} \end{cases} \quad (2.26)$$

For composites, the wave number k_i is dependent on the varying wavefront's outward normal vector n_i . The wave number k_i is written as:

$$k_i = \frac{\omega}{v_p} n_i \quad (2.27)$$

Similarly to the phase velocity, for a point on the envelope in Figure 2.5, the group velocity is estimated by dividing the distance over the required travel time.

2.4. Skew Angle

The skew angle is solely a property of anisotropic solids. It is demarcated as the deviation of the propagating signal from the steered angle. To avoid this undesirable effect, the emitted wave has to travel in symmetric directions. For instance, in unidirectional laminates, the harmless directions are those parallel and perpendicular to the fibers (Rose, 2012).

2.5. Dispersion Curves for a Traction Free Plate

The dispersion curves are the first step of data processing of surface waves. Dispersion equations relate wave number to angular frequency, phase velocity to frequency and group velocity to frequency. For comparison, the symmetric and antisymmetric modes are schemed on the same chart of Figure 2.6. As the same manner as the solution of wave equation, dispersion relations differ between various materials.

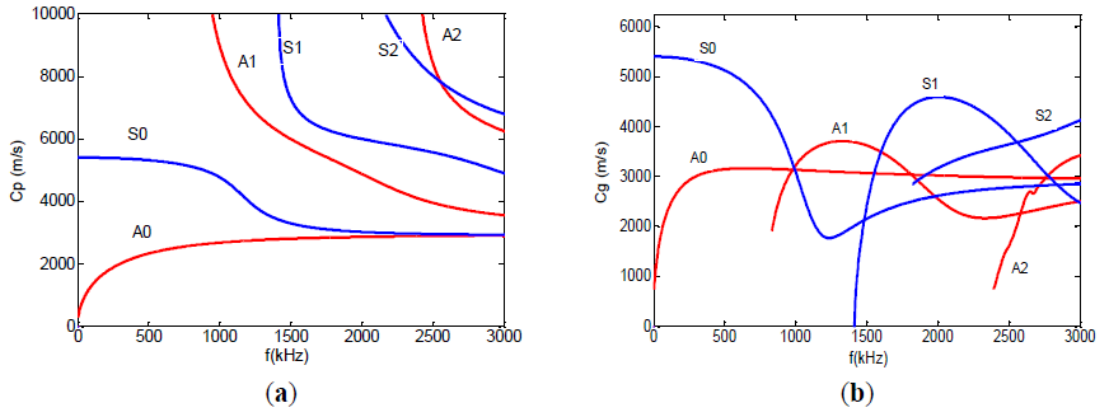


Figure 2.6. Free boundaries 2 mm aluminum plate dispersion relations; (a) phase velocity; (b) group velocity curves (Wan *et al.*, 2014)

2.5.1. Isotropic Medium

For the free plate problem, the dispersion relations are obtained by solving the equation of motion (Rose, 1999):

$$\mu u_{i,jj} + (\mu + \lambda) u_{j,ii} + \rho f_i = \rho \ddot{u}_i \quad (2.28)$$

where

μ, λ are Lamé constants

ρ is the volumetric density

f_i are the body forces. $i=1,2,3$

u_j are the displacements. $j=1,2,3$

Equation (2.28) can be solved either by the method of potentials or by the partial wave technique (Rose, 1999). However, both approaches will lead to the same findings. The potentials method uncouples the longitudinal from the transverse wave partial differential. Assuming ϕ and ψ the displacements along and perpendicular to the wave direction respectively, the disturbance equations are given by (Rose, 1999, Giurgiutiu, 2005 & Cardona *et al.*, 2008):

$$\begin{cases} \frac{\partial^2 \phi}{\partial x_1^2} + \frac{\partial^2 \phi}{\partial x_3^2} = \frac{1}{C_L^2} \frac{\partial^2 \phi}{\partial t^2}; \text{ for longitudinal waves} \\ \frac{\partial^2 \psi}{\partial x_1^2} + \frac{\partial^2 \psi}{\partial x_3^2} = \frac{1}{C_T^2} \frac{\partial^2 \psi}{\partial t^2}; \text{ for shear waves} \end{cases} \quad (2.29)$$

To start solving the system of equations (2.29), ϕ and ψ are set as:

$$\phi = \phi(x_3) e^{i(kx_3 - \omega t)} \quad (2.30)$$

and

$$\psi = \psi(x_3) e^{i(kx_3 - \omega t)} \quad (2.31)$$

On the other hand, the partial wave technique (Rose, 1999) offers a direct, general solution to Equation (2.28) by assuming the displacement expression of a partial wave as:

$$u_j = a_j e^{ik(x - \frac{k_z}{k_x} z)} \quad (2.32)$$

The overall displacement of the whole wave is a combination of the partial waves and is given by:

$$u_j = \sum_{n=1}^6 C_n \alpha_j^{(n)} e^{ik[x - (\frac{k_z}{k_x})^{(n)} z]} \quad (2.33)$$

The solution of both methods leads to the obtention of what is called Rayleigh-lamb frequency equations for the symmetric and anti-symmetric modes, depicted in Equation (2.24).

$$\begin{cases} \frac{\tan(qh)}{\tan(ph)} = -\frac{4k^2 pq}{(q^2 - k^2)^2}; \text{ for symmetric modes} \\ \frac{\tan(qh)}{\tan(ph)} = -\frac{(q^2 - k^2)^2}{4k^2 pq}; \text{ for antisymmetric modes} \end{cases} \quad (2.34)$$

The constants p and q are expressed in terms of wave number k and angular velocity ω :

$$p = \left(\frac{\omega}{c_L}\right)^2 - k^2 \quad (2.35)$$

and

$$q = \left(\frac{\omega}{c_T}\right)^2 - k^2 \quad (2.36)$$

Each equation of (2.34) is solved separately by means of root finding algorithms such as Newton-Raphson, bisection, etc.

2.5.2. Anisotropic Medium

For an anisotropic medium, the determination of the dispersion relations is more complicated than that of aluminium. Assuming a symmetry plane parallel to the laminate surfaces, Yan and Thompson (1990) derived a generalized Lamb-Rayleigh dispersion relation for the anisotropic case. Later, various methods have been investigated and tested for more general cases; The basic approaches are: Transfer Matrix Method (TMM) (Kamal & Giurgiutiu, 2014 & Pant, 2014), Stiffness Matrix Method (SMM) (Kamal & Giurgiutiu, 2014), Global Matrix Method (GMM) (Kamal & Giurgiutiu, 2014 & Pant, 2014), Semi Analytical Finite Element (SAFE) (Ahmad *et al.*, 2013 & Kamal & Giurgiutiu, 2014), Local Interaction Simulation Approach (LISA) (Kamal & Giurgiutiu, 2014), the Equivalent Matrix Method (EMM) (Kamal & Giurgiutiu, 2014) and the 3D elasticity theory (Wang & Yuan, 2007).

Each stated algorithm has drawbacks and strengths. For this reason, Kamal and Giurgiutiu (2014) thought about a combination of the transfer and stiffness matrix method (STMM) to fill the deficiency gap of both processes.

For N-layered laminates, Cardona *et al.* (2008) also developed a numerical

solution algorithm with global convergence based on the bisection criteria able to plot the dispersion curve point by point.

3. Beamforming Presentation

Beamforming, also known as spatial filtering, is a signal processing employed to orient the radiated waves toward a priority track. When two or more point sources superpose, resultant waves are produced. The emitted signals interfere with one another constructively in some directions and destructively in the others, as shown in Figure 3.1. Constructive interference is achieved when the travelling pulses arrive at their destination in phase. The difference between two crests, d , is an integer, n , multiple of wave length, λ , ($d=n\lambda$). The resultant wave, therefore, has an amplitude equal to the sum of the wave amplitudes. On the opposite side, destructive interference occurs when the waves are out of phase. Such sinusoidal signals cancel out as every crest is opposed by a trough making “nulls.” The phase difference is expressed by $d=(n-\frac{1}{2})\lambda$.

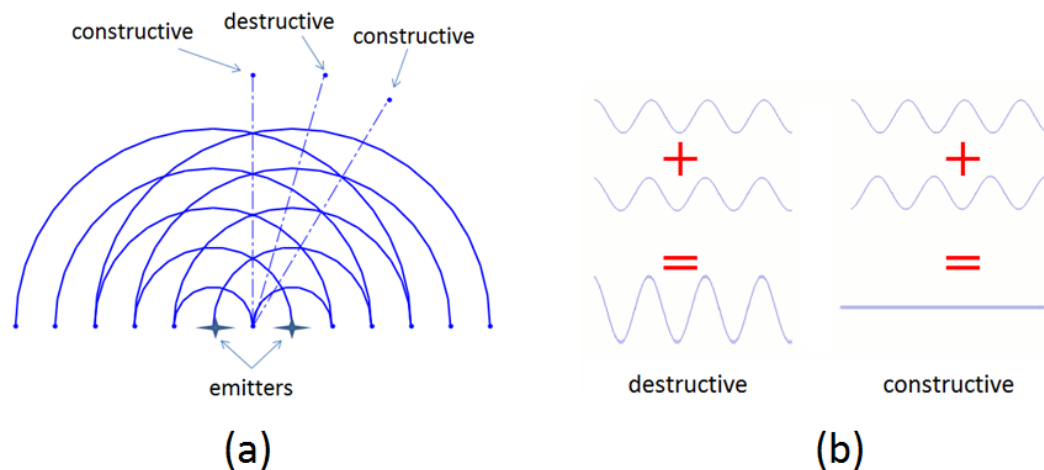


Figure 3.1. Wave interference from two point sources: (a) top view; (b) constructive and destructive out-of-plane displacement profile

In the radiation diagram, the field strength is not uniform and three major kinds of lobes are formed. These are the main, grating and side lobes separated by minimums (nulls) as depicted in Figure 3.2. The main lobe has the maximum power and is in the

direction of scanning. The grating lobe, also referred to as the back lobe, is an unintended beam opposing the main lobe. Sidelobes are the result of constructive interference, but of less amplitude than other lobes.

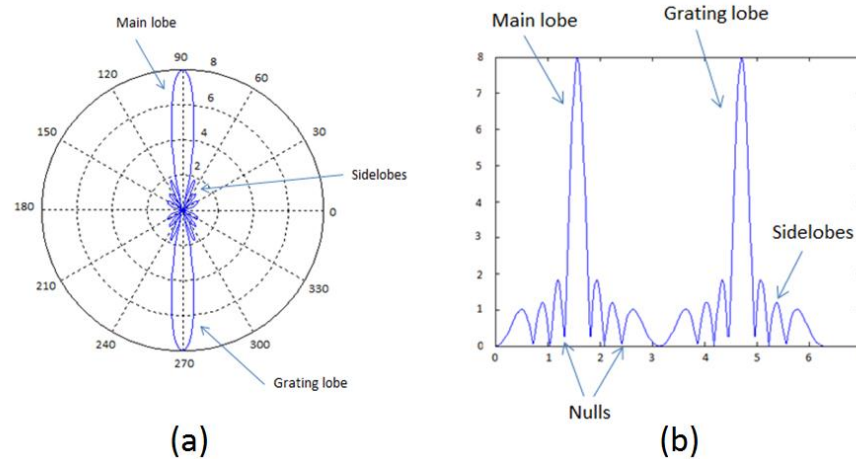


Figure 3.2. Focused directional radiation pattern of linear array: (a) Left-In polar coordinates; (b) Cartesian coordinates (MATLAB R2011a)

The wave propagation profile is highly dependent on the material type and target position. Usually, circular or distorted rings moving harmoniously, like when dropping a pebble into calm water, are seen to occur. When interacting with a solid medium, the spreading signals experience dispersion and loss of energy. For aluminum, analogous wave translation is observed in all directions at any time. However, in anisotropic materials such as composites, waves have the tendency to migrate more easily along the fiber directions. The emitted waves can also reach points in the near as well as the far fields. The main difference between these two approaches is related to the shape of the wave front. As shown in Figure 3.3, for a destination far away from the emission source, the wave front is approximately flat, whereas for closer targets, the curvature can still be noticed.

It is difficult to determine the exact range of a near or far field, but the direction of

propagation can be determined (Lingyu,2006). Referring to the theory of antennas, Lingyu (2006) gives a conventional estimation of the field by the inequalities:

- $0.62 \sqrt{\frac{D^3}{\lambda}} < r_{near} \leq 2 \frac{D^2}{\lambda}$
- $r_{far} > 2 \frac{D^2}{\lambda}$

where D and λ stand for the diameter of the aperture enclosing the actuation points and the wave length respectively. r_{near} designates the radius for the nearfield starting region and r_{far} that of the far field. The term $(\frac{2D^2}{\lambda})$ is the transition radius between the two domains.

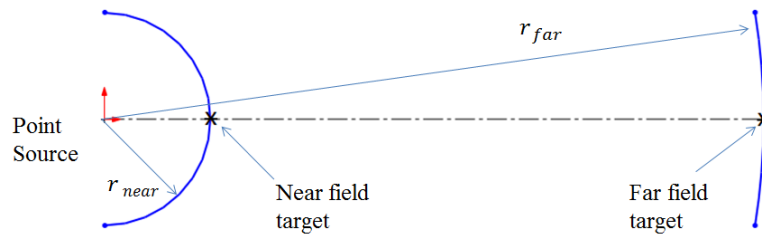


Figure 3.3. Wave front in the near and far fields respectively

3.1. Formulation of Wave Beamforming from Multiple Excitation Sources in an Anisotropic Medium:

In order to identify the damage location, a time domain approach using several ultrasonic wave emissions is proposed. The excitations positioning, weight and phase shift have a great influence of the directivity and shaping of the resultant beam. These conditions also vary with target location. Osterc and Kim (2013) developed a model of beamforming applicable for quasi-isotropic composites. For simplification, their study did not account for the amplitude variation with direction. In the following context, the

complete beamforming equations are derived for simultaneous and successive excitations. The two scanned fields are also distinguished.

3.1.1. Simultaneous Excitations (No Delay):

In this section, it will be assumed that the emitting sources are fired at the same time. Accordingly, a definite beam cannot be formed. Instead, the array factor function is determined. This presumption does not actually apply for real life practices, although it is an appropriate starting point. It enables better understanding of the time-delayed excitations later.

Near Field:

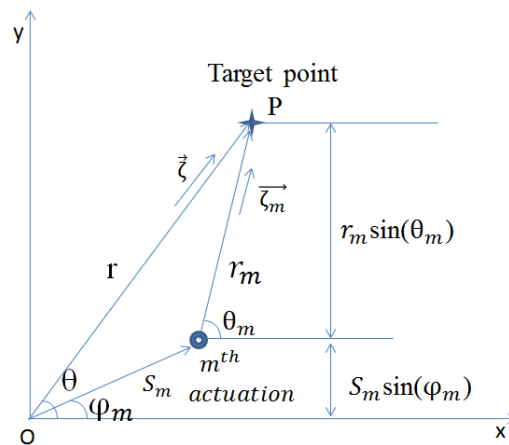


Figure 3.4. Near field schema for single actuation point

The out-of-plane displacement expression of the disturbance emitted from the m^{th} actuation, shown in Figure 3.4 is defined by:

$$y_m(t) = f(\vec{r}_m, t) = \frac{A(\theta_m)}{\sqrt{r_m}} e^{i(\omega t - \vec{k}_m \cdot \vec{r}_m)} \quad (3.1)$$

The expression of the wave number \vec{k}_m can be written as follows:

$$\vec{k}_m = \vec{\zeta}_m \cdot \frac{\omega}{c(\theta_m)} \quad (3.2)$$

Where $\vec{\zeta}_m$ is the unit vector of \vec{r}_m .

Replacing equation (3.2) in (3.1):

$$\begin{aligned} y_m(t) = f(\vec{r}_m, t) &= \frac{A(\theta_m)}{\sqrt{r_m}} e^{i(\omega t - \vec{\zeta}_m \cdot \frac{\omega}{c(\theta_m)} \cdot \vec{r}_m)} \\ &= \frac{A(\theta_m)}{\sqrt{r_m}} e^{i\omega(t - \vec{\zeta}_m \cdot \frac{\vec{r}_m}{c(\theta_m)})} \end{aligned} \quad (3.3)$$

Referring to Figure 3.4, it can be seen that:

$$\vec{r}_m = r_m \cdot \vec{\zeta}_m \quad (3.4)$$

Thus,

$$\vec{\zeta}_m \cdot \vec{r}_m = \vec{\zeta}_m \cdot (r_m \cdot \vec{\zeta}_m) = r_m \quad (3.5)$$

Plugging equation (3.5) in (3.3) yields:

$$y_m(t) = f(\vec{r}_m, t) = \frac{A(\theta_m)}{\sqrt{r_m}} e^{i\omega(t - \frac{r_m}{c(\theta_m)})} \quad (3.6)$$

Note that the general wavefront equation from the pattern's centroid is expressed by:

$$f(\vec{r}, t) = \frac{A(\theta)}{\sqrt{r}} e^{i(\omega t - \vec{k} \cdot \vec{r})} \quad (3.7)$$

where

$$\vec{k} = \vec{\zeta} \cdot \frac{\omega}{c(\theta)} \quad (3.8)$$

and

$$\vec{r} = r \cdot \vec{\zeta} \quad (3.9)$$

Repeating the same precedent process, Equation (3.7) becomes:

$$\begin{aligned}
 f(\vec{r}, t) &= \frac{A(\theta)}{\sqrt{r}} e^{i(\omega t - \vec{\zeta} \cdot \frac{\omega}{c(\theta)} \cdot r \cdot \vec{\zeta})} \\
 &= \frac{A(\theta)}{\sqrt{r}} e^{i(\omega t - \frac{\omega r}{c(\theta)})} \\
 &= \frac{A(\theta)}{\sqrt{r}} e^{i\omega(t - \frac{r}{c(\theta)})}
 \end{aligned} \tag{3.10}$$

Equations (3.6) and (3.10) can be related by the following:

$$f(\vec{r}_m, t) = \frac{A(\theta_m)}{A(\theta)} \frac{1}{\sqrt{\frac{r_m}{r}}} e^{i\omega(\frac{r}{c(\theta)} - \frac{r_m}{c(\theta_m)})} f(\vec{r}, t) \tag{3.11}$$

Proof:

$$\begin{aligned}
 \frac{f(\vec{r}_m, t)}{f(\vec{r}, t)} &= \frac{\frac{A(\theta_m)}{\sqrt{r_m}} e^{i\omega(t - \frac{r_m}{c(\theta_m)})}}{\frac{A(\theta)}{\sqrt{r}} e^{i\omega(t - \frac{r}{c(\theta)})}} = \frac{A(\theta_m)}{\sqrt{r_m}} \frac{\sqrt{r}}{A(\theta)} e^{i\omega(\frac{r}{c(\theta)} - \frac{r_m}{c(\theta_m)})} \\
 &= \frac{A(\theta_m)}{A(\theta)} \frac{1}{\sqrt{\frac{r_m}{r}}} e^{i\omega(\frac{r}{c(\theta)} - \frac{r_m}{c(\theta_m)})}
 \end{aligned}$$

Thus, by multiplying both sides by $f(\vec{r}, t)$:

$$f(\vec{r}_m, t) = \frac{A(\theta_m)}{A(\theta)} \frac{1}{\sqrt{\frac{r_m}{r}}} e^{i\omega(\frac{r}{c(\theta)} - \frac{r_m}{c(\theta_m)})} f(\vec{r}, t)$$

The synthetic wavefront resulting from a total number M of actuations is determined by:

$$z(\vec{r}, t) = \sum_{m=1}^M \omega_m y_m(t) = \sum_{m=1}^M \omega_m f(\vec{r}_m, t) \tag{3.12}$$

Replacing (3.11) in (3.12):

$$z(\vec{r}, t) = \sum_{m=1}^M \omega_m y_m(t) = \sum_{m=1}^M \omega_m f(\vec{r}_m, t)$$

$$= \sum_{m=1}^M \omega_m \frac{A(\theta_m)}{A(\theta)} \frac{1}{\sqrt{\frac{r_m}{r}}} e^{i\omega(\frac{r}{c(\theta)} - \frac{r_m}{c(\theta_m)})} f(\vec{r}, t) \quad (3.13)$$

For an array of identical elements, the radiation pattern is calculated from the pattern multiplication theorem:

$$\text{Array pattern} = \text{Array element pattern} \times \text{Array Factor (AF)}$$

where the array element pattern is the pattern produced by a single element of the array.

Taking the constant entities out of the summation in equation (3.13):

$$\begin{aligned} z(\vec{r}, t) &= f(\vec{r}, t) \sum_{m=1}^M \omega_m \frac{A(\theta_m)}{A(\theta)} \frac{1}{\sqrt{\frac{r_m}{r}}} e^{i\omega(\frac{r}{c(\theta)} - \frac{r_m}{c(\theta_m)})} \\ &= f(\vec{r}, t) \cdot AF(\theta) \end{aligned} \quad (3.14)$$

Here, the array factor AF assumes that all the point sources are identical.

The generic Array Factor expression is given by:

$$AF(\theta) = \sum_{m=1}^M \omega_m \frac{A(\theta_m)}{A(\theta)} \frac{1}{\sqrt{\frac{r_m}{r}}} e^{i\omega(\frac{r}{c(\theta)} - \frac{r_m}{c(\theta_m)})} \quad (3.15)$$

In particular, set the weighting factor ω_m equal to 1 ($\omega_m = 1$), Equation (3.15) becomes:

$$AF(\theta) = \sum_{m=1}^M \frac{A(\theta_m)}{A(\theta)} \frac{1}{\sqrt{\frac{r_m}{r}}} e^{i\omega(\frac{r}{c(\theta)} - \frac{r_m}{c(\theta_m)})} \quad (3.16)$$

The expression of angular frequency ω in terms of frequency f is:

$$\omega = 2\pi f \quad (3.17)$$

Replacing Equation (3.17) in (3.16) gives:

$$AF(\theta) = \sum_{m=1}^M \frac{A(\theta_m)}{A(\theta)} \frac{1}{\sqrt{\frac{r_m}{r}}} e^{i2\pi f(\frac{r}{c(\theta)} - \frac{r_m}{c(\theta_m)})} \quad (3.18)$$

Finally, the normalized beamforming is obtained by dividing Equation (3.16) by the total number of actuators M . Thus:

$$AF(\theta)_{norm} = \frac{1}{M} \sum_{m=1}^M \frac{A(\theta_m)}{A(\theta)} \frac{1}{\sqrt{\frac{r_m}{r}}} e^{i2\pi f(\frac{r}{c(\theta)} - \frac{r_m}{c(\theta_m)})} \quad (3.19)$$

In Equation (3.19), r_m and θ_m should be expressed in terms of the excitation point's polar coordinates (S_m, φ_m) and the angle θ . From the geometry in Figure 3.4, by applying the cosine rule r_m is defined by:

$$r_m = \sqrt{S_m^2 + r^2 - 2rS_m \cos(\theta - \varphi_m)} \quad (3.20)$$

also

$$\theta_m = \sin^{-1} \left(\frac{r \sin(\theta) - S_m \sin(\varphi_m)}{\sqrt{S_m^2 + r^2 - 2rS_m \cos(\theta - \varphi_m)}} \right) \quad (3.21)$$

Proof:

From Figure 3.4, $r \sin(\theta) = S_m \sin(\varphi_m) + r_m \sin(\theta_m) \rightarrow$

$$\theta_m = \sin^{-1} \left[\frac{r \sin(\theta) - S_m \sin(\varphi_m)}{r_m} \right]$$

But r_m is given in Equation (3.20), thus:

$$\theta_m = \sin^{-1} \left[\frac{r \sin(\theta) - S_m \sin(\varphi_m)}{\sqrt{S_m^2 + r^2 - 2rS_m \cos(\theta - \varphi_m)}} \right]$$

Note that θ_m 's expression depends on the position of the m^{th} actuation in the four quadrants of the coordinate system. Let (x_m, y_m) be the Cartesian coordinates of the m^{th} focal point. The algorithm below defines θ_m in three conditional cases:

- if $x_m \geq 0$ and $y_m \geq 0$

$$\begin{aligned} & \text{if } 0^\circ \leq \theta < \sin^{-1} \left[\frac{S_m \sin(\varphi_m)}{r} \right] \\ & \quad \theta_m = \sin^{-1} \left[\frac{S_m \sin(\varphi_m) - r \sin(\theta)}{r_m} \right] \\ & \text{if } \sin^{-1} \left[\frac{S_m \sin(\varphi_m)}{r} \right] \leq \theta < 180^\circ \\ & \quad \theta_m = \sin^{-1} \left[\frac{r \sin(\theta) - S_m \sin(\varphi_m)}{r_m} \right] \\ & \text{if } 180^\circ \leq \theta \leq 360^\circ \\ & \quad \theta_m = \sin^{-1} \left[\frac{S_m \sin(\varphi_m) - r \sin(\theta)}{r_m} \right] \end{aligned}$$

- if $x_m < 0$ and $y_m > 0$

$$\begin{aligned} & \text{if } 0^\circ \leq \theta < \sin^{-1} \left[\frac{S_m \sin(\varphi_m)}{r} \right] \\ & \quad \theta_m = \sin^{-1} \left[\frac{S_m \sin(\varphi_m) - r \sin(\theta)}{r_m} \right] \\ & \text{if } \sin^{-1} \left[\frac{S_m \sin(\varphi_m)}{r} \right] \leq \theta < 180^\circ - \sin^{-1} \left[\frac{S_m \sin(\varphi_m)}{r} \right] \\ & \quad \theta_m = \sin^{-1} \left[\frac{r \sin(\theta) - S_m \sin(\varphi_m)}{r_m} \right] \\ & \text{if } 180^\circ - \sin^{-1} \left[\frac{S_m \sin(\varphi_m)}{r} \right] \leq \theta \leq 360^\circ \\ & \quad \theta_m = \sin^{-1} \left[\frac{S_m \sin(\varphi_m) - r \sin(\theta)}{r_m} \right] \end{aligned}$$

- if $(x_m < 0$ and $y_m < 0)$ or $(x_m > 0$ and $y_m < 0)$

$$\begin{aligned} & \text{if } 0^\circ \leq \theta < 180^\circ + \sin^{-1} \left[\frac{-S_m \sin(\varphi_m)}{r} \right] \\ & \quad \theta_m = \sin^{-1} \left[\frac{r \sin(\theta) - S_m \sin(\varphi_m)}{r_m} \right] \\ & \text{if } 180^\circ + \sin^{-1} \left[\frac{-S_m \sin(\varphi_m)}{r} \right] \leq \theta < 360^\circ - \sin^{-1} \left[\frac{-S_m \sin(\varphi_m)}{r} \right] \\ & \quad \theta_m = \sin^{-1} \left[\frac{S_m \sin(\varphi_m) - r \sin(\theta)}{r_m} \right] \\ & \text{if } 360^\circ - \sin^{-1} \left[\frac{-S_m \sin(\varphi_m)}{r} \right] \leq \theta \leq 360^\circ \\ & \quad \theta_m = \sin^{-1} \left[\frac{r \sin(\theta) - S_m \sin(\varphi_m)}{r_m} \right] \end{aligned}$$

Therefore, θ_m can be simply written as:

$$\theta_m = \sin^{-1} \left| \frac{S_m \sin(\varphi_m) - r \sin(\theta)}{r_m} \right|$$

The relation between the Cartesian and polar coordinates of the m^{th} excitation point is stated by:

$$x_m = S_m \cos(\varphi_m) ; y_m = S_m \sin(\varphi_m) \quad (3.22)$$

or

$$S_m = \sqrt{(x_m^2 + y_m^2)} ; \varphi_m = \tan^{-1}\left(\frac{y_m}{x_m}\right) \quad (3.23)$$

Far Field:

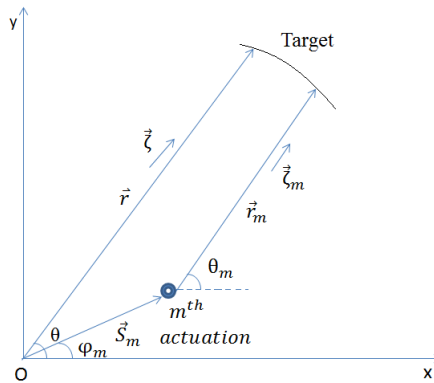


Figure 3.5. Far field schema for single actuation point

Although the target was a point in the near field, it is assumed that the wave front is flat if the target distance is far, as shown in Figure 3.5.

Assumptions:

$$\vec{z}_m \approx \vec{z} \text{ and } r_m \approx r \rightarrow c(\theta_m) \approx c(\theta) \text{ and } A(\theta_m) \approx A(\theta)$$

Then, Equation (3.2) gives:

$$\vec{k}_m = \vec{z}_m \cdot \frac{\omega}{c(\theta_m)} \approx \vec{z} \cdot \frac{\omega}{c(\theta)} = \vec{k} \quad (3.24)$$

Equation (3.3) becomes:

$$y_m(t) = f(\vec{r}_m, t) = \frac{A(\theta)}{\sqrt{r}} e^{i\omega(t - \vec{\zeta} \cdot \frac{\vec{r}_m}{c(\theta)})} \quad (3.25)$$

Note the vector relation:

$$\vec{r}_m = \vec{r} - \vec{s}_m \quad (3.26)$$

Plugging Equation (3.26) in (3.25):

$$f(\vec{r}_m, t) = \frac{A(\theta)}{\sqrt{r}} e^{i\omega(t - \vec{\zeta} \cdot \frac{\vec{r} - \vec{s}_m}{c(\theta)})} \quad (3.27)$$

As previously, $f(\vec{r}_m, t)$ and $f(\vec{r}, t)$ are also interrelated for far field by:

$$f(\vec{r}_m, t) = e^{i\frac{\omega}{c(\theta)} \vec{\zeta} \cdot \vec{s}_m} f(\vec{r}, t) \quad (3.28)$$

Proof:

$$\frac{f(\vec{r}_m, t)}{f(\vec{r}, t)} = \frac{\frac{A(\theta)}{\sqrt{r}} e^{i\omega(t - \vec{\zeta} \cdot \frac{\vec{r} - \vec{s}_m}{c(\theta)})}}{\frac{A(\theta)}{\sqrt{r}} e^{i\omega(t - \vec{\zeta} \cdot \frac{\vec{r}}{c(\theta)})}} = e^{i\omega(t - \vec{\zeta} \cdot \frac{\vec{r} - \vec{s}_m}{c(\theta)} - t + \vec{\zeta} \cdot \frac{\vec{r}}{c(\theta)})} = e^{i\frac{\omega}{c(\theta)} \vec{\zeta} \cdot \vec{s}_m}$$

Thus, by multiplying both sides by $f(\vec{r}, t)$:

$$f(\vec{r}_m, t) = e^{i\frac{\omega}{c(\theta)} \vec{\zeta} \cdot \vec{s}_m} f(\vec{r}, t)$$

Replacing $f(\vec{r}_m, t)$ of Equation (3.28) in the synthetic wavefront Equation (3.12) yields:

$$\begin{aligned} z(\vec{r}, t) &= \sum_{m=1}^M \omega_m y_m(t) = \sum_{m=1}^M \omega_m f(\vec{r}_m, t) \\ &= \sum_{m=1}^M \omega_m e^{i\frac{\omega}{c(\theta)} \vec{\zeta} \cdot \vec{s}_m} f(\vec{r}, t) \end{aligned} \quad (3.29)$$

Taking again the constant entity out of the summation:

$$z(\vec{r}, t) = f(\vec{r}, t) \sum_{m=1}^M \omega_m e^{i\frac{\omega}{c(\theta)} \vec{\zeta} \cdot \vec{s}_m} \quad (3.30)$$

The generic array factor expression is given by:

$$AF(\theta) = \sum_{m=1}^M \omega_m e^{i\frac{\omega}{c(\theta)} \vec{\zeta} \cdot \vec{s}_m} \quad (3.31)$$

In particular, set the weighting factor ω_m equal to 1 ($\omega_m = 1$), equation (3.31) becomes:

$$AF(\theta) = \sum_{m=1}^M e^{i\frac{\omega}{c(\theta)} \vec{\zeta} \cdot \vec{s}_m} \quad (3.32)$$

From the dot product relation:

$$\vec{\zeta} \cdot \vec{s}_m = S_m \cos(\theta - \varphi_m) \quad (3.33)$$

Replacing Equation (3.33) in (3.32) yields:

$$AF(\theta) = \sum_{m=1}^M e^{i\frac{\omega}{c(\theta)} S_m \cos(\theta - \varphi_m)} \quad (3.34)$$

Again, for normalization, divide the Array Factor equation by the total number of actuators:

$$AF(\theta)_{norm} = \frac{1}{M} \sum_{m=1}^M e^{i\frac{\omega}{c(\theta)} S_m \cos(\theta - \varphi_m)} \quad (3.35)$$

3.1.2. Successive Excitations (Time Delay Interval):

The previous concept applies when all the excitations are fired at the same time. The

generated waves, therefore, propagate likewise in all directions. But, in order to obtain an effective scanning, the wave front should be biased towards a certain angle. Producing excitations at varying time intervals controls the steering of the ultrasonic beam. The above exhibited method encounters slight changes to account for time suspension. The array factor (AF) is replaced by the term “Beamforming (BF)” in this case.

Let Δ_m be the corresponding time delays related to the M actuation points ($1 \leq m \leq M$). The synthetic wave front is redefined by:

$$z(\vec{r}, t) = \sum_{m=1}^M \omega_m y_m(t - \Delta_m) = \sum_{m=1}^M \omega_m f(\vec{r}_m, t - \Delta_m) \quad (3.36)$$

Near Field:

By repeating the same previous process, the beamforming factor for a steered beam becomes:

$$BF(\theta)_{norm} = \frac{1}{M} \sum_{m=1}^M \frac{A(\theta_m)}{A(\theta)} \frac{1}{\sqrt{\frac{r_m}{r}}} e^{i2\pi f \left(\frac{r}{c(\theta)} - \frac{r_m}{c(\theta_m)} - \Delta_m \right)} \quad (3.37)$$

The time delay Δ_m for a near field is given by:

$$\Delta_m = \frac{r}{c(\theta_0)} - \frac{r_{m0}}{c(\theta_{m0})} \quad (3.38)$$

Plugging Equation (3.38) into (3.37):

$$BF(\theta)_{norm} = \frac{1}{M} \sum_{m=1}^M \frac{A(\theta_m)}{A(\theta)} \frac{1}{\sqrt{\frac{r_m}{r}}} e^{i2\pi f \left[\frac{r}{c(\theta)} - \frac{r_m}{c(\theta_m)} - \left(\frac{r}{c(\theta_0)} - \frac{r_{m0}}{c(\theta_{m0})} \right) \right]} \quad (3.39)$$

where

θ_0 is the steering angle of the beam.

θ_{m0} is the angle formed by r_{m0} with the horizontal

r_{m0} is the distance from the m^{th} actuator to the target point at the defined direction

Similar to r_m and θ_m , r_{m0} and θ_{m0} are annotated in Figure 3.6, and respectively written as:

From cosine rule:

$$r_{m0} = \sqrt{S_m^2 + r^2 - 2rS_m \cos(\theta_0 - \varphi_m)} \quad (3.40)$$

and

$$\theta_{m0} = \sin^{-1} \left(\frac{r \sin(\theta_0) - S_m \sin(\varphi_m)}{\sqrt{S_m^2 + r^2 - 2rS_m \cos(\theta_0 - \varphi_m)}} \right) \quad (3.41)$$

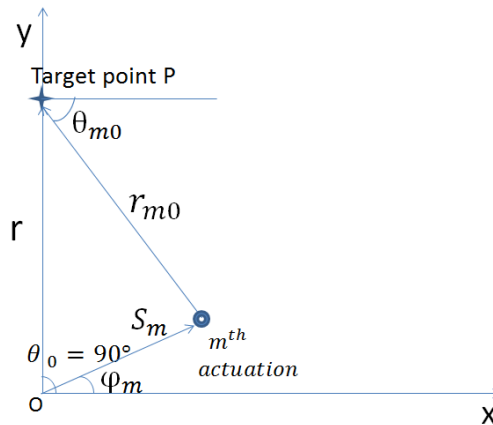


Figure 3.6. Schematic of near field for a single actuation point and a target at 90° direction

Far Field:

In a similar manner, the equation of beamforming factor for a far field with time delay is written as:

$$BF(\theta)_{norm} = \frac{1}{M} \sum_{m=1}^M e^{i\omega \left[\frac{S_m \cos(\theta - \varphi_m)}{c(\theta)} - \Delta_m \right]} \quad (3.42)$$

Let the time delay in this case be:

$$\Delta_m = \frac{S_m \cos(\theta_0 - \varphi_m)}{c(\theta_0)} \quad (3.43)$$

Therefore,

$$BF(\theta)_{norm} = \frac{1}{M} \sum_{m=1}^M e^{i\omega S_m \left[\frac{\cos(\theta - \varphi_m)}{c(\theta)} - \frac{\cos(\theta_0 - \varphi_m)}{c(\theta_0)} \right]} \quad (3.44)$$

3.2. Wave Beamforming from Multiple Excitation Sources in an Isotropic Medium:

The isotropic theory is a particular case of the general anisotropic principle. The same approach exhibited in the upper section applies but with some simplifications on the level of phase velocity and amplitude. The isotropic beamforming is already discussed by Yu and Giurgiutiu (2005), and Yu (2006).

For isotropic materials, the wave propagation is independent of direction. The front wave's velocity and amplitude reduce only with distance due to dissipative forces caused by the frictional molecular interaction of the generated vibrations within the material.

No time Delay:

Assumptions:

$$c(\theta) = c(\theta_m) = c \text{ and } A(\theta) = A(\theta_m) = A$$

Based on the assumptions, the array factor expressions of Equations (3.19) and (3.35) are shown below.

For the near field:

$$AF(\theta)_{norm} = \frac{1}{M} \sum_{m=1}^M \frac{1}{\sqrt{\frac{r_m}{r}}} e^{i2\pi f \left[\frac{r-r_m}{c} \right]} \quad (3.45)$$

For the far field:

$$AF(\theta)_{norm} = \frac{1}{M} \sum_{m=1}^M e^{i \frac{2\pi f}{c} S_m \cos(\theta - \varphi_m)} \quad (3.46)$$

With time Delay:

Assumptions:

$$c(\theta) = c(\theta_m) = c ; c(\theta_0) = c(\theta_{m0}) = c$$

$$A(\theta) = A(\theta_m) = A$$

Equation (3.38) becomes:

$$\Delta_m = \frac{r-r_m}{c} \quad (3.47)$$

Based on the assumptions, the transformed beamforming expressions of Equations (3.39) and (3.44) are shown below.

For the near field:

$$BF(\theta)_{norm} = \frac{1}{M} \sum_{m=1}^M \frac{1}{\sqrt{\frac{r_m}{r}}} e^{i2\pi f \left[\frac{r_{m0}-r_m}{c} \right]} \quad (3.48)$$

Note that Equations (3.20) and (3.40) stay also applicable for r_m and r_{m0} respectively in this section.

For the far field:

$$BF(\theta)_{norm} = \frac{1}{M} \sum_{m=1}^M e^{i\omega S_m \left[\frac{\cos(\theta - \varphi_m) - \cos(\theta_0 - \varphi_m)}{c} \right]} \quad (3.48)$$

4. Pattern Geometry

Phased array is a set of multiple sources of propagating waves. Arrays are commonly utilized to increase the overall gain (the power transmitted in the direction of peak radiation), maximize the signal and steer it in a particular direction. To achieve the desired radiation profile, the emitted signals are combined and processed. Several design variables can be adjusted to fulfill the purpose; these are the overall array shape and elements' spacing, the excitations' amplitudes and phase delays.

Arrays vary in geometry depending on their application. Uniformly spaced arrays with constant spacing between elements have been found attractive in ultrasonic applications. Uniform linear, circular, planar and multi-dimensional patterns are depicted in Figure 4.1. Such patterns are validated by theoretical analysis, experiments and/or simulations. It was concluded that by increasing the array size, the beamwidth reduces while grating lobes grow in undesirable directions (antenna-theory.com). Neighboring elements should be at maximum a half-wavelength apart to avoid "aliasing." This term is attributed to the phenomenon where two waves emitted from different sources propagate accidentally in phase creating constructive radiations (antenna-theory.com).

Lately, improvements were introduced to these arrangements. In order to enhance the directivity of the emitted beam, the elements' spacing, excitation weight and firing time are modified. The current investigation seeks a random planar arrangement of point sources, excited successively with uniform time delay. Therefore, the geometry is directly reliant on the time expression. As seen in Chapter 3, the induced time delay equation is also material and field dependent.

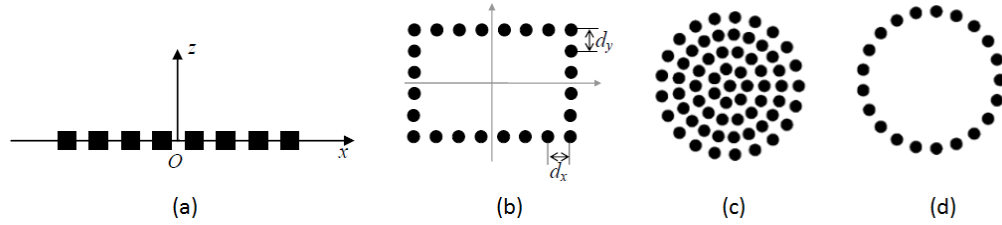


Figure 4.1. Different pattern configuration: (a) linear; (b) rectangular; (c) disk; (d) circular arrays (Lingyu, 2006)

4.1. Actuation Time Delay

Assume Δ the absolute elapsed time between two consecutive excitations. Denote by Δ_m the time delay of the m^{th} actuation. Δ_m can be positive (delayed excitation) or negative (advanced excitation). This classification is determined by the location of the focal point with respect to the time origin and location of defect to be detected. Thus, Δ_m can be written as:

$$\Delta_m = \mp m \Delta ; 0 \leq m \leq M \text{ and } m \text{ is an integer} \quad (4.1)$$

where M is the total number of actuations.

As shown in Figure 4.2 below, in time domain, the origin has a zero-time delay value. On the right side, as the excitation comes closer to the target P , it is delayed (positive delay). The inverse occurs on the left hand side (negative delay). This is due to the fact that for a well-shaped beam, all the wave fronts resulting from the successive excitations should reach point P at the same instant. Assuming constant propagation velocity, an increase in distance leads to an increase in time.

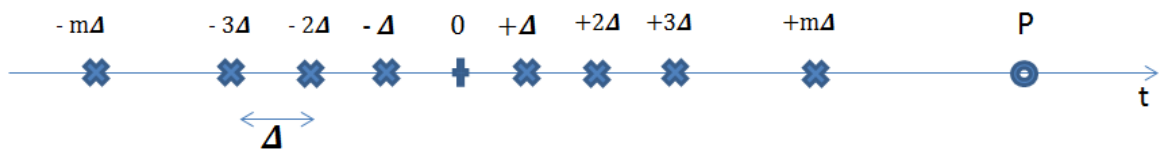


Figure 4.2. Excitations delays in time domain

For the near field, the time delay is expressed in terms of the target position r , the distance from the actuation point to the target denoted r_{m0} and the phase propagation velocity of the front wave.

4.2. Isotropic Propagation Medium

In an isotropic medium, the time delay for a near field target is given by equation (3.47). Equating Equality (3.47) to (4.1) leads:

$$\Delta_m = \frac{r - r_{m0}}{c} = \mp m \Delta ; 0 \leq m \leq M \quad (4.2)$$

Rearranging equation (4.2):

$$r_{m0} = r \mp m \Delta c ; 0 \leq m \leq M \quad (4.3)$$

Equation (4.3) describes a family of equally spaced concentric circles (C_m) of center $P(0, r)$ and radii r_{m0} offset by a distance $d = \Delta c$ where r , Δ , and c are constants.

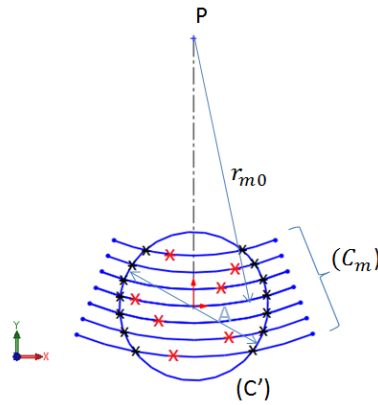


Figure 4.3. Aluminum pattern geometry for a target point in the 90° direction

In addition, all the actuation points must be enclosed within an aperture of diameter D . Let (C') be the circle of center $O(0,0)$ and diameter A . Therefore, the excitations lay on the arcs (C_m) within the circle (C') shown in Figure 4.3.

Note that:

$$r_{m0} = \begin{cases} r - m \Delta c, & y > 0 \\ r + m \Delta c, & y < 0 \end{cases} \quad (4.3)$$

Where y is the ordinate of the excitation point, measured from the circular aperture's center taken as origin.

To determine the spatial distribution of actuations, the allowable range of Cartesian coordinates of each point has to be determined. The equations of $(C')=C[(0,0), \frac{D}{2}]$ and $(C_m)=C[(0,r), r_{m0}]$ are given by:

$$(C'): x_m^2 + y_m^2 = \frac{D^2}{4} \quad (4.4)$$

and

$$(C_m): x_m^2 + (y_m - r)^2 = r_{m0}^2 \quad (4.5)$$

The expression of y_{min} is given by:

$$y_{min} = \begin{cases} m \Delta c, & y > 0 \\ -m \Delta c, & y < 0 \end{cases} \quad (4.6)$$

Whereas y_{max} is determined from intersections of (C') and (C_m) . Equating Equation (4.4) to (4.5) gives:

$$y_{max} = \frac{r^2 - r_{m0}^2 + \frac{D^2}{4}}{2r} \quad (4.7)$$

Proof:

$$(C'): x_m^2 + y_m^2 = \frac{D^2}{4} \rightarrow x_m^2 = \frac{D^2}{4} - y_m^2 : (*)$$

$$(C_m): x_m^2 + (y_m - r)^2 = r_{m0}^2 : (4.5)$$

Replacing (*) in (4.5):

$$\begin{aligned} \frac{D^2}{4} - y_m^2 + (y_m - r)^2 &= r_{m0}^2 \rightarrow \\ -y_m^2 + y_m^2 + r^2 - 2 y_m r &= r_{m0}^2 - \frac{D^2}{4} \rightarrow \\ 2 y_m r &= r^2 - r_{m0}^2 + \frac{D^2}{4} \rightarrow \\ y_m = y_{m,max} &= \frac{r^2 - r_{m0}^2 + \frac{D^2}{4}}{2r} \end{aligned}$$

The range of x_m is expressed by:

$$x_{m,min} = -\sqrt{\frac{D^2}{4} - y_{m,max}^2} \leq x_m \leq \sqrt{\frac{D^2}{4} - y_{m,max}^2} = x_{m,max} \quad (4.8)$$

The boundaries of the m^{th} actuation point are shown in Figure 4.4.

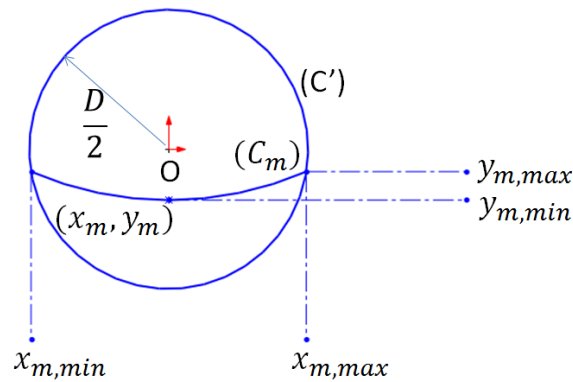


Figure 4.4. The x_m and y_m coordinates range for an isotropic medium

4.3. Anisotropic Propagation Medium

For anisotropy, the same process followed in section 4.2 is applied. However, the time delay equation of an anisotropic medium is given by Equation (3.38). Again equating Equations (3.38) to (4.1) yields:

$$\Delta_m = \frac{r}{c(\theta_0)} - \frac{r_{m0}}{c(\theta_{m0})} = \mp m \Delta ; 0 \leq m \leq M \quad (4.9)$$

Solving for r_{m0} :

$$r_{m0} = c(\theta_{m0}) \left[\frac{r}{c(\theta_0)} \mp m \Delta \right] ; 0 \leq m \leq M \quad (4.10)$$

In this case, the problem is split into two parts, $y_m > 0$ and $y_m < 0$.

- *If $y_m > 0$ ($r_{m0} < r$)*

$$r_{m0} = c(\theta_{m0}) \left[\frac{r}{c(\theta_0)} - m \Delta \right] ; 0 \leq m \leq M \quad (4.11)$$

Assume a unidirectional laminate with 0° fiber angle and a target in the 90° direction:

$$r_{m0} = r_{m0,max} \text{ if } c(\theta_{m0}) = c_{max}(\theta_{m0}) \rightarrow c(\theta_{m0}) = 0^\circ$$

$$r_{m0} = r_{m0,min} \text{ if } c(\theta_{m0}) = c_{min}(\theta_{m0}) \rightarrow c(\theta_{m0}) = 90^\circ$$

Thus,

$$r_{m0,max} = c(0^\circ) \left[\frac{r}{c(\theta_0)} - m \Delta \right] ; 0 \leq m \leq M \quad (4.12)$$

and

$$r_{m0,min} = c(90^\circ) \left[\frac{r}{c(\theta_0)} - m \Delta \right] ; 0 \leq m \leq M \quad (4.13)$$

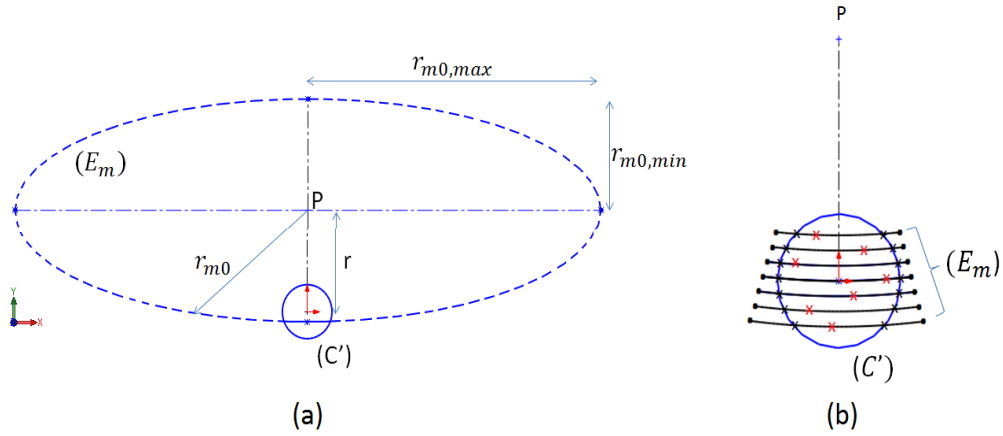


Figure 4.5. Pattern arrangement on elliptical arcs for unidirectional fiber reinforced composites: (a) for a single actuation; (b) for M actuations

The conic of center P and radius r_{m0} is a family of ellipses plotted in Figure 4.5, of Cartesian equation:

$$(E_m): \frac{x_m^2}{r_{m0,max}^2} + \frac{(y_m-r)^2}{r_{m0,min}^2} = 1 \quad (4.14)$$

Recall that the equation of circle (C') is given in Equation (4.4).

$y_{m,min}$ can be determined from the relation:

$$y_{m,min} = r - r_{m0,min} = r - c(90^\circ) \left[\frac{r}{c(\theta_0)} - m \Delta \right]; 0 \leq m \leq M \quad (4.13)$$

$y_{m,max}$ is calculated from the intersection of (E_m) and (C') .

From Equation (4.14),

$$\frac{x_m^2}{r_{m0,max}^2} = 1 - \frac{(y_m-r)^2}{r_{m0,min}^2} \rightarrow x_m^2 = r_{m0,max}^2 \left[1 - \frac{(y_m-r)^2}{r_{m0,min}^2} \right] : (**)$$

From Equation (4.4),

$$x_m^2 + y_m^2 = \frac{D^2}{4} \rightarrow x_m^2 = \frac{D^2}{4} - y_m^2 : (***)$$

Equating (**) to (***) gives:

$$r_{m0,max}^2 \left[1 - \frac{(y_m - r)^2}{r_{m0,min}^2} \right] = \frac{D^2}{4} - y_m^2 \rightarrow$$

$$r_{m0,max}^2 - \left(\frac{r_{m0,max}^2}{r_{m0,min}^2} \right) (y_m - r)^2 = \frac{D^2}{4} - y_m^2 \rightarrow$$

$$r_{m0,max}^2 - \left(\frac{r_{m0,max}^2}{r_{m0,min}^2} \right)^2 (y_m^2 + r^2 - 2 y_m r) = \frac{D^2}{4} - y_m^2 \rightarrow$$

$$r_{m0,max}^2 - \left(\frac{r_{m0,max}^2}{r_{m0,min}^2} \right)^2 (y_m^2 + r^2 - 2 y_m r) - \frac{D^2}{4} + y_m^2 = 0 \rightarrow$$

$$\left[1 - \left(\frac{r_{m0,max}^2}{r_{m0,min}^2} \right)^2 \right] y_m^2 + \left[2 r \left(\frac{r_{m0,max}^2}{r_{m0,min}^2} \right)^2 \right] y_m + \left[r_{m0,max}^2 - \frac{D^2}{4} - r^2 \left(\frac{r_{m0,max}^2}{r_{m0,min}^2} \right)^2 \right] = 0 \quad (4.14)$$

Parity (4.14) is a quadratic equation of variable y_m and can be written in general form:

$$A y_m^2 + B y_m + C = 0 \quad (4.15)$$

Where A, B and C are given by:

$$A = 1 - \left(\frac{r_{m0,max}^2}{r_{m0,min}^2} \right)^2$$

$$B = 2 r \left(\frac{r_{m0,max}^2}{r_{m0,min}^2} \right)^2$$

$$C = r_{m0,max}^2 - \frac{D^2}{4} - r^2 \left(\frac{r_{m0,max}^2}{r_{m0,min}^2} \right)^2$$

The system is solved in MATLAB by the following algorithm:

```
>>P = [A B C];
>>R=roots (P);
>>Y_m_max = min (R);
```

- If $y_m < 0$ ($r_{m0} > r$)

$$r_{m0} = c(\theta_{m0}) \left[\frac{r}{c(\theta_0)} + m \Delta \right]; 0 \leq m \leq M \quad (4.16)$$

Again,

$$r_{m0} = r_{m0,max} \text{ if } c(\theta_{m0}) = c_{max}(\theta_{m0}) \rightarrow c(\theta_{m0}) = 0^\circ$$

$$r_{m0} = r_{m0,min} \text{ if } c(\theta_{m0}) = c_{min}(\theta_{m0}) \rightarrow c(\theta_{m0}) = 90^\circ$$

Therefore,

$$r_{m0,max} = c(0^\circ) \left[\frac{r}{c(\theta_0)} + m \Delta \right]; 0 \leq m \leq M \quad (4.17)$$

and

$$r_{m0,min} = c(90^\circ) \left[\frac{r}{c(\theta_0)} + m \Delta \right]; 0 \leq m \leq M \quad (4.18)$$

also

$$y_{m,min} = r - r_{m0,min} = r - c(90^\circ) \left[\frac{r}{c(\theta_0)} + m \Delta \right]; 0 \leq m \leq M \quad (4.19)$$

$y_{m,max}$ is calculated as before by solving Equation (4.15) but $r_{m0,max}$ and $r_{m0,min}$ are used from Equations (4.17) and (4.18) respectively.

5. Finite Element Model and Results

Finite Element Analysis (FEA) is a powerful computerized tool to simulate the actual conduct of a mock-up under subjected loads, boundary conditions and/or environmental circumstances. In the last decades, FEA is intensely manipulated in engineering projects as it allows the prediction of the mechanical properties of a product. The compensation of time, the reduction of costs and the great level of accuracy of the results encourage the designers to rely on this technique at the conceptual, preliminary and detailed stages of design and construction. Additional experiments on real samples are also highly recommended to validate the virtual findings.

In the current study, a finite element model is made using ABAQUS/CAE 6.14 finite element (FE) software to monitor the wave propagation contour in a thin circular plate. Because the dispersion profile is symmetric in the four quadrants, a quarter portion is only modelled. An explicit dynamics analysis is performed on both Aluminum and unidirectional Hankuk Carbon CU 150NS composite specimens. For both models, the plate is excited at a single node at the center and a set of sensing nodes are selected to extract the wave properties. The boundary conditions are symmetrical and the simulation time is chosen so that no reflections from edges are detected by the sensors. The plots of out-of-plane displacements in various directions are obtained from an explicit dynamics analysis. Then, displacement amplitude and phase velocity are calculated, plotted and implemented later in the optimization algorithm.

5.1. Plate Modelling

In ABAQUS, the plate modelling consists of five basic steps. These are:

- Part creation
- Material selection and section assignment
- Step formation
- Loads and boundary conditions attribution
- Mesh instance creation
- Field and output request generation
- Job creation and verification

5.1.1. Part creation

The three dimensional (3D) deformable part consists of a quarter disk of radius 150mm and 1.125 mm thickness. The part is modelled as a solid instead of shell to provide a normal to plane propagating medium for the wave. For meshing purposes, an arc of radius 50mm was drawn on the top surface of the plate, then, partitioned through the thickness, as shown below in Figure 5.1.

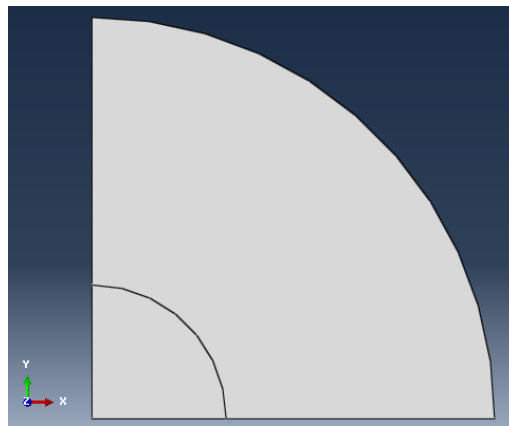


Figure 5.1. A top view of the quarter plate (ABAQUS/CAE 6.14)

5.1.2. Material selection and section assignment

Two separate simulations are established for aluminum and composite so that the isotropic and the anisotropic behaviors are compared. The Young's modulus (E), the shear modulus (G), the Poisson ratio (ν) and the density (ρ) are inputted into the software. The mechanical properties of both materials are shown in Table 5.1.

Note that both models were assigned homogeneous solid sections. Disregarding the occurrences at every layer, the unidirectional composite laminate is seen as a stack having mechanical properties that are direction reliant.

Table 5.1. Mechanical properties of the aluminum and composite

Mechanical Properties	Aluminum	Composite
E_1 (GPa)	68.9	125
E_2 (GPa)	68.9	8.1
E_3 (GPa)	68.9	8.1
G_{12} (GPa)	25.9	4.2
G_{13} (GPa)	25.9	4.2
G_{23} (GPa)	25.9	3.5
ν_{12}	0.33	0.33
ν_{13}	0.33	0.33
ν_{23}	0.33	0.45
ρ (Kg / m ³)	2700	1550

5.1.3. Step formation

The simulation time step is chosen so that the excitation signal can be detected at the sensors before the waves are dispersed and reflected back from the boundaries. Because the wave speed depends on the propagation medium, aluminum and composites analyses are run for 0.135×10^{-3} s (seconds) and 0.145×10^{-3} s respectively. An identical time increment of 5×10^{-7} s is chosen to identify precisely the wave propagation profile. Such increment respects a certain criteria stated by Osterc (2015); the period of a travelling signal is the inverse of the frequency and 20 increments are required at least per oscillation period to ensure accuracy and stability requirements in ABAQUS.

5.1.4. Loads and Boundary Conditions Attribution

The mode shape of vibrations is influenced by the direction of the subjected load. Also, depending on the excitation manner, the upper and lower surfaces oscillate harmonically either in a symmetrical or anti-symmetrical mode. In order to isolate the symmetric mode, loads in the same direction are applied on the top and bottom surfaces of the body. However, a pure antisymmetric mode can be obtained by exerting opposing loads on these surfaces. In this case study, a concentrated unit (1N) force, with a 2.5-cycle-Hanning window sinusoidal signal of 50 KHz plotted in Figure 5.2, is applied orthogonally on the upper plane of the plate to monitor the entire wave packet.

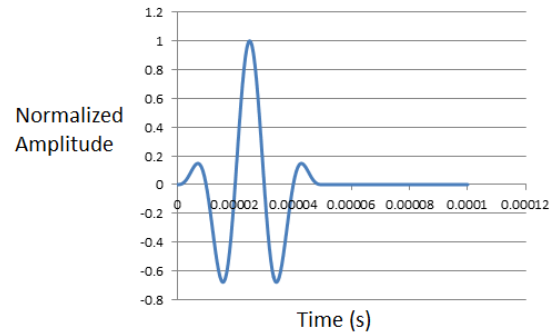


Figure 5.2. 50 KHz 2.5 Hanning window for 0.1 ms excitation interval

A model obeys to symmetry condition if its geometry, material, load and boundary conditions are all symmetric about a certain plane in the three dimensional space. Symmetric boundaries constrain all the translations perpendicular to the plane of symmetry and the rotational degrees of freedom that generate out of plane motion. A portion of the geometry with increment load is studied and the results are generalized for the remaining part. The load and boundary condition of the plate are shown in Figure 5.3.

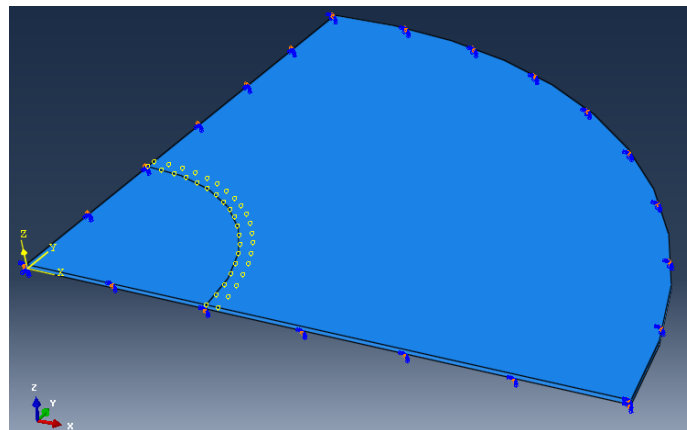


Figure 5.3. Normal load and boundary conditions imposed to the thin plate (ABAQUS/CAE 6.14)

5.1.5. Mesh Instance Creation

The meshing is very important in the numerical simulation. It is commonly known that a fine mesh usually gives high accuracy calculation results. However, up to a

certain limit, the mesh refinement will not have a great effect on the results. Therefore, an optimized mesh element is reasonable for accurate outcomes and reduced time consumption.

The element aspect ratio (AR) should be also taken into consideration. Generally, for a solid stress analysis, the aspect ratio of a cubic cell should not exceed 15. In ABAQUS, a high aspect ratio (about 100) will cause simulation crash and a warning will pop up on the screen.

After setting the loads and boundaries, the subparts of the model are meshed separately. For the enclosed quarter piece, the orthogonal edges are seeded a biased partition starting from 0.2mm at the center and expanding to 0.5mm at the vicinity of the circular border. A sweep, hexagonal-dominant (element shape) and advancing front mesh is selected.

The advancing front procedure creates quadrilateral elements all around the seeded boundaries of the section, respecting precisely the seeding dimensions, and continues the generation of the same elements as it moves towards the inside of the region.

Second, the in-plane boundaries of the outer plate are uniformly portioned; each section is 0.05mm long. The outer portion is meshed with a sweep, hexagonal-dominant (element shape) and medial method. In addition, two elements across the thickness are enough for the entire model.

The medial axis algorithm operates differently than the advancing front algorithm. It first sections the region to be meshed into simpler divisions. Then, these partitions are filled in by small cells.

5.1.6. Field and Output Request Generation

Finite element analyses generate huge data of outputs. However, through ABAQUS, these information can be managed so that only required data are produced. In the field output request manager, the database extracted at every iteration from the entire model is chosen. This enables the animation of displacements and velocities profiles.

Specific nodes' data can be designated from the history output request manager. Because the aim of the ABAQUS simulation is to extract the out-of-plane amplitude and phase velocity in all the directions, precise sensor nodes marked by yellow dots in Figure 5.4 are picked. The array of nodes is selected at 50mm from the center, spaced by a 5° increment angle and offset by 3mm.

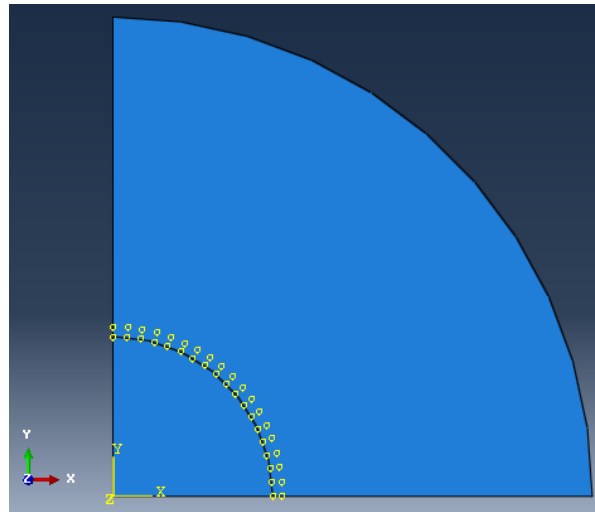


Figure 5.4. Sensors distribution on the 150 mm radius quarter plate (ABAQUS/CAE 6.14)

5.1.7. Job Creation and Verification

The job creation and confirmation is the last step before running the simulation. At this stage, the model is verified for any error or warning in the inputs. For any detected error, the term “aborted” is shown in the command window. Otherwise, the analysis is “complete” and the output data starts storing in the database. The progress

status of the job can be also seen. An explicit dynamics analysis is run once neither warnings nor modelling errors were detected.

5.2. Postprocessing, Results and Plots

Once the simulation terminates, the pool of data is gathered and ready to be interpreted. For a non-defected plate, it is expected that the profile of the emitted signal from the source, located at the origin, does not change drastically at any location. In other words, the perturbations should preserve the same number of cycles (2.5 cycles). This statement is validated by Figure 5.5 for both the anisotropic and isotropic media.

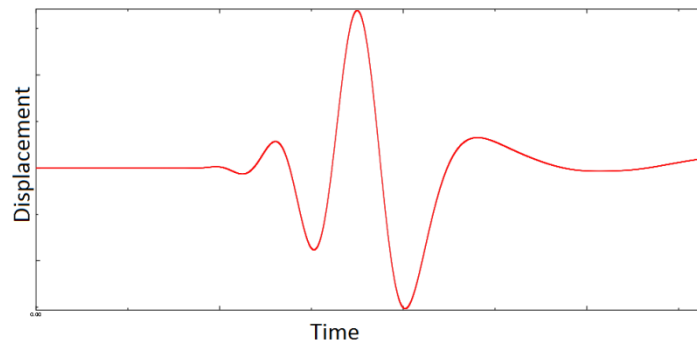


Figure 5.5. Signal response detected by a sensor 50mm from the excitation source (ABAQUS/CAE 6.14)

As mentioned in the previous chapters, due to the anisotropic nature of the composites, the material is direction dependent. Therefore, waves tend to propagate along the fibers more rapidly and at higher amplitude compared to the other directions. This is not the case for aluminum. For a single excited point, in an isotropic medium, the disturbances spread in circular rings. A comparison is made in Figure 5.6.

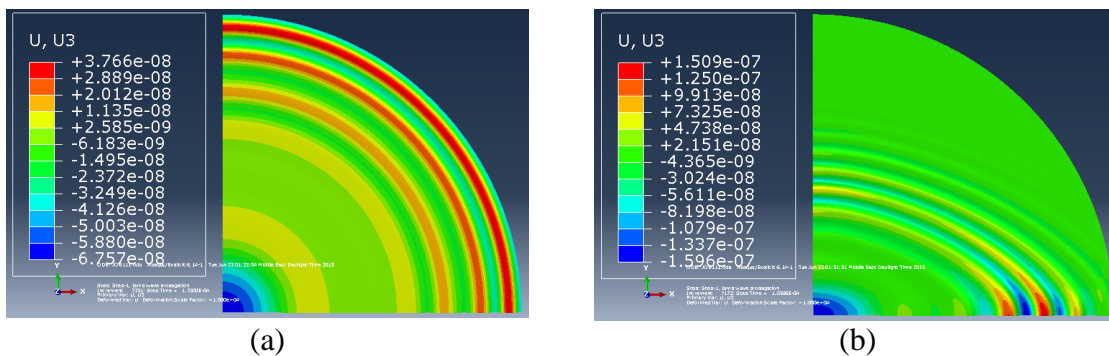


Figure 5.6. Out-of-plane displacement amplitude; (a) for aluminum; (b) for composite for 0° fiber angle (ABAQUS/CAE 6.14)

The phase velocity, amplitude and slowness curves cannot be obtained directly from the finite element software. Excel sheets are established to store the tables of coordinates, then, the plots are drawn, as shown in Figures 5.7 and 5.8, using MATLAB.

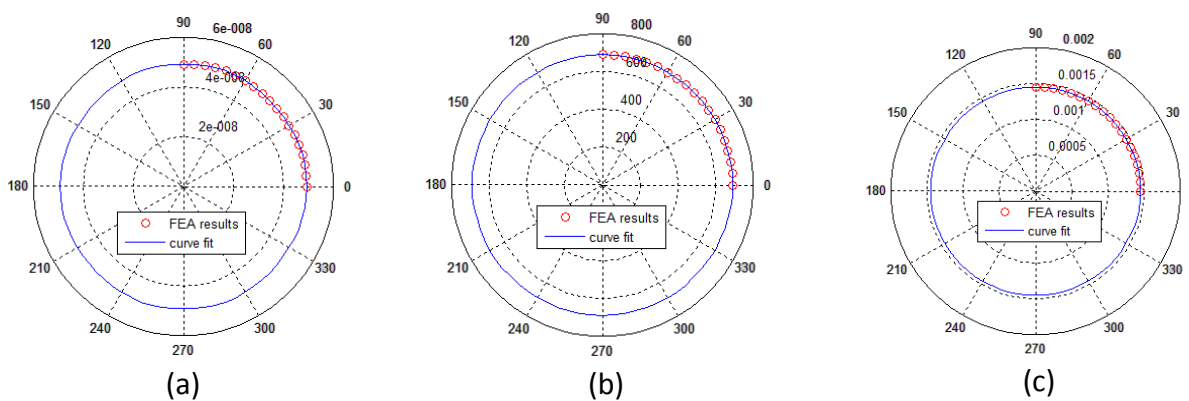


Figure 5.7. Characteristics of a 50 KHz lamb wave propagation in an aluminum plate of thickness 1.125mm: (a) amplitude profile; (b) phase velocity; (c) slowness curve

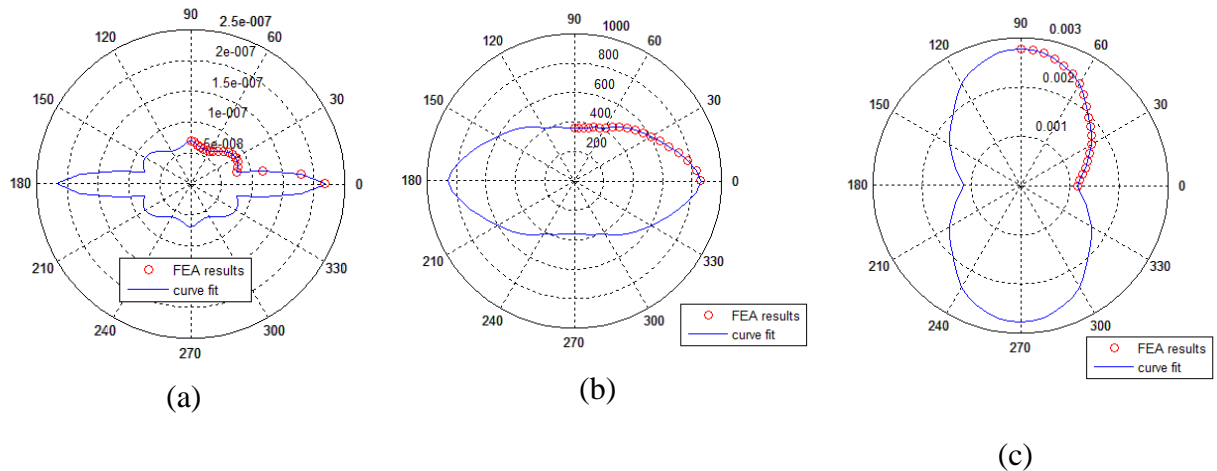


Figure 5.8. Characteristics of a 50 KHz lamb wave propagation in a unidirectional 0° composite plate of thickness 1.125mm: (a) amplitude profile; (b) phase velocity; (c) slowness curve

5.3. Results Confirmation

In order to validate the results, the findings of the anisotropic simulation are compared to data found in previous works.

Salas and Cesnik (2010) plotted the phase velocity and amplitude profiles of a 12-layer unidirectional laminate from data offered by the finite element analysis and laser vibrometry. The polar plots are given in Figure 5.8. The overall FEM polar plots of Figure 5.9 are similar to those in Figure 5.8 (a) and (b). For the antisymmetric mode, the phase velocity profile resembles to an ellipse of horizontal major axis. The amplitude plot in both cases is also similar; the curve has three local maxima between 0 and 90° .

Pant (2014) also schemed the slowness curves of unidirectional laminate at various frequency-thickness products by isolating the anti-symmetric mode of guided lamb wave. In both figures 5.8 (c) and 5.10, the slowness curves have a minimum at 0° and a maximum at 90° .

For the phase velocity, slowness and amplitude curves, the slight variation of the

shape is due to the evident dissimilarity of the excitation signal's amplitude, laminate thickness, composite mechanical properties and meshing method. For instance, Salas and Cesnik (2010) used a 12-ply laminate at 75 KHz frequency, 3.5 Hanning window signal. The specimen is meshed with C3D8 and C3D6 0.25 mm element. The mechanical properties of the stack are also different than those used in Table 5.1.

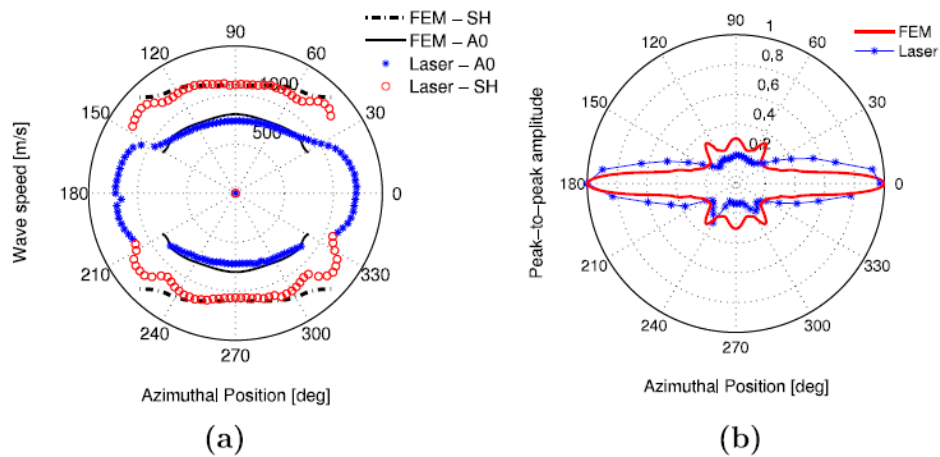


Figure 5.9. Wave characteristics of 12-layer unidirectional laminate: (a) phase velocity; (b) peak-to-peak amplitude profiles (Salas and Cesnik, 2010)

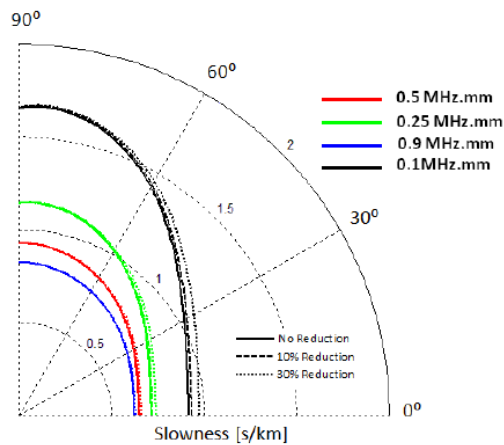


Figure 5.10. Slowness curves at different frequency-thickness product of antisymmetric Lamb wave dispersing in unidirectional laminate (Pant, 2014)

6. Optimization Algorithm

Optimization allows the best end result to be selected among alternative plausible solutions. The main limitations when maximizing the efficiency of a combination of parameters are the cost function and the boundary conditions. Optimization is useful in different research fields dealing with applied mathematics. In phased arrays searches, space optimization of the actuation points leads to a well-shaped beam with low Side-Lobes Levels (SLL) and narrow Beam-Width First Null (BWFN). It also provides enhanced beamforming with reduced actuation points for steering toward a desired location.

Particularly for randomly distributed excitation points, the arrangements of positions are infinitely numerous; any alteration of one point contributes to a modified re-organization of the remaining set. Therefore, the problem can be treated by initializing a random permutation of conceivable solutions. Then, the suggested coordinates are evaluated based on the hypothetical restrictions by means of an optimizing method and the best space combination is finally chosen.

6.1 Proposed Algorithms for Phased Arrays

A variety of optimization practices concerning geometrical distribution of actuators are discussed in previous published works. In major reviews, the Genetic Algorithm (GA) in parallel with the Particle Swarm Optimization (PSO) is widely employed beside other evolutionary techniques to treat linear and multi-dimensional patterns.

6.1.1 Linear Arrays

Uniformly spread linear arrays generate a high grating lobe in a different direction

than that of the steered main beam but with approximately equal amplitude. This occurrence is undesirable since it clues to confusion about the location of the defect to be precisely determined. Optimization methods play on eliminating the periodicity of excitation by producing sparse arrays. For treating linear arrays, Merad *et al.* (2006) emphasize the use of Controlled Random Search (CRS) Optimization procedure. They also encourage for further development of these techniques for upcoming use. Kaur and Kumar (2011) suggested five evolutionary optimization approaches to alter the uniform spacing between the actuators so that better beam scanning is achieved. But, only one technique is highly recommended among the others. The selection falls on Biogeography Based Optimization (BBO) in first place in comparison with Genetic Algorithm, Simulated Annealing (SA), Bacteria Foraging (BFA) as well as Particle Swarm Optimization. PSO also has advantages above its candidates. In terms of optimal findings at a low computation period and simple cost function, PSO leads over the rest. PSO also tolerates beam steering inaccuracies better than BFA (Kaur & Kumar, 2011) whereas the latter has a greater role in side lobe suppression (Datta & Misra, 2008). Later, Ridwan *et al.* (2012) designed a non-uniform linear antenna array using Genetic Algorithm. To demonstrate the effectiveness of their algorithm, the final results are compared to the uniform, the binomial and Dolph-Chebyshev arrays. The improvements came on the level of beam directivity, beamwidth and sidelobes' amplitudes. For all the arrays, the array factor is normalized to compare the sidelobes' levels for various numbers of actuators. The GA was able to produce lower sidelobes than the binomial and Dolph-Chebyshev arrays. However, it should be noted that the element spacing to wavelength ratio (d/λ) for a non-uniform array is smaller (approximately 0.15) compared to a uniformly arranged

pattern (about 0.5) (Ridwan *et al.*, 2012). Again, Shreni and Raikwar (2012) confirm the ability of the Genetic Algorithm to reduce the sidelobe amplitudes for 8, 20 and 24 elements. In the same domain of research, Bhattacharya *et al.* (2012) proposed a family of developed models of the traditional Particle Swarm Optimization Technique. Position Mutated Hierarchical Particle Swarm Optimization algorithms with Time Varying Acceleration Coefficients, denoted HPSO-TVAC, are employed to adjust the main beam properties (SLL and BWFN). For HPSO-TVAC, the velocity and displacement equations are modified to ameliorate the convergence to the mean global best value (Bhattacharya *et al.*, 2012).

6.1.2 Circular Arrays

Wave-emitting sources can be arranged in a circular rather than linear manner. For such arrays, the problem does not only deal with beamwidth and sidelobe level, but extends to minimize the aperture size of the arrangement. Due to its geometry, a circular configuration has the tendency to generate comparable wave beams in all directions when all excitations are fired at the same time. Thus, the greatly elevated grating lobes appear as main beams. A non-uniform rearrangement with firing time adjustment of the actuation elements improves beam steering. Real Genetic Algorithm (RGA) and Hierarchical Dynamic Local Neighborhood based PSO (HDLPSO) procedures are adequate optimization tactics for this situation. Bhattacharya *et al.* (2012) used the Real Genetic Algorithm method to reallocate evenly dispersed actuators on the circumference of a circle. Their study proposes minimizing a cost function relating the nulls levels to sidelobes' amplitudes and the main lobe beamwidth. Ghosh *et al.* (2012) recommended a diverse concept, founded on HDLPSO, to deal with circular arrays. After comparison of

radiation patterns, it can be noticed that the main beam width is the same at a normalized amplitude, but HDLPSO overcomes the conventional PSO and GA by clamping down the sidelobes. The circumference, in terms of wave length, is evaluated and reflects a great similarity between both methods for an increased number of elements (Ghosh *et al.*, 2012). A similar process was applied by Mandal *et al.* (2009) for an equally distributed array. Intensity factor findings from Binary coded Genetic Algorithm (BGA), Particle Swarm Optimization with Constriction Factor and Inertia Weight Approach (PSOCFIWA) and Crazyiness-based Particle Swarm Optimization (CRPSO) are compared for uniformly and non-uniformly excited cases (Mandal D. *et al.*, 2009).

6.1.3 Multi-Dimensional Arrays

Despite the wide investigation of uniform planar arrays, the multi-dimensional random arrangement of actuation points is barely examined. Most studies focus on varying the number of actuators, adjusting the weighting factor or marginally shifting the positions of elements in symmetric patterns. Bevelacqua (2008) advocates a linear programming method applicable for both linear and planar arrays to suppress the sidelobes' levels. In his method, the weighting factors are fluctuated between the exciters for the known geometry. In an analogous way, given a hexagonal pattern of wave emitters, Chen *et al.* (2005) deduced the excitation amplitude and phase of each unit to produce a well-oriented, three-dimensional wave front through PSO. Admitting the influence of the geometry on the sidelobes' levels, Bevelacqua (2008) also processed an optimization for estimating the locations of symmetrically-dispersed actuators using PSO for spatial coordinates determination. However, the reported elapsed time of the simulation versus the number of actuators is enormous. For instance, locating four

actuators consumes three hours which goes up to ten hours for only positioning seven elements. For two-dimensional, spatially arranged actuating points, a good beamforming is sometimes obtained for a higher number of elements. From a different point of view, “A Pareto Elite Selection Genetic Algorithm (PESGA) for Random Antenna Array Beamforming with Low Sidelobe Level” was lately completed by Jayaprakasam *et al.* (2013). Assuming there is a fixed distribution of elements, PESGA is proven to be more effective than other scenarios to decide the weights with the coordinates of all the elements previously known. During the simulation, the peak sidelobe level versus the flow of generations is monitored until convergence is attained. To validate the method, the evolutionary technique is placed face to face with the conventional GA (Jayaprakasam *et al.*, 2013).

6.2 Algorithm Selection

Because the proposed hypothesis in this investigation is uncommon, it is impossible to exactly apply any of the methods exhibited in the previous section. Recall that the major assumption is to preserve the same excitation delay at an undeviating weighting factor while optimizing the pattern. Accordingly, the expected geometry relies upon these assumptions as well as the wave front speed and out-of-plane displacement within the material. Once the inputs and the parameters to be adjusted are already determined, the optimization method can be selected. Based on the reviews of planar arrays, it is evident that the choice is restricted between GA and PSO to compute the Cartesian coordinates of every actuation point.

6.2.1 Genetic Algorithm

The genetic algorithm optimization technique intends to mimic the phenomenon

of reproduction of creatures in nature. In fact, a cell of any living organism encloses a nucleus of genes and group of genes constitutes the chromosomes. These chromosomes can be compared to a memory card that stores all the information of the body. The genes define certain features such as color of hair, skin and eyes, and the height, etc. Every organism can be identified by its unique combination of genes. During mating of the parent chromosomes, the sets of each partner try to dominate over the others. Strong genes are the ones that remain for the upcoming offspring. Likewise, the genetic algorithm is manipulated to solve the mathematical hypothesis by treating a series of promising solution candidates considered as the chromosomes, and each variable of the solution vector is a gene.

The GA is a suitable utensil to find near feasible local minima or maxima for a non-linear system where it is difficult to get to the global optimum resolution in a reduced computational time. Unlike gradient methods, depending on the initial guess, the genetic algorithm always converges to a sequence of variables that optimizes the fitness of the whole population (Carr, 2014 & Herrera, 1998).

6.2.2 Particle Swarm Optimization

The concept of PSO is inspired from the social behavior and movement of flocking insects, birds and fish. The collection of particles is called population and the final result is the convergence of all the members of the group. The fundamental of PSO involves the social force theory; pedestrian dynamics interpret a model of moving members considered as point mass particles. The principle accounts for social interaction and relates the behavioral change of an individual to its surroundings. For instance, a member usually has a tendency to reach the desired destination smoothly or involvement

with its neighbor environment. However, the adjacent individuals provoke repulsive, as well as interactive, forces. Social forces are present to adapt the individuals' motion to the overall flow.

Every individual has a personal tendency to select the path to follow and its corresponding velocity, although the overall flow obliges him/her to adjust to a collective strategy. Thus, there are two best, global and personal position and velocity (Kennedy, 1995 & Clerc, 2012).

6.2.3 Interpretation and Selection

Most optimization techniques have the same following global structure:

- A random starting population is generated including promising key solutions for the stated matter.
- Boundary and/or initial conditions are evaluated, if existing.
- Objective (cost) and fitness functions are verified for each guess.
- The population is reproduced with certain adjustments.
- The process is repeated through many generations, enabling convergence of the best guess to the desired end result.

GA and PSO respect the overall scheme, but modifications occur at the level of population reproduction. The GA is comprised of two main reforms that are not available in PSO: mutation and cross-over. Cross over allows mating of the genes of two parents to produce offspring. Mutation occurs by breeding some chromosomes with new values. The GA place high expectations on these steps, depicted in Figures 6.1 and 6.2, as they probably bring improvements to the final solution and introduce alterations to the initially suggested pool of results that are chosen randomly.

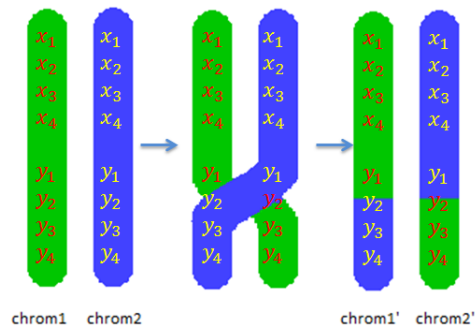


Figure 6.1. Chromosome single point cross-over

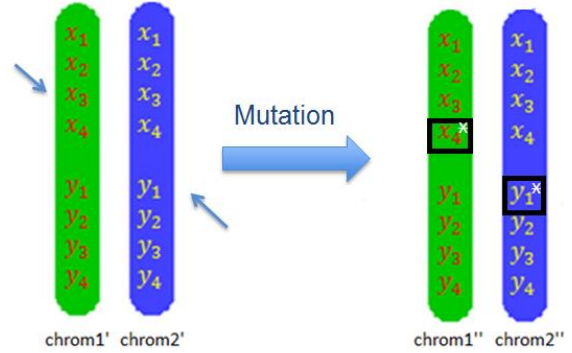


Figure 6.2. Chromosome mutations

On the other hand, the PSO calibrates the particles' motion and position, based on their personal states and the overall situation. Therefore, every single member of the population converges at the end toward the optimum result. PSO initiates with a primary presumption of a swarm of random particles; it is reported that 10 to 15 possibilities are usually sufficient (Clerc, 2012). The initial velocity and location are computed from Equations (6.1) and (6.2) respectively. Then, the given objective function is evaluated successively for all individuals. At each iteration, the velocities and positions are respectively updated from Equations (6.3) and (6.4). The best element coordinates with the lowest cost function value are extracted and updated every time.

$$x_0^i = x_{min} + rand1 (x_{max} - x_{min}) \quad (6.1)$$

$$v_0^i = \frac{x_{min} + rand1 (x_{max} - x_{min})}{\Delta t} \quad (6.2)$$

$$x_{k+1}^i = x_k^i + v_{k+1}^i \Delta t \quad (6.3)$$

$$v_{k+1}^i = w v_k^i + c_1 rand2 \frac{(p^i - x_k^i)}{\Delta t} + c_2 rand3 \frac{(p_k^g - x_k^i)}{\Delta t} \quad (6.4)$$

By introducing the constriction factor, Equation (6.4) can be written as:

$$v_{k+1}^i = k [v_k^i + c_1 rand2 \frac{(p^i - x_k^i)}{\Delta t} + c_2 rand3 \frac{(p_k^g - x_k^i)}{\Delta t}] \quad (6.5)$$

where:

w : inertia weight

k : constriction factor

x_0^i is the initial position of the i^{th} particle

x_{min} is the minimum allowable displacement from the origin of the coordinate system

x_{max} is the maximum allowable displacement from the origin of the coordinate system

v_0^i is the initial velocity of the i^{th} particle

v_{k+1}^i is the velocity of particle i at time $k+1$

w is the inertia factor range (between 0.4 and 1.4)

v_k^i is the velocity of particle i at time k

c_1 is the self confidence range (between 1.5 and 2)

c_2 is the swarm confidence range (between 2 and 2.5)

p^i is the i^{th} particle's best position

x_k^i is the position of particle i at time k

x_{k+1}^i is the position of particle i at time $k+1$

p_k^g is the global best position

Δt is the time interval per iteration

wv_k^i is the current motion

$rand \frac{(p^i - x_k^i)}{\Delta t}$ is the particle memory influence

$rand \frac{(p_k^g - x_k^i)}{\Delta t}$ is the swarm influence

Equations (6.1) to (6.4) are listed in Hassan *et al.* (2004) and the position and velocity vectors are depicted in Figure 6.3 below.

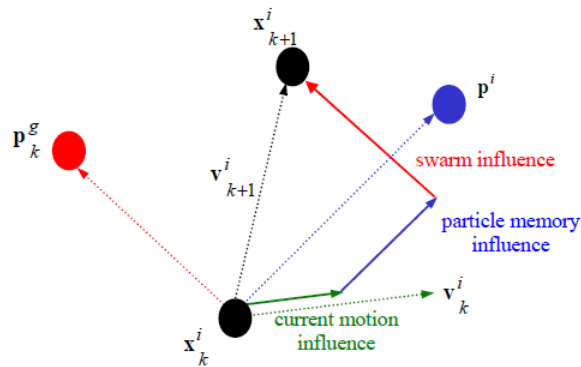


Figure 6.3. The i^{th} particle's local and global best displacement and velocity vectors (Hassan *et al.*, 2004)

In the current situation, GA works better than PSO for the following reasons:

First, the variables to be optimized are constraints within definite intervals that are determined by the aperture of the whole array pattern. In PSO, the new particle's position is updated based on the migration speed, as shown in Equation (6.3). The developed Particle Swarm Optimization techniques for the variables' constrained spaces rely on adjusting some parameters within the same velocity equation. Mezura-Montes and Flores-Mendoza (2011) propose to adjust the velocity function through the inertia weight (w), constriction factor (k) or the social network structures (c_1 and c_2). Helwig *et al.* (2009) implement a velocity adaptation mechanism into the conventional PSO algorithm. However, some new possibilities still will not verify the imposed boundary conditions and will be excluded. Therefore, the effective swarm size will be reduced. From the other side, in the GA, the cross-over and mutation allows regeneration of new solution candidates that automatically respect the limited range of every variable.

Second, PSO algorithm allows only convergence of the swarm to the optimum

result. In this process, the final result will be dependent on the initial guess, whereas, through mutation and cross-over, additional possibilities can be implemented and tested at every iteration.

Third, in the current situation, due to the wide probabilistic range of guess and technical restrictions, it is impossible to determine a global optimum. If manipulating a PSO technique especially at a high order of actuation points and a large population, the convergence of all the possibilities will consume excessive time.

As a result, a recommended GA method, revealed in the section below, will be initiated to formulate an optimized spatially perturbed array.

6.3 The Process of Optimization for The GA

The aim of this section is to define a tailored, appropriate methodology, which describes the suggested hypothesis and accommodates the theoretical requirements of the problem exhibited in Chapter 4. In this case study, the pattern of the actuation points is investigated. These points are located on arcs within a predefined aperture and spaced in such a way that the excitation time delay is kept constant. In addition, it is important to preserve the centroid location at the origin of the coordinate system. The formed beam should also be able to effectively scan a defect situated either in the near or far field from the array. Thus, the plan, thus, proposes the generation of a set of y-ordinates of these excitation points from which the x- values are determined. Then, the obtained coordinates are evaluated upon the stated constraints. The process is iterated many times until the ultimate pattern is reached. The strategic steps of the current problem in Cartesian coordinates are stated in Figure 6.4 below. It is possible to use polar coordinates r and θ instead of x and y , respectively. The algorithm starts by initiating a value of r and θ

instead of y and x.

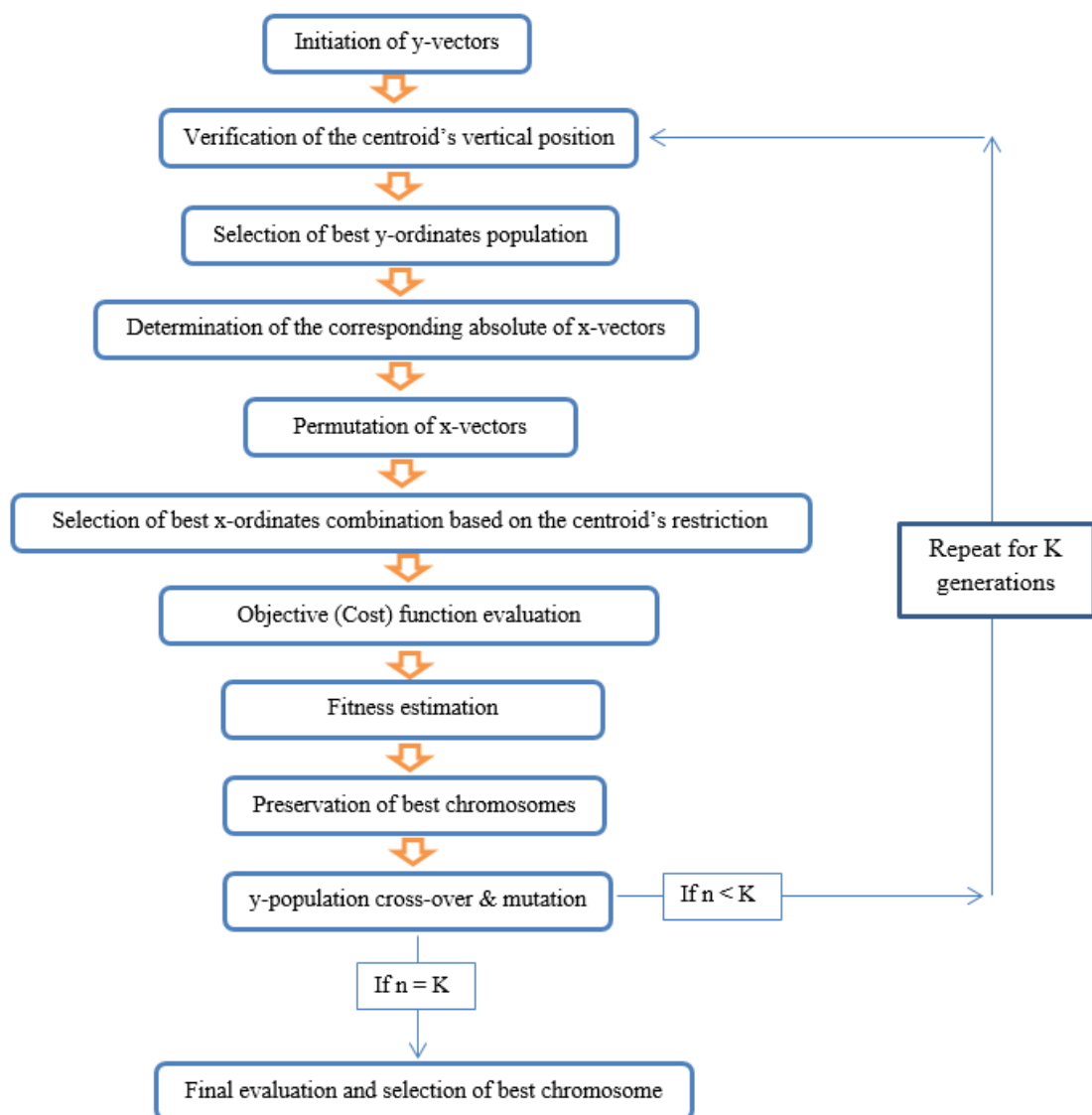


Figure 6.4. The flow chart of the proposed Genetic Algorithm for multi-directional sparse array

Part I: y-ordinate determination

- 1- Initiate, for a first guess, a matrix E of dimensions $M \times N$ where M represents the number of desired actuations and N that of the possible combinations of y-locations. Each vector of the matrix represents a promising resolution to the problem.

$$E = \begin{bmatrix} y_{1,1} & \cdots & y_{1,N} \\ \vdots & \ddots & \vdots \\ y_{M,1} & \cdots & y_{M,N} \end{bmatrix} \quad (6.6)$$

where

$$y_{i,j} = y_{i,j \min} + r_{i,j} \cdot \text{cof} \cdot (y_{i,j \max} - y_{i,j \min}) \quad (6.7)$$

$r_{i,j}$ is a decimal number between 0 and 1

$$0 < r_{i,j} < 1 \quad (6.8)$$

cof is a decimal correction factor which controls the position of the y-values from the y-axis.

$$0 < cf < 1 \quad (6.9)$$

- 2- The centroid is calculated from the relation:

$$\bar{y} = \frac{1}{M} \sum_{i=1}^M y_i \quad (6.10)$$

The centroid should be at the origin of the coordinate system. However, no combination can place it exactly at zero. For this reason, an allowable tolerance, ε , is proposed in such a way that the final result is not seriously affected. Equation (6.10) becomes:

$$|\bar{y}| = \varepsilon \quad (6.11)$$

- 3- At this stage, it's important to verify the condition (6.11) for every vector of matrix E.

If not satisfied, the vector is excluded out of matrix E and matrix E reduces to:

$$G = \begin{bmatrix} y_{1,1} & \cdots & y_{1,R} \\ \vdots & \ddots & \vdots \\ y_{M,1} & \cdots & y_{M,R} \end{bmatrix}; R < N \quad (6.12)$$

Where R is the number of vectors verifying equation (6.11)

Part II: x-ordinate determination

- 4- The absolute values of $x_{i,j}$ can be found from chapter 4. However, each element $y_{i,j}$ of vector y relates to a negative and a positive value of x , thus:

$$x_{i,j} = S_{i,j} \cdot |x_{i,j}|; 1 < i < M; 1 < j < R \quad (6.13)$$

where

$$S_{i,j} = \{-1,1\} \quad (6.14)$$

Note that, for polar coordinates, every value of r corresponds to either a positive or negative angle. The angle is measured from the vertical y -axis.

The value of $S_{i,j}$ is selected randomly and the absolute two-dimensional x -matrix becomes:

$$H = \begin{bmatrix} |x_{1,1}| & \cdots & |x_{1,R}| \\ \vdots & \ddots & \vdots \\ |x_{M,1}| & \cdots & |x_{M,R}| \end{bmatrix} \quad (6.15)$$

Now, for every single vector $|x|$ from matrix H corresponds Z combinations of positive and negative terms. Accordingly, the situation urges for a three-dimensional matrix for x -coordinates enclosing rows, columns and layers. The rows represent the x -abscissa of the actuation points, the columns are different combinations of x values and the layers enclose the attributed x -matrice to each vector of matrix H.

- 5- Again, similar to y-ordinates, the x-matrices is generated in two stages. First, a matrix labeled L_k is created by selecting randomly the $S_{i,j}$ values for a certain range of $x_{i,j}$.

The matrix L_k is written as:

$$L_k = \begin{bmatrix} x_{1,k,1} & \cdots & x_{1,k,Z} \\ \vdots & \ddots & \vdots \\ x_{M,k,1} & \cdots & x_{M,k,Z} \end{bmatrix}_{\text{layer } k} ; 1 < k < R \quad (6.16)$$

- 6- In the same way as y, every vector of L_k is evaluated based on the equation:

$$\bar{x} = \frac{1}{M} \sum_{i=1}^M x_i \quad (6.17)$$

Then, the x-vector, having the minimum \bar{x} , is taken and attributed to its corresponding y-vector in the initial population.

$$J = \begin{bmatrix} x_{1,1} & \cdots & x_{1,R} \\ \vdots & \ddots & \vdots \\ x_{M,1} & \cdots & x_{M,R} \end{bmatrix} \quad (6.18)$$

- 7- Finally, the initial population, P, is given by:

$$P = \begin{bmatrix} E \\ J \end{bmatrix} = \begin{bmatrix} x_{1,1} & \cdots & x_{1,R} \\ \vdots & \ddots & \vdots \\ x_{M,1} & \cdots & x_{M,R} \\ y_{1,1} & \cdots & y_{1,R} \\ \vdots & \ddots & \vdots \\ y_{M,1} & \cdots & y_{M,R} \end{bmatrix} \quad (6.19)$$

Part III: Cost Function

The cost function is a trade-off between the design variables. It evaluates the cost

and constraints at every iteration. If accurately chosen, a cost function has a great influence on the precision of the final results.

In this case, it is important to preserve the centroid at the origin, but the oriented beam properties are also valuable. An appropriate beam is characterized by a narrow Beam Width First Null (BWFN) pointing sharply to the target, and surrounded by a few sidelobes dependent on the amount of actuations frequencies and their numbers. These sidelobes' amplitudes should be minimal compared to the main lobe's amplitude and nulls must be reduced.

A convenient cost function to be used is proposed by Goswami and Mandal (2013). Each term represents one of the stated parameters multiplied by a weighting coefficient to control its importance. The minimizing equation is slightly modified to fit the requirements of this problem:

$$\begin{aligned} CF = & C_1 \times \frac{|\prod_{i=1}^m AF(null_i)|}{AF_{max}} + C_2 \times \sum_{k=1}^K H(k) \times (Q_k - \delta) \\ & + C_3 \times |FNBW_{computed} - FNBW_{desired}| \end{aligned} \quad (6.20)$$

where

$$H(k) = \begin{cases} 1, & (Q_k - \delta) > 0 \\ 0, & (Q_k - \delta) < 0 \end{cases} \quad (6.21)$$

and

$AF(null_i)$: Array factor at the null of index i in Decibels (dB)

Q_k : Sidelobe level in (dB)

δ : Desired sidelobe level in (dB)

$FNBW_{computed}$: Actual First Null Beam Width in radians (rad)

$FNBW_{desired}$: Desired First Null Beam Width in (rad)

C_1, C_2 and C_3 : Weighting coefficients

For a normalized Array Factor (AF_{norm}), AF_{max} is always equal to unity. Thus, Equation (6.15) reduces to:

$$CF = C_1 \times \left| \prod_{i=1}^m AF(null_i) \right| + C_2 \times \sum_{k=1}^K H(k) \times (Q_k - \delta) + C_3 \times |FNBW_{computed} - FNBW_{desired}| \quad (6.22)$$

Another form of cost function was manipulated by Bhattacharya et Al.(2012) for the purpose of optimizing an asymmetric circular antenna array². In their study, every antenna was given polar spherical coordinates (r, θ, φ) which are optimized through the analysis. The coordinates r, θ and φ stand respectively for the position of the wave emitter measured from the origin O, the out-of-plane elevation angle and the in-plane azimuth angle as depicted in Figure 6.5.

The employed cost function enables the determination of the weighting factor attributed to every emitting source. However, for this current research, it's assumed that all excitations occur at equal unit weights. The authors also suggest a minimizing cost function of a three dimensional (3D) space, but here the investigation is restricted only to planar arrangement of the actuated elements.

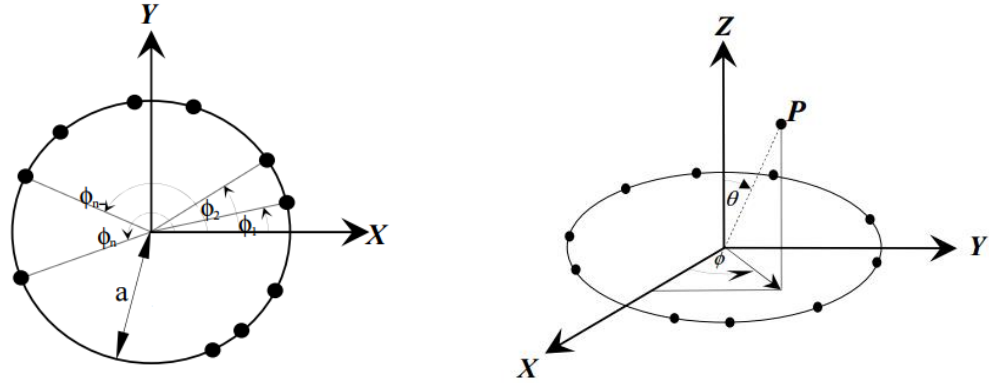


Figure 6.5. A three dimensional array of the wave radiators. Left - In plane arrangement; Right - An isometric view (Bhattacharya *et al.*,2012)

The modified cost function, CF, of antenna array in 2D space and equal weighting factor, assumed to be unity, is defined by:

$$CF = \frac{SLL_{initial}}{SLL_{current}} + \sum_{i=1}^M |AF(\theta_i)|^2 + |BWFN_{initial} - BWFN_{current}| \quad (6.23)$$

where

$$SLL_{initial} = 20 \log_{10} \left\{ \frac{0.5 |AF(\theta_{msl1_{initial}}) + AF(\theta_{msl2_{initial}})|}{|AF(\varphi_0)|} \right\} \quad (6.24)$$

and

$$SLL_{current} = 20 \log_{10} \left\{ \frac{0.5 |AF(\theta_{msl1_{current}}) + AF(\theta_{msl2_{current}})|}{|AF(\varphi_0)|} \right\} \quad (6.25)$$

The cost function (6.23) relates every iteration to the initial findings in a repetitive process, and the terms of Equations (6.23), (6.24) and (6.25) are determined as the following:

$SLL_{initial}$: Initial sidelobe level

$SLL_{current}$: Current sidelobe level

$AF(\theta_i)$: Array factor at the null of index i

$AF(\varphi_0)$: Array factor at the null of index i

$BWFN_{initial}$: Initial Beam Width First Null

$BWFN_{current}$: Current Beam Width First Null

$AF(\theta_{msl\ 1\ initial})$: Initial array factor of the upper band highest sidelobe

$AF(\theta_{msl\ 2\ initial})$: Initial array factor of the lower band highest sidelobe

$AF(\theta_{msl\ 1\ current})$: Current array factor of the upper band highest sidelobe

$AF(\theta_{msl\ 2\ current})$: Current array factor of the lower band highest sidelobe

Part IV: Extraction of best fitting chromosome, cross-over and mutation

After the evaluation of the pool of chromosomes consisting of the positional coordinates, crossover and mutation are performed. The extraction of the finest population can be done in several methods: the roulette wheel, the rank based and the tournament selections.

For the roulette method, the order of the chromosomes inside the matrix is permuted based on a procedure starting by computing an objective function, assessing its related fitness, estimating the probability and obtaining the cumulative probability of each chromosome. The last chromosome should have the cumulative probability equal to unity. Furthermore, random numbers between 0 and 1 are generated. The rule of selection of the chromosomes for the next generation is given by: Consider the i^{th} chromosome (vector) in matrix P (Equation 6.19), R(i) its random number and C(i) its cumulative probability. If R(i) is greater than C(i) and less than C(i+1), then, pick the chromosome of index i+1 for the next generation. Otherwise, the i^{th} chromosome is taken. Therefore, the

new elements of the upcoming generation are reorganized in a new matrix.

Another useful method is described by Raja and Bhaskaran (2008) to improve the performance of Genetic Algorithm by reducing the population size. Known as tournament selection, this method tends to divide the population into small groups. Then, tournaments are achieved between the individuals of the same group to recognize the decent individuals from the hunt space. The winning members, having the minimum cost function, constitute the new population.

Ranked selection is another method to extract eligible candidates from the population. From its name, it can be inferred that the elements having the highest probability are allowed to proceed. In contrast with other selection techniques, ranked selection allows preservation of a constant population through all of the iterations. This method will be chosen as a selection criteria because it has the highest profit and the best convergence amongst the others.

Cross-over is operated to bring the population to convergence towards a local optimum. It occurs when a pair of chromosomes hybridizes. Crossbreeding can occur at single, double or multiple points. As a result, the offspring chromosomes contain a mixture of genes of the two parents. In matrix P, the vectors to be crossed-over are selected upon a predetermined cross-over parameter, ρ . As stated before, for each single chromosome, there corresponds a generated random number $R(i)$. If $R(i)$ is less than ρ , then the vector of order i is a parent of the offspring generation. In this case, uniform (multiple points) cross-over is performed by randomly choosing the breeding locations.

Mutation is a divergence process; it has the tendency to introduce some new members to the population in order to seek for a probable optimum solution in another

space. Mutation is done by substituting a gene (y -coordinate) at a random position by a new value. Four factors characterize a mutation; these are the mutation rate, number of mutations, mutation locations and mutating values. The mutation rate is a numerically adjustable value that must be kept as low as possible. The number of mutations is determined by multiplying the number of genes by the total number of chromosomes in a population and by the mutation rate. Then, the decimal number is rounded to the nearest integer. The location of the mutated element is randomly selected and the mutation value is given by replacing $r_{i,j}$ in Equation (6.7) with a new decimal between 0 and 1.

After passing through all of the mentioned steps, the cycle is repeated until the given number of generations is reached. Finally, among all of the best chromosomes extracted from each cycle, the most fitting solution vector is chosen for the final result.

The following instructions are followed for optimization:

- Number of Individuals per generation: 100 (for aluminum) / 50 (for composites)
- Number of generations: 50
- Selection Mechanism: Ranked selection
- Crossover Type: Uniform crossover
- Crossover Rate: 0.90
- Mutation Rate: 0.15

7. Data Analysis and Findings

In this chapter, the plotted results of the simulated algorithm using MATLAB are presented. Two fundamental aims are satisfied from the data collection and the subsequent analysis. The first goal is to design and model a random pattern of actuation arrays for structural health monitoring of a thin plate. The number of actuation points and the material type are the floating parameters, whereas the excitation time delay has to remain uniform along the scanning process.

Second, the challenge is to demonstrate the consistency of the perception and validate its effectiveness for future utilization. For this reason, the beamforming is plotted in Cartesian and polar coordinate systems and the convergence of the cost function is illustrated. The space arrangement of the emission points is also schemed for anisotropic and isotropic materials as well as for the increased actuation points.

The findings are finally compared to previously developed studies on uniformly distributed, linear and disk patterns of emission sources fired at varying time delay. This alteration of the moment of excitation accounts for the distance of each actuation point from the target. Once the tasks are successfully fulfilled, the results have shown efficiency for upcoming use.

7.1. Random Array Results for Aluminum

For aluminum, the simulations are performed for 40, 51 and 66 random actuation points to scan a target point at 90° angle from the horizontal.

- 40 Actuations:

The polar and linear beamforming, the cost function and the space arrangement of the 40

actuators pattern are shown in Figures (7.1) to (7.4).

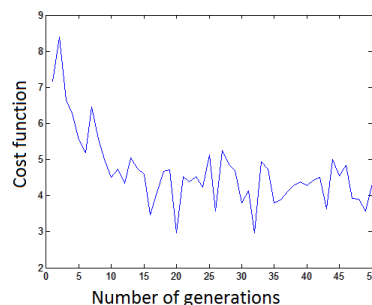
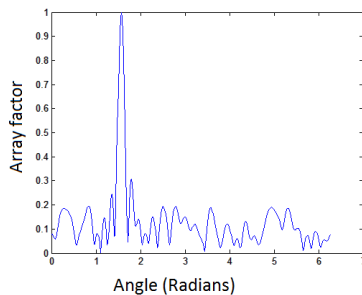
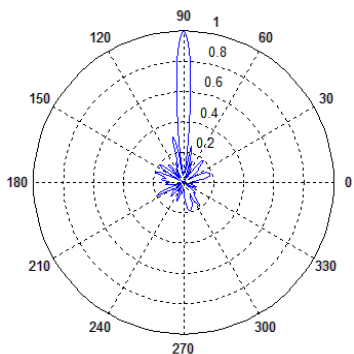


Figure 7.1. Polar beamforming resulting from 40 actuators and pointing towards a 90° target on an aluminum plate

Figure 7.2. A Cartesian plot of the array factor illustrating the main beam at 90° and its adjacent side lobes of 40 actuators for an isotropic medium

Figure 7.3. The convergence process of the cost function to the optimum solution by means of a Genetic Algorithm processing of 40 locations for an isotropic medium

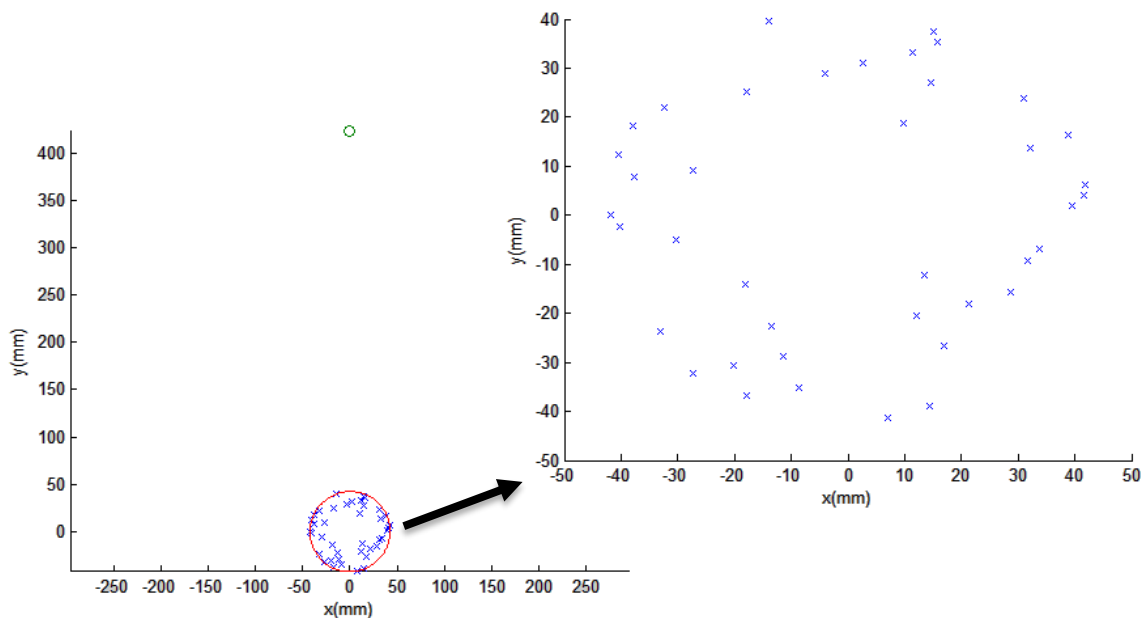


Figure 7.4. A space arrangement of the 40 actuators enclosed within a circular aperture and facing a target point in the near field on an aluminum plate

- 51 Actuators:

The polar and linear beamforming, the cost function and the space arrangement of the

51 actuations pattern are shown in Figures (7.5) to (7.8).

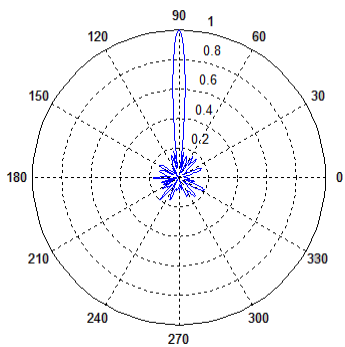


Figure 7.5. Polar beamforming resulting from 51 random actuations and pointing towards a 90° target on an aluminum plate

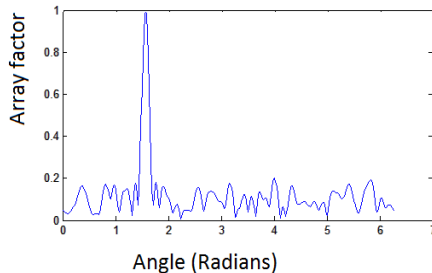


Figure 7.6. A Cartesian plot of the array factor illustrating the main beam at 90° and its adjacent side lobes of 51 actuations for an isotropic medium

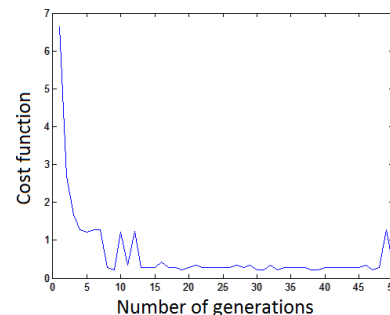


Figure 7.7. The convergence process of the cost function to the optimum solution by means of a Genetic Algorithm processing of 51 locations for an isotropic medium

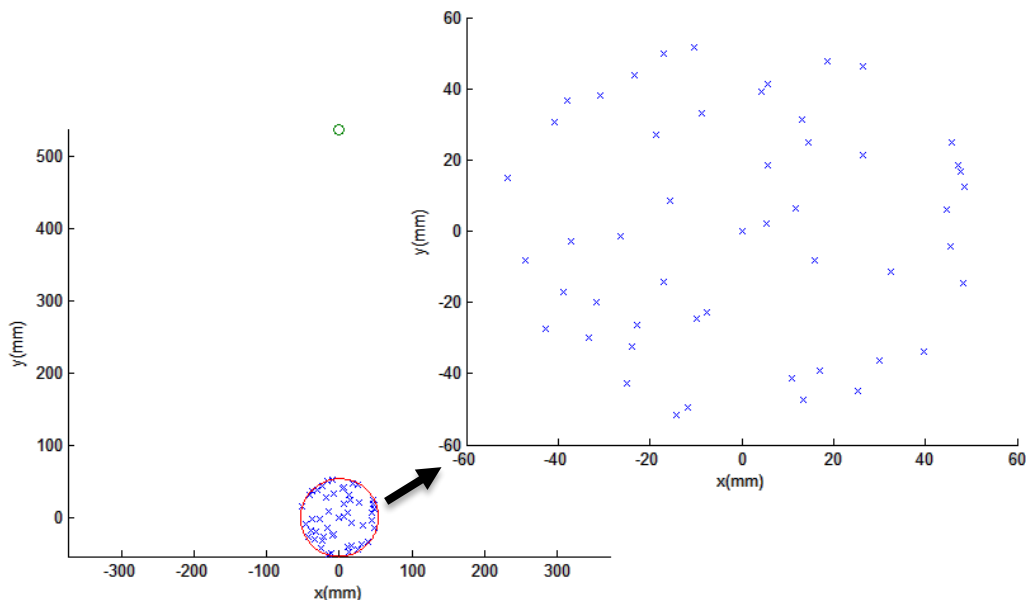


Figure 7.8. A space arrangement of the 51 actuation points enclosed within a circular aperture and facing a target point in the near field on an aluminum plate

- 66 Actuations:

The polar and linear beamforming, the cost function and the space arrangement of the 66 actuations pattern are shown in Figures (7.9) to (7.12).

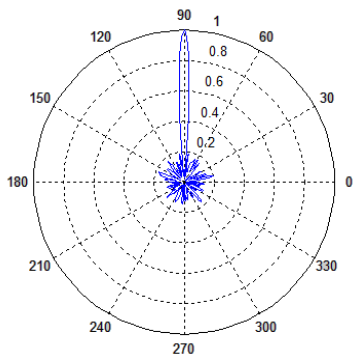


Figure 7.9. Polar beamforming resulting from 66 random actuations and pointing towards a 90° target on an aluminum plate

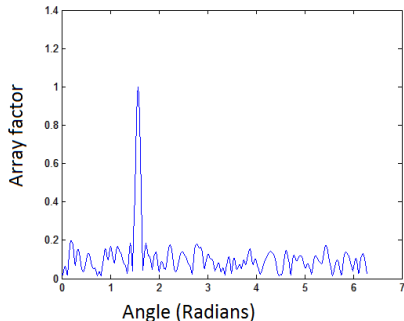


Figure 7.10. A Cartesian plot of the array factor illustrating the main beam at 90° and its adjacent side lobes of 66 actuations for an isotropic medium

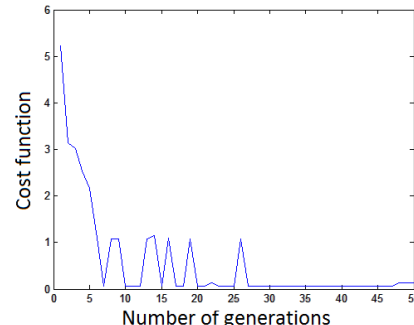


Figure 7.11. The convergence process of the cost function to the optimum solution by means of a Genetic Algorithm processing of 66 locations for an isotropic medium

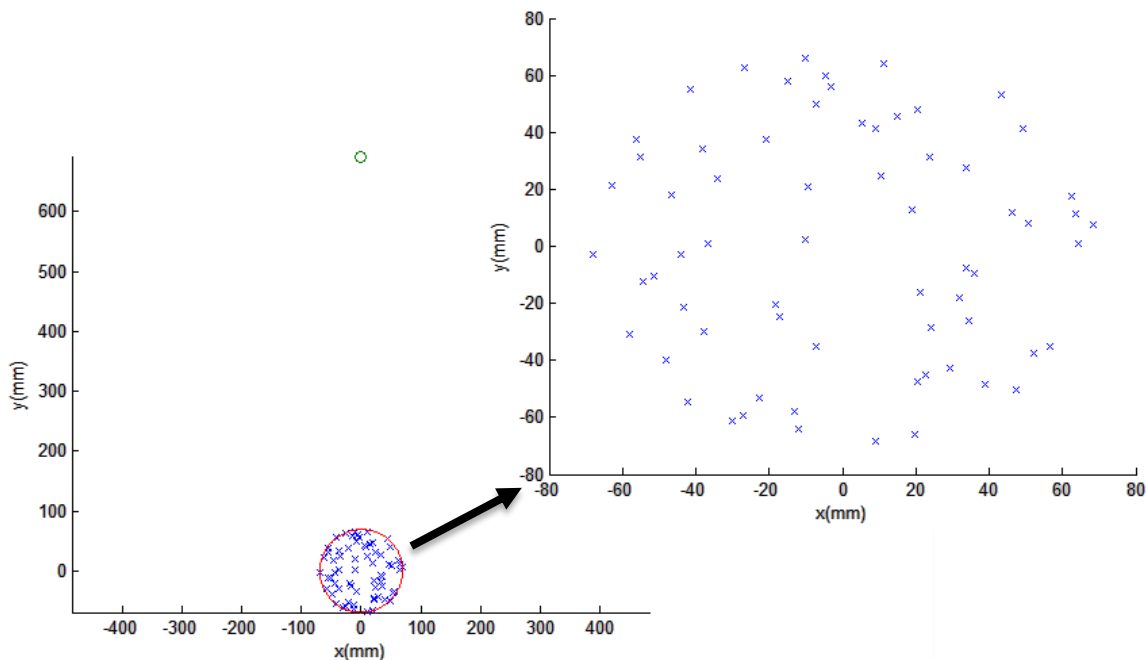


Figure 7.12. A space arrangement of the 66 actuation points enclosed within a circular aperture and facing a target point in the near field on an aluminum plate

7.2. Random Array Results for a 0° Unidirectional Laminate

For composite, the simulations are performed for 20, 51 and 66 actuation points to scan a target point at 90° angle from the horizontal.

- 20 Actuators:

The polar and linear beamforming, the cost function and the space arrangement of the 20 actuators pattern for a 0° unidirectional laminate are shown in Figures (7.13) to (7.16).

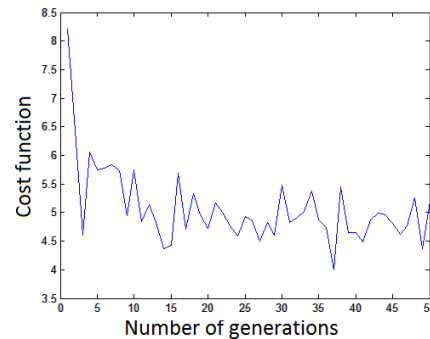
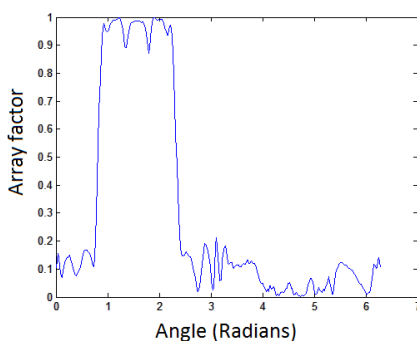
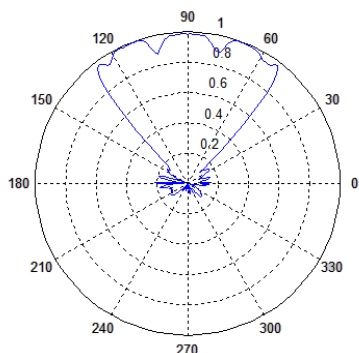


Figure 7.13. Polar beamforming resulting from 20 random actuators and pointing towards a 90° target on a 0° unidirectional fiber plate

Figure 7.14. A Cartesian plot of the array factor illustrating the main beam at 90° and its adjacent side lobes of 20 actuators in a 0° fiber medium

Figure 7.15. The convergence process of the cost function to the optimum solution by means of a Genetic Algorithm processing of 20 locations in a 0° fiber medium

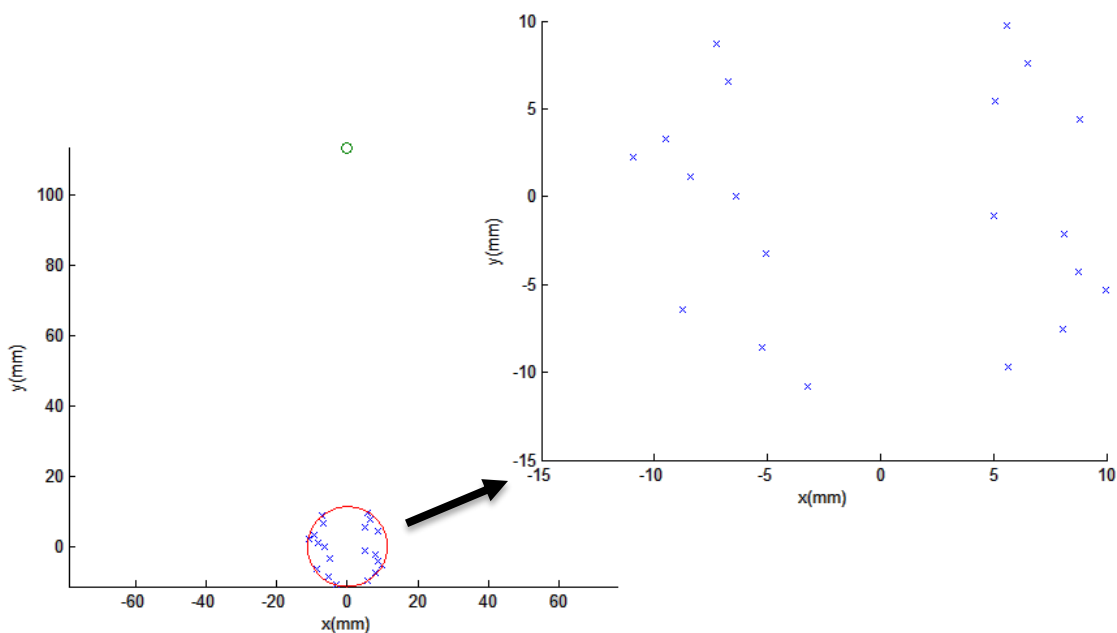


Figure 7.16. A space arrangement of the 20 actuation points enclosed within a circular aperture and facing a target point in the near field on a 0° Unidirectional Laminate

- 51 Actuators:

The polar and linear beamforming, the cost function and the space arrangement of the 51 actuations pattern for a 0° unidirectional laminate are shown in Figures (7.17) to (7.20).

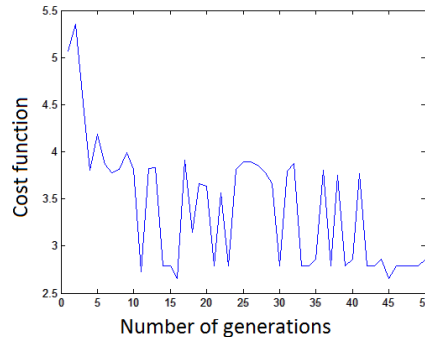
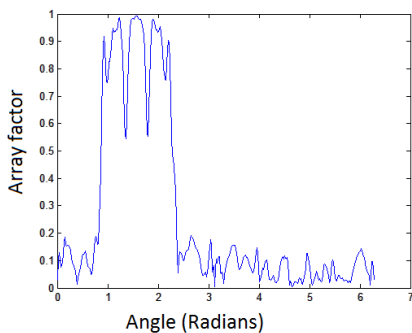
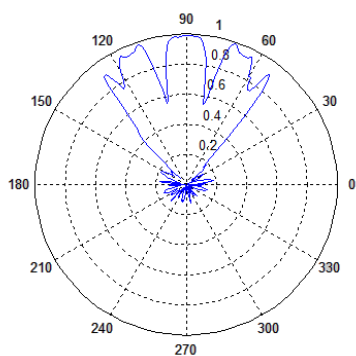


Figure 7.17. Polar beamforming resulting from 51 random actuators and pointing towards a 90° target on a 0° unidirectional fiber plate

Figure 7.18. A Cartesian plot of the array factor illustrating the main beam at 90° and its adjacent side lobes of 51 actuators in a 0° fiber medium

Figure 7.19. The convergence process of the cost function to the optimum solution by means of a Genetic Algorithm processing of 51 chromosomes in a 0° fiber medium

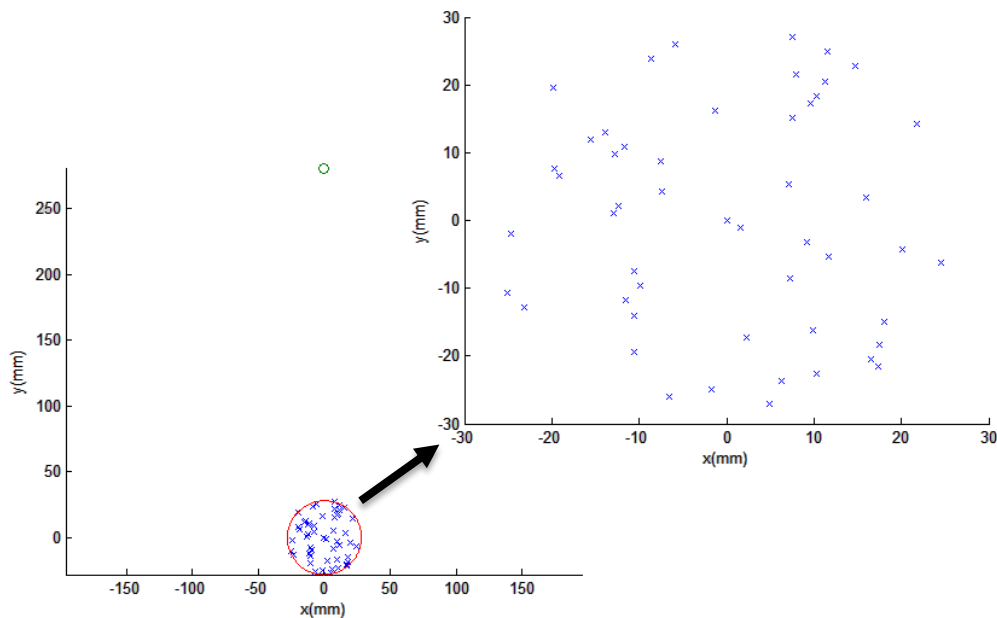


Figure 7.20. A space arrangement of the 51 actuation points enclosed within a circular aperture and facing a target point in the near field on a 0° Unidirectional Laminate.

- 66 Actuators:

The polar and linear beamforming, the cost function and the space arrangement of the 66 actuators pattern for a 0° unidirectional laminate are shown in Figures (7.21) to (7.24).

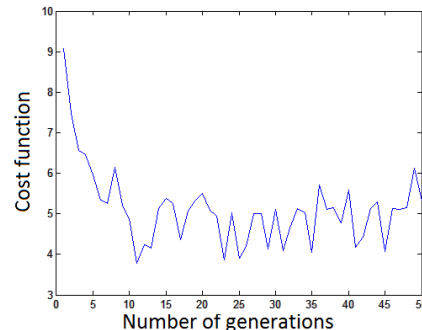
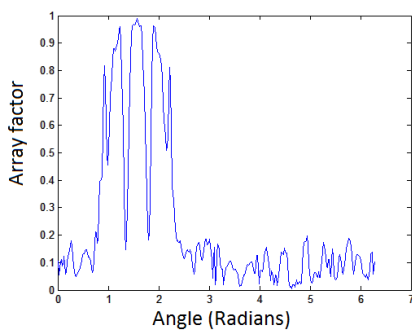
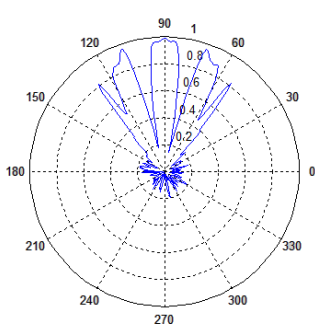


Figure 7.21. Polar beamforming resulting from 66 random actuations and pointing towards a 90° target on a 0° unidirectional fiber plate

Figure 7.22. A Cartesian plot of the array factor illustrating the main beam at 90° and its adjacent side lobes of 66 actuations in a 0° fiber medium

Figure 7.23. The convergence process of the cost function to the optimum solution by means of a Genetic Algorithm processing of 66 locations in a 0° fiber medium

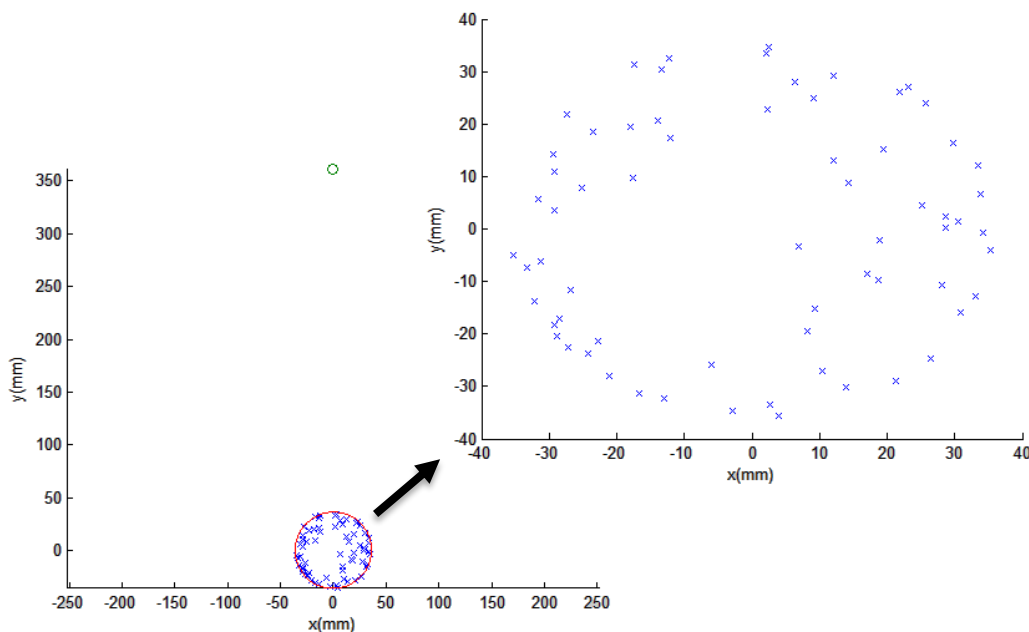


Figure 7.24. A space arrangement of the 66 actuation points enclosed within a circular aperture and facing a target point in the near field on a 0° Unidirectional Laminate

7.3. Random Array Results for a 90° Unidirectional Laminate

In the case, the fibers are rotated to the direction of the target point.

- 18 Actuators:

The polar and linear beamforming, the cost function and the space arrangement of the 51 actuations pattern for a 90° unidirectional laminate are shown in Figures (7.25) to (7.28).

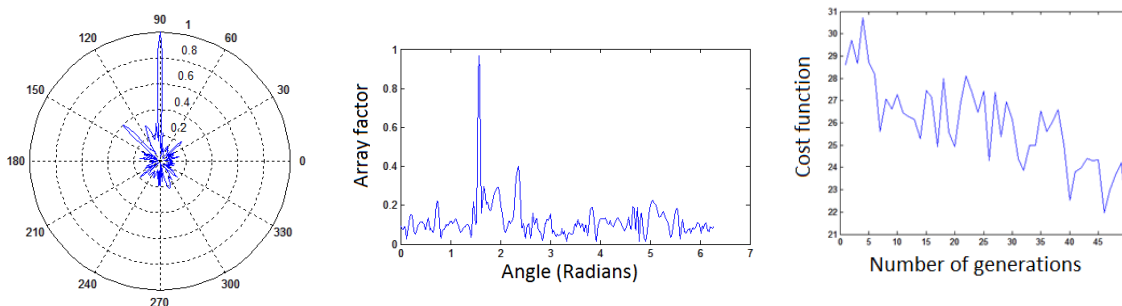


Figure 7.25. Polar beamforming resulting from 18 random actuators and pointing towards a 90° target on a 90° unidirectional fiber plate

Figure 7.26. A Cartesian plot of the array factor illustrating the main beam at 90° and its adjacent side lobes of 18 actuators in a 90° fiber medium

Figure 7.27. The convergence process of the cost function to the optimum solution by means of a Genetic Algorithm processing of 18 locations in a 90° fiber medium

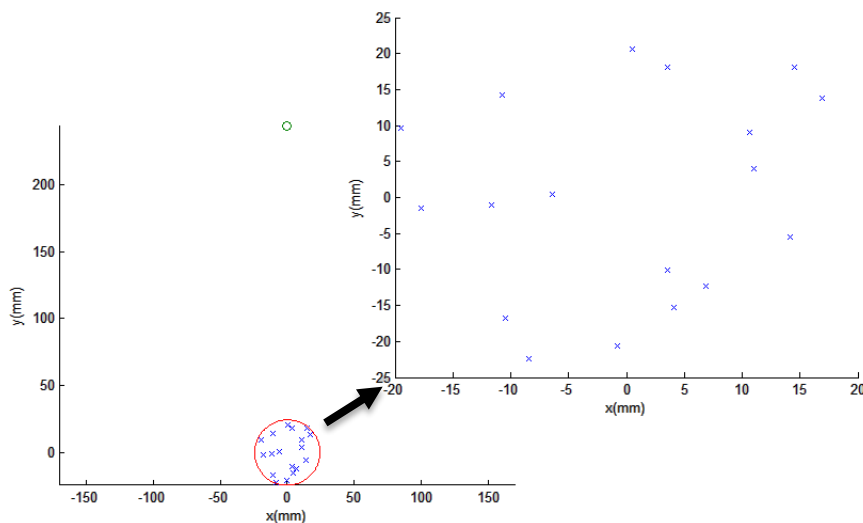


Figure 7.28. A space arrangement of the 18 actuation points enclosed within a circular aperture and facing a target point in the near field on a 90° Unidirectional Laminate

- 20 Actuators:

The polar and linear beamforming, the cost function and the space arrangement of the 51 actuations pattern for a 90° unidirectional laminate are shown in Figures (7.29) to (7.32).

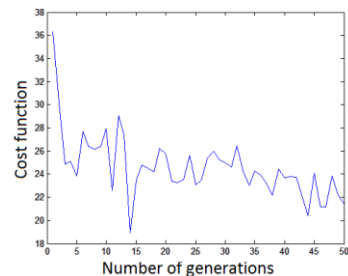
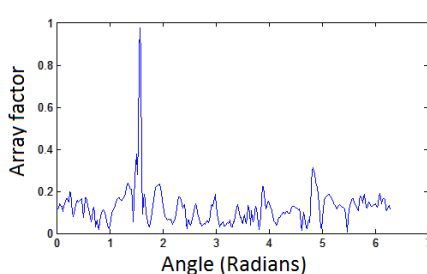
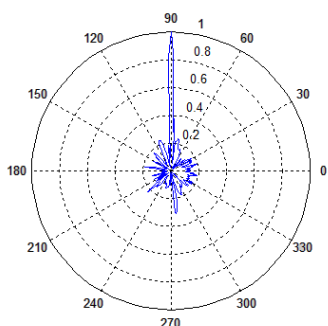


Figure 7.29. Polar beamforming resulting from 20 random actuators and pointing towards a 90° target on a 90° unidirectional fiber plate

Figure 7.30. A Cartesian plot of the array factor illustrating the main beam at 90° and its adjacent side lobes of 20 actuators in a 90° fiber medium

Figure 7.31. The convergence process of the cost function to the optimum solution by means of a Genetic Algorithm processing of 20 locations in a 90° fiber medium

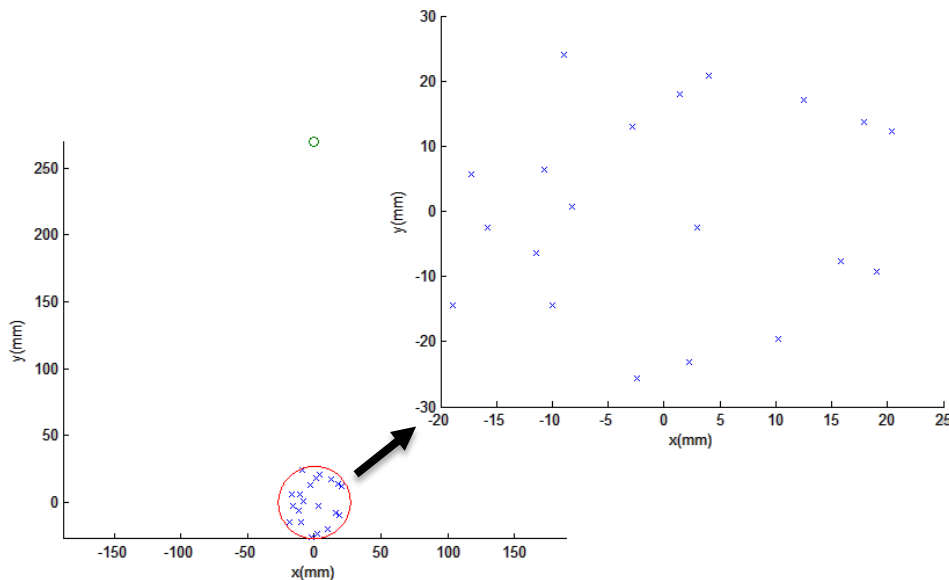


Figure 7.32. A space arrangement of the 20 actuation points enclosed within a circular aperture and facing a target point in the near field on a 90° Unidirectional Laminate

7.4. Results of a Uniformly Distributed Linear Array for an Orthotropic Laminate

Here, the beamforming of a fixed number of 20 equally spaced actuation points, fired at varying time, are plotted in both cases of a 0° and 90° unidirectional fiber plates in Figures (7.33) and (7.34) respectively.

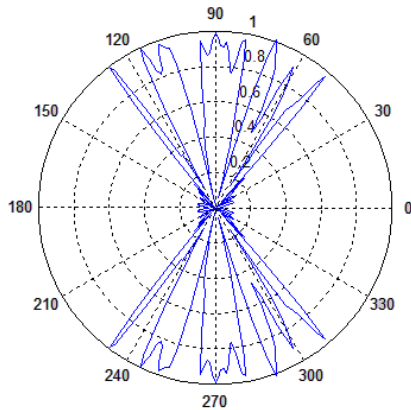


Figure 7.33. Polar beamforming resulting from 20 linear actuations and pointing towards a 90° target on a 0° unidirectional fiber plate

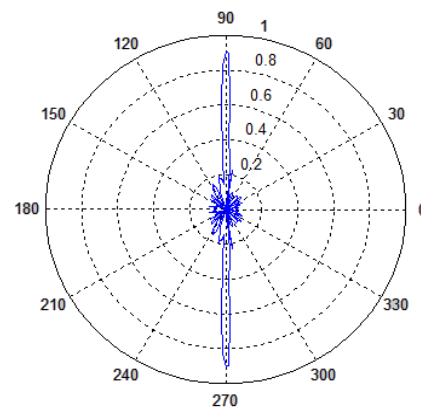


Figure 7.34. Polar beamforming resulting from 20 linear actuations and pointing towards a 90° target on a 90° unidirectional fiber plate

7.5. Results of Uniform Array Geometries for an Isotropic Material

The beamforming equations of linear and disk planar arrays, derived by Lingyu (2006), are used to model the wave maximum displacement in Figures (7.35), (7.36) and (7.37). Note that these patterns have fluctuating excitation delay. Later, these findings are compared to the investigated random patterns.

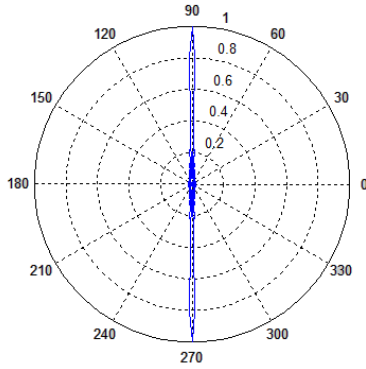


Figure 7.35. Polar beamforming resulting from 40 linear actuators and pointing towards a 90° target on an aluminum plate

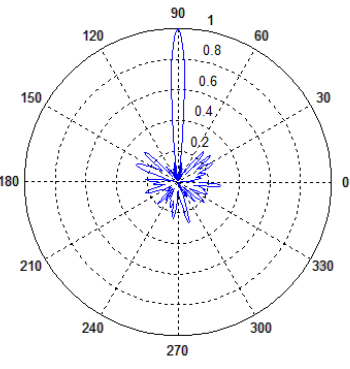


Figure 7.36. Polar beamforming resulting from a disk pattern of 40 actuators and pointing towards a 90° target on an aluminum plate

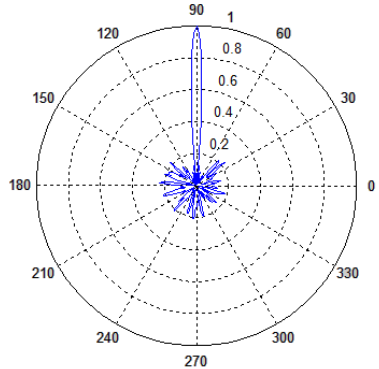


Figure 7.37. Polar beamforming resulting from a disk pattern of 66 actuators and pointing towards a 90° target on an aluminum plate

7.6. Discussion and Interpretation

The beamforming plots in the previous section aim to verify the directionality and out-of-plane displacement amplitude of the wave front. However, the main characteristics of these schemes are summarized in Tables (7.1) to (7.5) below.

Table 7.1. Beamwidth first null and sidelobes' levels at different random actuation points for an isotropic medium

Number of actuators	Beam Width First Null (BWFN)	Side Lobe Levels (SLL)
40	16.01°	0.3075
51	16.01°	0.1998
66	12.00°	0.1990

Table 7.2. Beamwidth first null and sidelobes' levels at different uniformly spaced actuation points for an isotropic medium

Array type	Number of actuators	Beam Width First Null (BWFN)	Side Lobe Levels (SLL)
Linear	40	6°	0.2176
Disk	40	16°	0.2989
Disk	66	12°	0.2297

Table 7.3. Beamwidth first null and sidelobes' levels at different random actuation points for a 0° unidirectional fiber plate

Number of actuators	Beam Width First Null (BWFN)	Side Lobe Levels (SLL)
20	94°	0.2120
51	86°	0.1903
66	86°	0.1904

Table 7.4. Beamwidth first null and sidelobe levels at different random actuation points for a 90° unidirectional fiber plate

Number of actuators	Beam Width First Null (BWFN)	Side Lobe Levels (SLL)
18	6°	0.3784
20	6°	0.3999

Table 7.5. Beamwidth first null and sidelobes' levels at different random actuation points for a linear 20 actuators array over a composite plate

Composite orientation	Beam Width First Null (BWFN)	Side Lobe Levels (SLL)
0°	84°	0.3592
90°	12°	0.2281

By comparing the beamwidth and the sidelobes' levels of patterns within the same material category, here are some basic deductions:

- By increasing the number of actuation points, the BWFN and the SLLs decrease; the beam is narrowed and the nulls are pushed down to the pattern's centroid.
- Independent of the material type, a linear uniformly distributed array generates a grating lobe symmetrical to the main lobe in the opposite direction for a 90° steering.

- Due to the anisotropic nature of composites, the fibers help improving the directionality of the beam and a lower number of actuation points is required for a beam steering along the fibers.
- In the direction orthogonal to the fibers, the friction with the orthotropic material is at its maximum so the formed beam tends to diverge from the target and the beamwidth is about 90° . Increasing the actuation helps to slightly decreasing the beamwidth up to a certain limit ($\approx 10\%$).
- A random array, excited at the same time delay, proves to have the same wave features as a regularly distributed, non-uniformly excited disk array. For the latter, the excitation moment is determined by the distance of the excitation point to the target.
- Some tolerant errors in the composite plots (negligible dissymmetry in beamforming) happened due to the choice of the beamforming expression used in the algorithm. The array factor for isotropic media is transformed to account for anisotropy. However, the expression of displacement should be derived from the initial partial differential wave equation of a unidirectional laminate stated in chapter 2.

8. Conclusion and Future Work

In the current thesis, an optimization algorithm is developed to position in space the location of actuation points fired from a source to excite a structural surface. The health of the monitored part is evaluated based on the response to the propagating wave packet. The wave front of the resultant beam is guided to the target by calibrating the time delay between the firing of excitations. Assuming a constant time suspension, the geometry of the actuations' pattern is optimized to shape a steered beam able to reach the location being inspected. A mathematical model is developed to describe the stated hypothesis. Then, finite element simulations are conducted to obtain the wave physical characteristics. Finally, all the findings are implemented in a genetic algorithm to predict the profile of the actuation points. After succeeding to accomplish the task, the results are compared to conventional patterns manipulated in previous studies. The outcomes are promising and this research can be developed further in the future. The coded Genetic Algorithm (GA) has a general use; it is not only restricted to unidirectional laminates. However, here are some reforms to be achieved to complete the research:

- Generation of velocity dispersion curves suitable for the anisotropic plate by selecting the most accurate method among those stated in chapter 2.
- Derivation the out-of-plane displacement and beamforming expression from the unidirectional laminate wave differential equation.
- Modification of the GA code to be able to steer the target in all direction instead of only the 90° position.
- Validation of the excitation pattern virtually by means of ABAQUS software or experimentally.

REFERENCES

Ahmad Z. A. B., Vivar-Perez, J. M. & Gabbert, U. (2013). Semi-analytical finite element method for modeling of lamb wave propagation. Springer.

Baskar Rao, M., Bhat, M.R., Murthy, C.R.L., Venu Madhav, K. & Asokan, S. Structural Health Monitoring (SHM) Using Strain Gauges, PVDF Film and Fiber Bragg Grating (FBG) Sensors: A Comparative Study. (2006). In *Proceedings of National Seminar on Non-Destructive Evaluation*.

Bevelacqua P.J. (2008). *Antenna arrays: performance limits and geometry optimization*. Arizona state university.

Bhattacharya, M., Das, S., Mandal, D. & Bhattacharjee, A.K. (2012). Asymmetric circular array antenna synthesis based on angular positions. *International Journal of Information and Electronics Engineering, Vol. 2, No. 3*.

Bhattacharya, R., Bhattacharyya, T.K. & Garg, R. (2012). Position mutated hierarchical particle swarm optimization and its application in synthesis of unequally spaced antenna arrays. *IEEE TRANSACTIONS ON ANTENNAS AND PROPAGATION, VOL. 60, NO. 7*.

Boeringer, D.W. & Werner, D.H. (2004). Particle Swarm Optimization Versus Genetic Algorithms for Phased Array Synthesis. *IEEE TRANSACTIONS ON ANTENNAS AND PROPAGATION, VOL. 52, NO. 3*.

Calomfirescu, M. (2008). Lamb Waves for Structural Health Monitoring in Viscoelastic Composite Materials. Universität Bremen.

Cardona, J., Tabuenca, P. & Samartin, A. (2008). A numerical solution of the dispersion equation of the guided wave propagation in N-layered media.

Carr, J. (2014). An introduction to genetic algorithm.

Chang, P.C., Flatau, A. & Liu S. C. (2003). Health Monitoring of Civil Infrastructure. SAGE Publications.

Chen, T.B., Chen, Y.B., Jiao, Y.C., & Zhang F.S. (2005). Synthesis of antenna array using particle swarm optimization. In *APMC Proceedings*.

Choi, H., Choi, S. and Cha, H. (2008). Structural Health Monitoring System based on Strain Gauge Enabled Wireless Sensor Nodes. In *IEEE*.

Clerc, M. (2012). Standard Particle Swarm Optimization.

Colangelo, V.J., Heiser, F. A. (1987). Analysis of Metallurgical Failures. Wiley-Interscience.

Datta, T. & Misra, I.S. *A comparative study of optimization techniques in adaptive antenna array processing: the bacteria-foraging algorithm and particle-swarm optimization*. Jadavpur University.

David J. & Cheeke N. (2012). Fundamentals and Applications of Ultrasonic Waves. Second Edition. Taylor & Francis.

Deng, Y. & Liu, X. (2011). Electromagnetic Imaging in Structural Health Monitoring (SHM) and Nondestructive Evaluation (NDE). Anschutz Medical Campus, University of Colorado Denver.

Farrar, C. R. & Worden, K. (2007). An Introduction to Structural Health Monitoring. The Royal Society Press.

Flores-Mendoza, J.I. & Mezura-Montes, E. Looking inside particle swarm optimization in constrained search spaces.

Ghosh, P., Banerjee, J., Das, S. & Chaudhury, S.S. (2012). Design of non-uniform circular antenna arrays: an evolutionary algorithm based approach. *Progress in Electromagnetics Research B*, Vol. 43, 333-354.

Giurgiutiu, V. (2014). *Structural Health Monitoring with Piezoelectric Wafer Active Sensors*. Academic Pr

Goswami, B. & Mandal, D. (2013). A genetic algorithm for the level control of nulls and sidelobes in linear antenna arrays. *Journal of King Saud University*, pp.117–126.

Goswami, B. & Mandal, D. (2012). A genetic algorithm for the level control of nulls and sidelobes in linear antenna arrays. *Journal of King Saud University – Computer and Information Sciences* (2013) 25, 117–126.

Guo, H., Xiao G., Mrad, N., & Yao J., (2011) Fiber Optic Sensors for Structural Health Monitoring of Air Platforms. *Sensors*, 11, 3687-3705

Hassan, R., Cohanin, B. & De Weck O. A comparison of particle swarm optimization and the genetic algorithm. In *AIAA*.

Helwig, S., Neumann, F. & Wanka, R. Particle swarm optimization with velocity adaptation.

Herrera, F., Lozano, M. & Verdegay, J.L.(1998). Tackling real-coded genetic algorithms: operators and tools for behavioural analysis. *Artificial Intelligence Review* 12: 265–319.

Jaeger, J.C., Cook, N.G.W., Zimmerman, R. (2009). *Fundamentals of Rock Mechanics*. John Wiley & Sons.

Jayaprakasam, S., Rahim, S. K. A. & Leow, C. (2013). A pareto elite selection genetic algorithm for random antenna array beamforming with low sidelobe level.

Progress in Electromagnetics Research B, Vol. 51, 407-425.

Kamal, A. & Giurgiutiu. (2014). Stiffness Transfer Matrix Method (STMM) for stable dispersion curves solution in anisotropic composites. In *SPIE*.

Kaur, I. & Kumar, S. (2011). linear antenna array optimization techniques.

International Journal of Engineering Trends and Technology.

Kennedy, J. & Eberhart, R. (1995). Particle swarm optimization. In *IEEE*.

Lahiri, S.K., Gangopadhyay, R., Mathur, B.K., Dutta, A.K., Ray, S.K. and Das, S. (2000). International Conference on Fiber Optics and Photonics. *ISBN 81-7764-103-4.*

Li, Y. & Thompson, R.B. (1990). Influence of anisotropy on the dispersion characteristics of guided ultrasonic plate modes. Iowa State University.

Mandal, D., Bhattacharjee, A.K. & Ghoshal, S.P. (2009). Comparative optimal designs of non-uniformly excited concentric circular antenna array using evolutionary optimization techniques. *Second International Conference on Emerging Trends in Engineering and Technology.*

Merad, L., Bendimerad, F.T. & Meriah, S.M. (2006). Controlled random search optimization for linear antenna arrays. *RADIOENGINEERING, VOL. 15, NO. 3.*

Mezura-Montes E. & Flores-Mendoza, J.I. Improved particle swarm optimization in constrained numerical search spaces. Laboratorio Nacional de Informatica Avanzada.

Nagayama, T. & Spencer, B.F. (2007). Structural Health Monitoring Using Smart Sensors. NSEL Report Series, Report No. NSEL-001

Osterc, P. & Kim D. (2013). Phased array beamsteering in composite laminates for guided wave structural health monitoring. In proceedings of AIAA.

Osterc, P. (2015). Phased array beamsteering in composite laminates for guided wave structural health monitoring (unpublished master's thesis). Embry Riddle Aeronautical University.

Pant, S. (2014). Lamb Wave Propagation and Material Characterization of Metallic and Composite Aerospace Structures for Improved Structural Health Monitoring (SHM). Carleton University Ottawa, Ontario.

Raja, V. & Bhaskaran, M. (2013). Improving the performance of genetic algorithm by reducing the population size. *International Journal of Emerging Technology and Advanced Engineering, Volume 3, Issue 8.*

Rattan, M. (2008). Antenna array optimization using evolutionary approaches. *Apeiron, Vol. 15, No. 1.*

Richards, W. L., Madaras, E., Prosser W. H., & Studor G. (2013, 10 September). NASA Applications of Structural Health Monitoring Technology. In 9th International Workshop on Structural Health Monitoring.

Ridwan, M., Abdo M. & Jorswieck, E. (2012). Design of non-uniform antenna arrays using genetic algorithm. *Journal of Wireless Networking and Communications, 2(2): 7-10.*

Rokhlin S.I., Chimenti, D. E. & Nagy, P. B. (2011). Physical Ultrasonics of composites. Oxford University Press.

Rose, J. L. (1999). Health monitoring of composite structures using guided waves. Penn State University.

Rose, J. L. (1999). *Ultrasonic waves in solid media*. Cambridge University Press.

Rytter, A. (1993). *Vibrational Based Inspection of Civil Engineering Structures*. Aalborg: Dept. of Building Technology and Structural Engineering, Aalborg University. (Fracture and Dynamics; No. 44, Vol. R9314).

Shreni, V. & Raikwar, P. (2012). Optimization of Reduction in Side Lobe Level Using Genetic Algorithm. *International Journal of Emerging Technology and Advanced Engineering, Volume 2, Issue 12*.

Vaara P. & Leinonen J. (2012). Technology Survey on NDT of Carbon-fiber Composites. Kemi-Tornio University of Applied Sciences.

Wan, X., Zhang Q., Xu, G., & Tse, P.W. Numerical Simulation of Nonlinear Lamb Waves Used in a Thin Plate for Detecting Buried Micro-Cracks. *Sensors, 14*, 8528-8546.

Wang, L. & Yuan, F.G. (2007). Group velocity and characteristic wave curves of Lamb waves in composites: Modeling and experiments. *Composites Science and Technology*, 1370–1384.

Yu, L. (2006). In-Situ Structural Health Monitoring with Piezoelectric Wafer Active Sensor Guided-Wave Phased Arrays. *PhD. Dissertation, Department of Mechanical Engineering, College of Engineering and Information Technology, University of South Carolina*.

Yu, L. and Giurgiutiu, V. (2005). Improvement of Damage Detection with the Embedded Ultrasonics Structural Radar for Structural Health Monitoring. In *5th International Workshop on Structural Health Monitoring*.

Yu, L. and Giurgiutiu, V. (2005). Using Phased Array Technology and Embedded Ultrasonic Structural Radar for Active Structural Health Monitoring and Nondestructive Evaluation. In *Proceedings of IMECE*.